

SPECTROSCOPIC AND ELECTROCHEMICAL STUDIES  
OF *SHEWANELLA ONEIDENSIS* CYTOCHROME C  
NITRITE REDUCTASE, AND IMPROVING C-HEME  
EXPRESSION SYSTEMS

by

Natalia Stein

A Dissertation Submitted in

Partial Fulfillment of the

Requirements for the Degree of

Doctor of Philosophy

in Chemistry

at

The University of Wisconsin-Milwaukee

December 2014

UMI Number: 3685085

All rights reserved

INFORMATION TO ALL USERS

The quality of this reproduction is dependent upon the quality of the copy submitted.

In the unlikely event that the author did not send a complete manuscript and there are missing pages, these will be noted. Also, if material had to be removed, a note will indicate the deletion.



UMI 3685085

Published by ProQuest LLC (2015). Copyright in the Dissertation held by the Author.

Microform Edition © ProQuest LLC.

All rights reserved. This work is protected against unauthorized copying under Title 17, United States Code



ProQuest LLC.  
789 East Eisenhower Parkway  
P.O. Box 1346  
Ann Arbor, MI 48106 - 1346

# ABSTRACT

## SPECTROSCOPIC AND ELECTROCHEMICAL STUDIES OF *SHEWANELLA ONEIDENSIS* CYTOCHROME C NITRITE REDUCTASE, AND IMPROVING C-HEME EXPRESSION SYSTEMS

by

Natalia Stein

The University of Wisconsin-Milwaukee, 2014  
Under the Supervision of Professor Andy Pacheco

In this work the redox properties of cytochrome c nitrite reductase (CcNiR), a decaheme homodimer that was isolated from *S. oneidensis*, were determined in the presence and absence of the strong-field ligands cyanide and nitrite. Four hemes per CcNiR protomer are hexa-coordinate with tightly bound axial histidines, while the fifth (active site) has one tightly bound lysine and a distal site that can be open, or contain exogenous ligands such as the substrate nitrite. Controlled potential electrolysis in combination with UV/visible absorption (UV-vis) and electron paramagnetic resonance (EPR) spectroscopies allowed for assignment of all heme midpoint potentials under each set of conditions. The studies show that the active-site heme is the first to be reduced under all conditions. The midpoint redox potential of that heme shifts approximately 70mV to the positive upon binding a strong field ligand such as nitrite or cyanide. When controlled potential electrolysis was carried out in the presence of nitrite, a concerted two electron reduction was observed by UV-vis, and a  $\{\text{Fe}(\text{NO})\}^7$

reduced product was revealed in EPR. In addition, an asymmetry in ligand binding between active sites was revealed. This information is relevant for the interpretation of planned and ongoing mechanistic studies of CcNiR.

Over-expression, partial purification and characterization of another *S. oneidensis* multiheme enzyme, known as octaheme tetrathionate reductase (OTR), is also described herein. Though of unknown cellular function, OTR was previously reported to have tetrathionate reductase activity, in addition to nitrite and hydroxylamine reductase activities. The new results indicate that the expression of OTR has no effect on tetrathionate or nitrite reductase activities in the whole cell lysate, and only hydroxylamine reductase activity was substantially elevated in the overexpressing bacteria. OTR was stable in buffered solutions, but substantial activity loss during all attempts at column chromatography was a major obstacle to the complete purification. OTR also proved quite hydrophobic, so possible membrane association should be considered in future attempts to purify this protein.

Finally, this dissertation also reports attempts to improve *S. oneidensis*' ability to express foreign proteins. Though ideally suited to expressing c-hemes, it proved difficult to express carboxy his-tagged proteins in *S. oneidensis* because of persistent tag degradation. Attempts to knock out lon protease, a cytoplasmic carboxypeptidase, as well as the result of redirecting ccNiR from the SecA to the possibly more protected signal particle recognition (SRP) secretion pathway, are described.

Iron heme cofactors are single-electron transport moieties that play a crucial role in respiration. While oxygen is the electron acceptor of choice in aerobic atmospheres, microorganisms that live in anaerobic environments utilize other molecules with similarly high reduction potentials. *S. oneidensis* can utilize numerous terminal electron acceptors, including nitrite, dimethylsulfoxide and even uranium, thanks to a particularly rich array of multi c-heme respiratory proteins. Understanding of how the midpoint potentials and heme arrangements within the proteins influence these exotic respiratory processes is of interest in the fields of bioremediation and fuel development.

# TABLE OF CONTENTS

<b>1</b>	<b>Introduction</b> .....	<b>1</b>
1.1	Overview .....	1
1.2	Spectroscopic and physical methods .....	5
1.2.1	UV-vis and Spectropotentiometry.....	5
1.2.2	Electron Paramagnetic Resonance (EPR) .....	9
1.3	Electronic and magnetic properties of hemes in CcNiR and related proteins.....	18
1.3.1	Peripheral hemes 2 and 5 .....	20
1.3.2	Active site heme 1 .....	23
1.3.3	Inner core hemes 3 and 4 .....	25
1.4	Summary.....	26
1.5	References .....	27
<b>2</b>	<b>Correlations between the electronic properties of <i>S. oneidensis</i> CcNiR and its structure: effects of heme oxidation state and active site ligation, and implications for the CcNiR reaction mechanism</b> .....	<b>32</b>
2.1	Background .....	32
2.2	Materials and Methods .....	33
2.2.1	General materials.....	33
2.2.2	Protein purification and handling .....	34
2.2.4	UV/Vis spectropotentiometric titrations of CcNiR.....	38
2.2.5	Electron paramagnetic resonance (EPR) titrations of CcNiR.....	38
2.3	Results .....	40
2.3.1	Effect of strong-field ligands on the EPR spectrum of CcNiR .....	40

2.3.2	Effect of cyanide on the electrochemical properties of CcNiR .....	46
2.3.3	UV/Vis spectropotentiometry of the H268M <i>S. oneidensis</i> CcNiR mutant ..	53
2.3.4	Effect of nitrite on the electrochemical properties of CcNiR .....	58
<b>2.4</b>	<b>Discussion .....</b>	<b>63</b>
2.4.1	Titration of CcNiR with cyanide and nitrite.....	63
2.4.2	Order of heme reduction in CcNiRs from different organisms.....	65
2.4.3	Nitrite reduction at the CcNiR active site .....	72
<b>2.5</b>	<b>References .....</b>	<b>76</b>
<b>3</b>	<b>Nitrite and sulfate binding to CcNiR .....</b>	<b>81</b>
<b>3.1</b>	<b>Background .....</b>	<b>81</b>
<b>3.2</b>	<b>Methods .....</b>	<b>82</b>
3.2.1	Purification.....	82
3.2.2	Sulfate titrations.....	82
3.2.3	Nitrite titration (EPR) of sulfate free CcNiR solution .....	83
<b>3.3</b>	<b>Results .....</b>	<b>84</b>
3.3.1	Sulfate titrations monitored by UV-Vis.....	84
3.3.2	Nitrite titrations of sulfate free CcNiR monitored by EPR .....	86
<b>3.4</b>	<b>Discussion .....</b>	<b>90</b>
<b>3.5</b>	<b>References .....</b>	<b>93</b>
<b>4</b>	<b>Octaheme tetrathionate reductase .....</b>	<b>94</b>
<b>4.1</b>	<b>Background .....</b>	<b>94</b>
4.1.1	Subcloning and expression .....	94
4.1.2	Activity assays.....	99
4.1.3	Optimization of OTR expression .....	101
4.1.4	Streptomycin sulfate additions .....	102

4.1.5	Ammonium sulfate fractionation .....	102
4.1.6	Chromatographic separation using octyl-sepharose hydrophobic interaction chromatography .....	103
4.1.7	Chromatographic separation using hydrophobic interaction, anion exchange and size exclusion columns in series .....	104
<b>4.2</b>	<b>Results .....</b>	<b>106</b>
4.2.1	Subcloning and expression .....	106
4.2.2	Activity assays.....	107
4.2.3	Analysis by octyl sepharose separation .....	108
4.2.4	Streptomycin sulfate additions .....	109
4.2.5	Ammonium sulfate fractionation .....	110
4.2.6	Serial column chromatography.....	111
<b>4.3</b>	<b>Discussion .....</b>	<b>112</b>
<b>4.4</b>	<b>References .....</b>	<b>116</b>
<b>5</b>	<b><i>Shewanella oneidensis</i> Lon Deletion.....</b>	<b>117</b>
<b>5.1</b>	<b>Background .....</b>	<b>117</b>
<b>5.2</b>	<b>Methods .....</b>	<b>120</b>
5.2.1	Suicide construct.....	120
5.2.2	Conjugation (mating).....	123
<b>5.3</b>	<b>Results and Conclusion .....</b>	<b>124</b>
<b>5.4</b>	<b>References .....</b>	<b>129</b>
<b>6</b>	<b>DsbA leader peptide mediated translocation of tagged CcNiR in <i>S. oneidensis</i>.....</b>	<b>131</b>
<b>6.1</b>	<b>Background .....</b>	<b>131</b>
<b>6.2</b>	<b>Materials and Methods .....</b>	<b>133</b>
6.2.1	Leader sequence replacement.....	133
6.2.2	Expression and 6XHis-tag integrity assessment.....	137

<b>6.3 Results and Discussion</b> .....	<b>138</b>
6.3.1 DsbA leader sequence insertion .....	138
6.3.2 Expression and Ni-NTA binding .....	138
<b>6.4 References</b> .....	<b>141</b>
<b>ACKNOWLEDGMENTS</b> .....	<b>142</b>
<b>CURRICULUM VITAE</b> .....	<b>143</b>

## TABLE OF FIGURES

- Figure 1.1 (A) The CcNiR dimer from *S. oneidensis*, showing the amino acid backbone in cartoon form and the hemes in stick form; the active site heme is shown in red, while the electron transfer hemes are in green. (B) Heme arrangement within one of the CcNiR subunits, showing the numbering system used in the text..... 2
- Figure 1.2 The UV-vis spectra of CcNiR from *S. oneidensis*<sup>10</sup>. Fully oxidized in blue and fully reduced in red. .... 6
- Figure 1.3 The diagram represents the energy splitting between the excited  $m_s=1/2$  and ground  $m_s=-1/2$  states as the static magnetic field increases.  $g$  is the Lande factor,  $h$  is Planck's constant,  $\nu$  is the frequency of the isolating magnetic field perpendicular to the static magnetic field,  $\mu_b$  is the Bohr magneton. The initial spin is pictured with a 45-degree tilt to represent that the two levels are degenerate in the absence of magnetic field..... 11
- Figure 1.4 The diagram represents the octahedral ligand-field splitting effect on the Fe(III) 3d orbitals. The strength of the ligand field in comparison with the strength of the pairing energy will determine the total spin configuration. This difference is detectable by EPR spectroscopy. .... 13
- Figure 1.5 The effects of strong octahedral ligand-field splitting followed by tetragonal and rhombic distortions on the energies of the d spatial orbitals. The bold labels are the terms for the EPR signals characteristic of these distortions. These terms are used throughout this thesis..... 14
- Figure 1.6 (A) Two axial histidines aligned in plane with each other and only with the y axis, lower the symmetry of the complex. (B) Histidines aligned perpendicularly to each other and equally with the y and x axes, preserve the symmetry..... 15
- Figure 1.7 Heme-heme and heme pyrrole nitrogen dihedral angles for Table 1.1 were measured as illustrated here. The pyrrole ring I was selected to serve as the reference in both cases. The central atom was used as the second atom for dihedral angle calculations all measurements. .... 22
- Figure 2.1 (A) The TEV tag, polyglycine linker and histidine tag were added to the CcNiR gene sequence at carboxyl terminus by serial PCR reaction. The forward primer CcNiRTEVf was used for all reactions. The primer sequences are listed in Table 2.2. Products from each reaction were cleaned by PCR clean up kit before subsequent amplification. Once the addition was complete, the pHSG298 and the final product were double-digested with EcoRI and PstI. The small DNA fragments that were generated by the digestion were removed using PCR clean up kit. The insert - CcNiR 6XHis and pHSG298 were ligated using T4 DNA ligase (HC) from Thermo. A maxi

prep of the construct was prepared and the sequence was confirmed by Cancer Research Center DNA sequencing facility in Chicago. (B) Construction of 10X histidine tagged CcNiR by insertion mutagenesis. The five-prime phosphorylated primers (see Table 2.2) were used in PCR to amplify the CcNiR6XHisPHSG298 construct adding four extra histidine residues. The reaction product was cleaned with PCR cleanup kit and ligated. A maxi prep was prepared for sequencing and subsequent electroporation into <i>S. oneidensis</i> TSP-C. This construct was used in site directed mutagenesis. ....	36
Figure 2.2 EPR spectral changes observed when a 25 $\mu$ M CcNiR dimer solution is exposed to varying concentrations of cyanide. (A) Full spectral range where signals are observed; (B) magnified view of the signals that remain after addition of the first 25 $\mu$ M aliquot of cyanide.....	42
Figure 2.3 EPR spectral changes observed when a 25 $\mu$ M ccNiR dimer solution is exposed to varying concentrations of nitrite. (A) Full spectral range where signals are observed; (B) magnified view of the signals that remain in the presence of 200 $\mu$ M nitrite.....	43
Figure 2.4 Comparison of the EPR spectra obtained in the presence of 100 $\mu$ M cyanide (blue trace) and 2.7 mM nitrite (red trace). The residual difference between the two spectra is plotted in black below the full traces. ....	45
Figure 2.5 The five hemes from one of the ccNiR protomers. The dashed vertical line represents the interface for the complete dimer. The hemes are color-coded to match spectral assignments made in the main text and Table 2.3. Histidine 268 is labeled. ....	45
Figure 2.6 (A) UV/Vis spectral changes obtained upon exposing a solution initially containing 23.3 $\mu$ M of fully oxidized CcNiR dimer and 75 $\mu$ M cyanide to applied potentials of -27, -137, -217, -317, and -487 mV vs the standard hydrogen electrode (SHE). Solid lines show the experimentally obtained data, whereas the dashed red lines were calculated from least-squares fitting to five Nernstian potentials, as described in ref. 4. (B) Blue circles: an absorbance difference vs. applied potential slice taken at 426 nm from the spectra of part (A); green circles: an equivalent slice obtained from a global fit of the spectral changes accompanying potentiometric reduction of a 23.3 $\mu$ M solution of CcNiR dimer in the absence of cyanide. In both cases the solid red traces are the least-squares best fits obtained from a global analysis of the data. ....	47
Figure 2.7 (A) Extinction coefficient difference spectra corresponding to each of the reduced CcNiR species $C_{red1} - C_{red5}$ (Scheme 2.1), as calculated by the procedure described in ref. 4 for the data obtained in the presence of cyanide (Figure 2.6a). (B) Calculated concentrations of $C_{red1} - C_{red5}$ as a function of the applied potential (vs SHE) for the same data. Both here and in (A) the traces are color coded to match the hemes in Figure 2.5 to which	

they are tentatively assigned (see text for details). Note: the values of $C_{\text{red1}} - C_{\text{red5}}$ are given in terms of dimer concentrations, but those of $\Delta\varepsilon$ are given in terms of the protomer concentrations, to allow direct comparison with earlier reports where this was done (for example in refs. 3 and 4). The amplitudes for the $\Delta\varepsilon$ spectra corresponding to the CcNiR dimer will be twice those shown in (A). .....	48
Figure 2.8 X-band EPR spectra obtained for a solution initially containing 25 $\mu\text{M}$ of fully oxidized CcNiR dimer and 100 $\mu\text{M}$ cyanide, upon exposing it to the applied potentials shown (vs SHE).....	50
Figure 2.9 X-band EPR spectra obtained for a solution initially containing 25 $\mu\text{M}$ of fully oxidized CcNiR dimer in the absence of any strong-field ligands, upon exposing it to the applied potentials shown (vs SHE). .....	53
Figure 2.10 UV/Vis spectral changes obtained upon exposing a solution initially containing 19.9 $\mu\text{M}$ of fully oxidized CcNiR <sub>H268M</sub> dimer to applied potentials of 0, -100, -180, -270, and -500 mV vs SHE. Solid lines show the experimentally obtained data, whereas the dashed red lines were calculated from least-squares fitting to four Nernstian potentials. ....	55
Figure 2.11 (A) Extinction coefficient difference spectra corresponding to spectroscopically distinct products of reduction for the mutant CcNiR <sub>H268M</sub> for the data shown in Figure 2.10. (B) Equivalent extinction coefficient difference spectra obtained for CcNiR <sub>wt</sub> ; both (A) and (B) were obtained in the absence of strong-field ligands. The spectra are color-coded to match the hemes in Figure 2.5, to which they are tentatively assigned. $\Delta\varepsilon_{\text{red1}}$ in (A) is drawn in both blue and red because in the mutant this spectral component is believed to arise from reduction of both hemes 1 and 5. Note the much-diminished red-shift in the two lowest-potential components of CcNiR <sub>H268M</sub> , as compared to those of CcNiR <sub>wt</sub> . ....	57
Figure 2.12(A) UV/Vis spectral changes obtained upon exposing a solution initially containing 29 $\mu\text{M}$ of fully oxidized CcNiR <sub>wt</sub> dimer and 5 mM nitrite to progressively lower potentials. Solid blue lines show the experimentally obtained data, whereas the dashed red lines were calculated from least-squares fitting with two Nernstian 2-electron reduction events, and one spectral component. (B) Blue circles: an absorbance difference vs. applied potential slice taken at 425 nm from the spectra of part (A); solid red line: least-squares best fit obtained from global analysis of the data with two Nernstian 2-electron reduction events; dotted green line: least-squares best fit obtained from global analysis of the same data with two Nernstian 1-electron reduction events. ....	59
Figure 2.13 X-band EPR spectra obtained for a solution initially containing 25 $\mu\text{M}$ of fully oxidized CcNiR dimer and 5 mM nitrite, upon exposing it to the applied potentials shown (vs SHE).....	61

Figure 2.14 Space-filling view of the CcNiR surface in the vicinity of heme 2 (purple) for (A) the <i>S. oneidensis</i> enzyme; and (B) the <i>E. coli</i> enzyme. The yellow arrows point to the heme propionate that is solvent-exposed in the <i>S. oneidensis</i> enzyme, but hydrogen-bonded to Arg 201 in the <i>E. coli</i> enzyme. ....	67
Figure 3.1 Difference UV-Vis spectra of CcNiR titrated with sulfate. Arrows indicate the direction of change. The most profound change is at 411 nm. While not as profound, a second change in absorbance can be seen at 310nm. Two isosbestic points are seen at 350 and 460 nm. ....	85
Figure 3.2 Change in absorbance at 411 nm with respect to sulfate concentration. The black squares and red triangles are titration points with 0.1 M with 0.5 M sulfate respectively. The red line is the fit of the data to equation 2, which yielded optimized parameters $K_d = 2.87$ mM and $\Delta A_{\max} = -0.05$ . ....	85
Figure 3.3 (A) EPR spectrum of resting CcNiR. (B) EPR spectrum of CcNiR in the presence of 50 $\mu$ M nitrite. (C) Difference between A and B. ....	87
Figure 3.4 Net differences between <i>g</i> values as indicated in text and in Figure 3.5 below. ....	87
Figure 3.5 The overlaid spectra conveys the entire titration of sulfate free CcNiR. The up and down arrows indicate the <i>g</i> values that increase and subsequently decrease as the concentration of nitrite increases (see Figure 3.4). ....	88
Figure 3.6 The overlaid spectra of sulfate-containing CcNiR solutions as they are titrated with nitrite from Chapter 2 replotted here for convenience. The arrows indicate the <i>g</i> -values. The notable difference between these and the spectra in Figure 3.5 is that here only two distinct, decreasing signals observed and not intermediates. ....	89
Figure 3.7 The edge-to-edge distances between hemes, and select imidazole rings of the axial histidine ligands, for hemes 1, 3 and 4 of CcNiR. ....	90
Figure 4.1 pMMB503EH is a broad-host range mobilize-able expression vector based on the rsf1010 plasmid <sup>5</sup> . Rep genes, together with F and E genes, act on the origin of replication OriV that allows for replication in gram negative bacteria. Mob genes act on OriT to initiate conjugative transfer; however, for successful transfer, Tra genes that encode for proteins that make pili also need to be provided. The plasmid carries resistance to streptomycin (SmA and SmB). The polycloning site that allows one to subclone the gene for expression is located downstream of the tac promoter, which is a synthetic promoter that has a higher affinity for RNA polymerase than the lac promoter. The tac promoter also contains a lac repressor region where the repressor protein lacIq suppresses gene expression in the	

absence of IPTG or allolactose (see main text). LacIq is expressed constitutively under the lac promoter.....	98
Figure 4.2. The PCR cycling parameters used to check for a ~1.4 kb OTR fragment in the colonies purportedly containing the OTR-pMMB503EH construct. The PCR mixture used is described in the text.....	98
Figure 4.3 A sample activity assay. The segment up to ~0.3 minutes (min) is absorbance at 600nm of 50mM HEPES, ~80µM MV <sub>red</sub> and OTR prior to addition of oxidizing substrate. The latter is added at the time shown by the downward arrow. The dip in absorbance is due to lifting of the cuvette during sample mixing. The initial rate is taken from the slope of the linear portion of the trace that follows substrate addition.....	100
Figure 4.4 Balanced chemical equations for reactions reported for OTR in previous publications <sup>3</sup> .....	100
Figure 4.6 Nitrite, hydroxylamine and tetrathionate reductase activities, as separated by octyl sepharose chromatography of lysate with 30% ammonium sulfate from NS_432f. The protein was bound to the column at 30% ammonium sulfate in 50mM HEPES pH=7.0 and 1mM EDTA. 6mL fractions were collected during 600mL gradient from 30% to 0% ammonium sulfate.....	109
Figure 4.7 Effect of adding progressively larger amounts of streptomycin sulfate to NS_432f clarified cell lysate. Streptomycin sulfate was added to a slowly stirring solution as described in methods. The absorbance at 410 nm was measured and correlated to hydroxylamine reductase activity. For convenience in plotting the two disparate quantities on the same graph, absolute values were converted into percentages where the activity and A410 without streptomycine are taken as 100%.....	110
Figure 4.8. (A) Ammonium sulfate saturation. The activity was measured as described in methods. 100% activity was taken as the activity of the clarified NS_432f lysate. (B) Lysate in this purification trial contains 190,000 EU; 25% ammonium sulfate supernatant (Sn) 201,000 EU; 50% ammonium sulfate supernatant contains only 57,400 EU. Only 99,500 EU could be re-dissolved out of the pellet (PI). The re-dissolved suspension had to be centrifuged to remove some insoluble debris.....	111
Figure 4.9 The plots of enzymatic activities (left) and A410/A280 ratios (right) of the pooled samples obtained from each chromatographic step. Left: The blue bars are activities immediately before the column, and the red bars after. The samples were kept in the refrigerator overnight before the next column. Right: A410/A280 ratios as the measure of heme content per protein in the mixture.....	112

Figure 4.10 Surface representation of OTR. The five-coordinate active site heme 2 is represented by blue sticks, while the solvent-accessible cysteine is rendered as green sticks. ....	115
Figure 5.1 Comparison of the three operons containing lon protease as identified by the sequence homology. Their positions within their genomes are indicated by a graded line where K stands for thousand. <i>Shewanella oneidensis</i> (green) and <i>E. coli</i> K-12 (red) have the uninterrupted operons. <i>E. coli</i> (green) BL21DE3 has contains a transposase between <i>clpX</i> and <i>lon</i> sequences. The transposase is potentially responsible for observed Lon deficiency in the BL21DE3 strain. ....	118
Figure 5.2 A general scheme for the construction of Lon protease pDS132 vector that contains flanking regions of Lon protease from <i>S. oneidensis</i> . Fragment A was amplified with ns723a and ns713a primers, and fragment B with ns723b and 713b primers. For detailed description of the primers see Table 5.1. pDS132 was double digested with <i>Sall</i> and <i>SphI</i> , fragment A with <i>Sall</i> , and fragment B with <i>SphI</i> . The digested fragments and vector were ligated together. The linear ligation product was digested with <i>PstI</i> and circularized by ligation. A four amino acid sequence MILQ with two stop codons was placed in between the fragments. ....	121
Figure 5.3 Homology driven integration and resolution of a vector. (A) Homologous region of a plasmid is aligned with that of the <i>S. oneidensis</i> genomic DNA. Shown is the alignment of the A fragment that would lead to a five prime integration. Alignment of B fragments would lead to three-prime integration . (B) Example of the five-prime and the three prime integration of suicide construct and the possible resolution combinations. If resolution results from alignment of regions linked by the blue line, a deletion arrangement will result. If resolution results from alignment of regions linked by the red line, a wild type arrangement will be maintained. (C) Deletion and wild type arrangements in the Lon containing operon. ....	126
Figure 6.1. Comparison of leader peptides that were tested in this study. Underlined in red is the DsbA portion of the peptide from the <i>S. oneidensis</i> locus SO_0333, and in cyan the leader peptide from <i>S. oneidensis</i> ' small tetraheme-c locus SO_2727. In blue are the signal peptidase recognition sites, with arrows indicating the exact cleavage site. In green are the hydrophobic residues. In the STC1p these residues are interspersed. DsbAlp contains a solid hydrophobic core; the property responsible for the recognition of this leader peptide by SRPs 3,4. ....	132
Figure 6.2. (A) graphic depiction of primer annealing to the template. The primers NS_815a and b (Table 6.1) bind outside of STC1p, and carry the sequence that codes for the DsbAlp. (B) cycling parameters for the PCR. Each round will amplify the entire plasmid. ....	133

Figure 6.3. Lane 1: EZ-run pre-stained RecA ladder from Fisher Scientific. Lane 2: cleared lysate from  $\Delta$ MtrA/ $\Delta$ DegP\_DsbA/pCcNiR. Lane 3: cleared lysate from *S. oneidensis*  $\Delta$ MtrA/ $\Delta$ DegP..... 140

## TABLE SCHEMES

Scheme 2.1 Reduction of fully oxidized CcNiR (Ox). $C_{red1}$ – $C_{red5}$ refer to the one-electron-reduced to five-electron-reduced species, respectively. ....	46
Scheme 2.2 An $\{Fe(NO)\}^7$ species may form in two ways; concerted or stepwise reduction of iron nitrite complex. This study suggests that concerted mechanism is more likely. ....	62
Scheme 2.3 In the experiments described herein active site reduction in the presence of nitrite appears to proceed via Path 1. Under physiological conditions it will likely proceed via path 2.....	73

## TABLE OF EQUATIONS

Equation 1.1 The Stokes' equation correlates a frictional coefficient $f$ with a molecular radius $r$ and a medium of viscosity $\mu$ . .....	7
Equation 1.2 The Einstein-derived relation between the diffusion coefficient $D$ and the frictional coefficient $f$ . $k$ is the Boltzmann constant and $T$ is temperature in Kelvin. ....	7
Equation 1.3 Red is the concentration of reduced species. Ox is the concentration of oxidized species. $n$ is the number of electrons transferred in the reaction. $F$ is the Faraday constant, 96485 C/mole. $T$ is the temperature in Kelvin. $R$ is the gas constant, 8.314 J/mole K. $\epsilon^\circ$ is the midpoint redox potential, and $\epsilon_{app}$ is the applied potential. ....	9
Equation 1.4 Red is the concentration of reduced protein. $Q$ is the exponential term from Equation 1.3. $C_t$ is the total protein. ....	9
Equation 1.5 A chemical process by which a completely oxidized species undergoes two sequential redox events. The events are signified by the arrows. ....	9
Equation 1.6 Red <sub><math>m</math></sub> stands for the concentration of $m^{\text{th}}$ reduced species. The numerator contains $m$ $Q$ terms. $Q$ terms represent the exponential terms for each redox couple. The denominator remains the same for all Red <sub><math>m</math></sub> and contains all $Q$ terms. ....	9
Equation 1.7 $A_{exp}$ is the experimental absorbance, Red is the concentration of the reduced species obtained by setting the midpoint potential to a specific value, and $l$ is the path-length of the cuvette. $E_{calc}$ is the extinction coefficient calculated based on the specific value of the midpoint potential. $A_{calc}$ is the calculated absorbance. ....	9
Equation 3.1 $n$ is the total number of microliters of the sulfate stock added to the initial 1mL solution of CcNiR. ....	83
Equation 3.2 $\Delta A$ is the change in absorbance at 411 nm, $\Delta A_{max}$ is the maximum change in absorbance at 411 nm, and $K_d$ is the dissociation constant. ....	83
Equation 4.1 $AU_{600}/\text{min}$ is the change in absorbance per minute. $13600 \text{ (M}^{-1}\text{cm}^{-1}\text{)}$ is the $MV_{red}$ extinction coefficient. 0.001L is the volume of the assay. $\#e^-$ stands for number of electrons transferred in order to reduce the substrate to product. $\mu\text{moles}/\text{min}$ are the EU in the assay. ....	101

## TABLE OF TABLES

Table 1.1 <i>E. coli</i> $\phi$ values were obtained from Bamford et al. <sup>7</sup> . The angles between the imidazoles, and imidazoles and porphyrin, were measured using the “get dihedral” function in PyMol and the crystal structure published in Clarke <i>et al.</i> <sup>41</sup> . <i>D. desulfuricans</i> $\phi$ values were obtained from a combination of studies <sup>32-34</sup> . The angles were measured by the same method as with <i>E. coli</i> using the structure published in by Cunha <sup>8</sup> . See Figure 1.7 for a more thorough description of the angle measurements. ....	21
Table 2.1 Mediators used for spectropotentiometry .....	34
Table 2.2 Primers used to generate 10X histidine tagged CcNiR in pHSG298 construct. Detailed explanation of the process is illustrated in Figure 2.1.....	37
Table 2.3 Midpoint redox potentials for wild type CcNiR (CcNiR <sub>wt</sub> ) under a variety of conditions, and for the H268M mutant (CcNiR <sub>H268M</sub> ). Colors suggest possible assignments to the hemes in Figure 4, but see text for more discussion on this point. ....	49
Table 5.1. Upper contains all the primers sequences used in this study and their descriptions in terms of priming regions on <i>S. oneidensis</i> ' genome and orientations, and the relevant endonuclease sites that they contain. The assignments are given in reference to Figures 5.2 and 5.3. Lower are bacterial cultures that were used in this study.....	122
Table 6.1. Primers, constructs and cultures used in this study .....	136

# 1 Introduction

## 1.1 Overview

Cytochrome *c* nitrite reductase (CcNiR) is a soluble periplasmic bacterial enzyme that catalyzes the 6-electron reduction of nitrite to ammonia (ammonification) <sup>1</sup>, and can also catalyze reduction of NO or hydroxylamine to ammonia <sup>2,3</sup>. The active protein is a homodimer (Figure. 1.1A). CcNiR's protomeric molecular masses range from 52 to 65 kDa depending on the organism from which it is obtained <sup>4-10</sup>. In all homologues studied so far each protomer contains five *c*-type hemes. Four of the hemes (hemes 2-5, Figure 1.1B) are six-coordinate, *bis*-histidine ligated and low-spin. The remaining heme (heme 1) is five-coordinate high-spin, and unique among *c*-hemes in having a lysine residue in the proximal axial position (Figure. 1.1B). The hemes in CcNiR are closely packed, with iron-iron distances of <13 Å, which facilitates rapid inter-heme electron transfer. Thus, the 6-coordinate hemes appear to act as an electron wire that efficiently carries the electrons from the enzyme's external physiological electron donor to the five-coordinate active site where nitrite reduction occurs <sup>4-10</sup>.

Ammonifying bacteria use CcNiR as the terminal electron acceptor in anaerobic respiration <sup>1,11,12</sup>, and this appears to be the enzyme's primary role. However, there is also some evidence that CcNiR has a role in mitigating

oxidative and nitrosative stress, not just in response to nitrite, but also to NO, hydroxylamine and even hydrogen peroxide<sup>2,6,13,14</sup>. This hypothesis has been reinforced by the isolation of CcNiR and a related nitrite reducing multi-heme protein from bacteria that are incapable of dissimilatory nitrite reduction<sup>6,14</sup>.

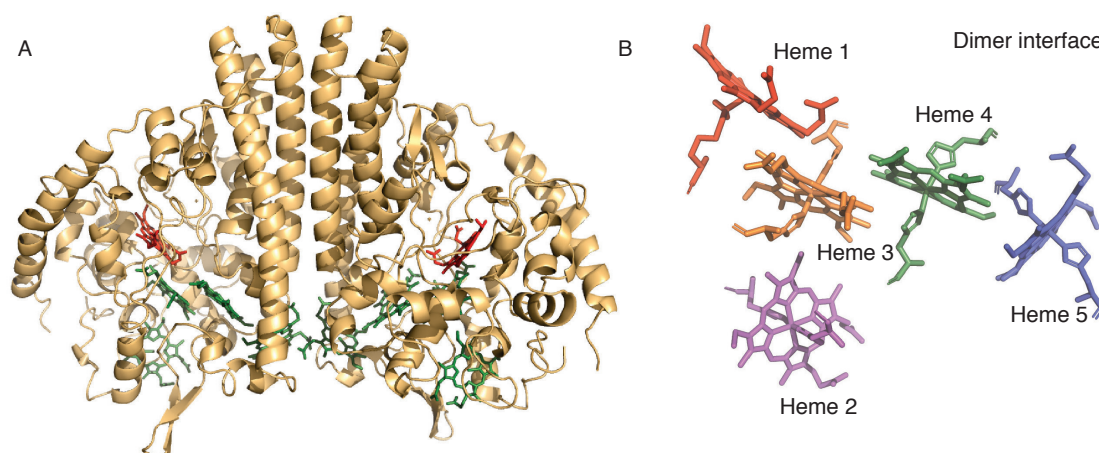


**Figure 1.1 (A) The CcNiR dimer from *S. oneidensis*, showing the amino acid backbone in cartoon form and the hemes in stick form; the active site heme is shown in red, while the electron transfer hemes are in green. (B) Heme arrangement within one of the CcNiR subunits, showing the numbering system used in the text.**

Many aspects of the heme arrangement within CcNiR are replicated in other proteins<sup>15,16</sup>, and how a common structural motif is optimized for specialized roles is a subject of much investigation. For example, comparative mechanistic studies of CcNiR and hydroxylamine oxidoreductase (HAO<sup>\*</sup>), a multi-heme enzyme which catalyzes the oxidation of hydroxylamine to nitrite in ammonia oxidizing bacteria,<sup>11,12</sup> have been carried out in order to understand how CcNiR and HAO have been evolutionarily optimized to catalyze similar reactions in opposite directions<sup>10,17-19</sup>.

\* The currently accepted name for this enzyme (EC 1.7.2.6) is hydroxylamine dehydrogenase, while its correct systematic name is hydroxylamine:ferricytochrome-c oxidoreductase. However, the old abbreviation HAO has been in use for nearly 50 years, and will be employed here in the interest of continuity.

Ultimately, meaningful interpretation of mechanistic data for CcNiR and HAO requires that the redox properties of the enzymes under reaction conditions be thoroughly understood. The primary focus of the project described herein was to characterize the redox properties of CcNiR from the bacteria *Shewanella oneidensis*. To this end, Chapter 2 of this dissertation presents UV/Vis and EPR spectropotentiometric studies of CcNiR from *S. oneidensis* in the presence of both weak-field and strong-field ligands, including the physiological substrate nitrite. Chapter 2 also explores the interaction of oxidized CcNiR with nitrite and cyanide using EPR spectroscopy.

While carrying out the investigations described in Chapter 2, it became apparent that the UV/Vis and EPR spectra of CcNiR varied as a function of the sulfate concentration present in the buffers. This phenomenon was investigated independently, and is described in Chapter 3.

When this project was first begun, its focus was not on CcNiR, but rather on another *S. oneidensis* multi-heme protein known as octaheme tetrathionate reductase (OTR). At the time, the structure of *S. oneidensis* CcNiR was still unavailable, whereas that of *S. oneidensis* OTR had already been solved. This, coupled to the fact that OTR is a monomer whereas CcNiR is a dimer, made attractive a comparative study of the nitrite and hydroxylamine reductase activities of the two enzymes. Chapter 4 describes the work done on OTR, which included the optimization of an OTR expression system and partial purification and characterization of the enzyme.

A major challenge when doing biophysical investigations of proteins such as the ones described herein is to obtain sufficient material for the often protein-intensive experiments. In 2012 Youngblut *et al.* reported on a high-yield expression system for wild-type *S. oneidensis* CcNiR. However, because this expression system itself uses *S. oneidensis*, a small fraction of the CcNiR it produces comes from genomic DNA expression. When only wild type CcNiR was desired this expression system was ideal. However, one of the experiments described in Chapter 2 required a mutant of the enzyme, as do many experiments planned for the future. For such experiments the genomically-expressed wild type constitutes an impurity that would likely be difficult to separate. For this reason, an important secondary objective of this dissertation was the development of expression systems for His-tagged CcNiR, which could be readily separated from the wild type.

Preliminary attempts at expressing tagged CcNiR and OTR in *S. oneidensis* revealed that the proteins tagged at the carboxy-terminus were susceptible to tag proteolysis. Consequently, Chapters 5 and 6 describe attempts to modify the *S. oneidensis* to eliminate this proteolysis. An attempt to delete a gene that codes for the major heat-shock protease (Lon) is described in Chapter 5. In Chapter 6 a leader peptide that translocates CcNiR to the periplasm co-translationally was used to protect the peptide from the cytoplasmic proteases.

The remainder of this chapter provides an introduction of spectroscopic and physical methods used to study CcNiR from *S. oneidensis*, followed by a

review of CcNiR's structural and spectroscopic properties as they were understood at the start of the project. In the review the questions that this dissertation sought to answer are introduced.

## 1.2 Spectroscopic and physical methods

### 1.2.1 UV-vis and Spectropotentiometry

Porphyrins possess a characteristic strong absorption band between 400 and 500 nm termed Soret band, and less prominent absorption bands between 500 and 600 nm, in their ultraviolet-visible absorption (UV-vis) spectra. Because in metalloporphyrins these bands are very sensitive to the metal oxidation state and ligand environment, UV-Vis spectroscopy is a convenient method for studying proteins that contain heme cofactors. The Soret band and the less prominent absorption bands between 500 and 600 nm arise from the  $\pi$  electron transitions from the highest occupied to the lowest unoccupied molecular orbitals of the porphyrin ring.<sup>20</sup> The central metal affects the energies and intensities of these transitions. Small but noticeable changes can occur when ligands such as cyanide in Chapter 2, and sulfate in Chapter 3, bind to or dissociate from the axial position on the central metal. More profound changes occur in the iron hemes when the metal changes oxidation state from Fe(III) to Fe(II) (Figure 1.2). The reduction shifts the Soret band to longer wavelengths and increases its intensity. This effect is used in Chapter 2 to quantitatively determine the hemes' midpoint potentials in CcNiR from *S. oneidensis* using protein spectroelectrochemistry.

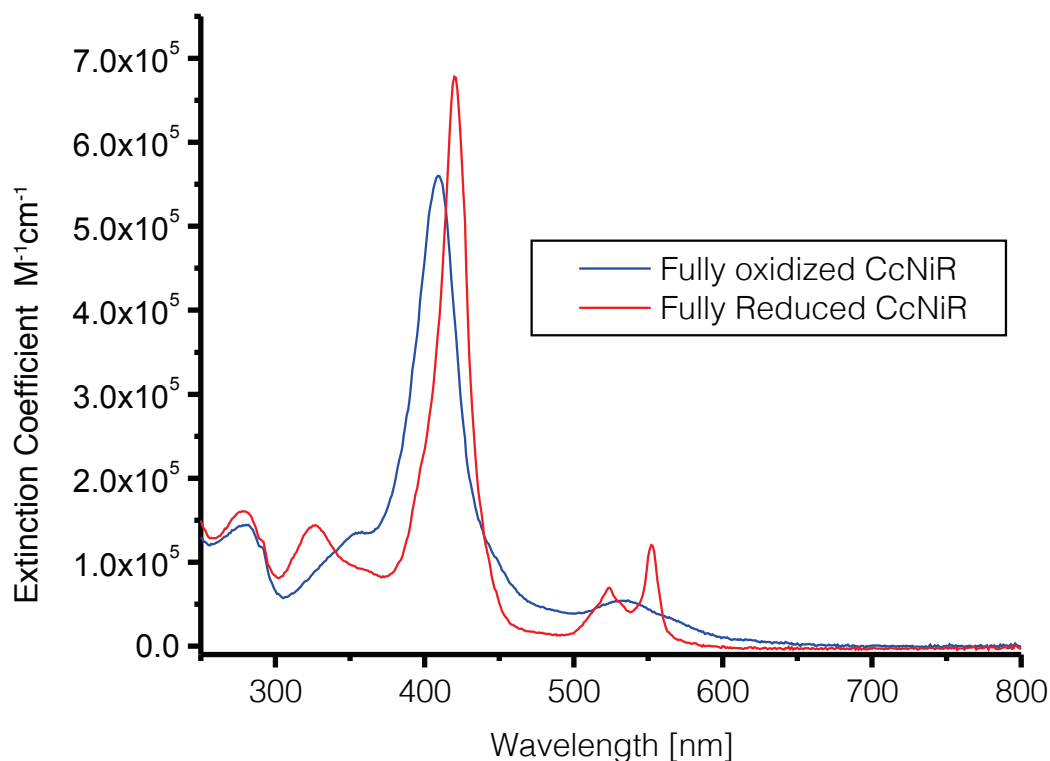


**Figure 1.2** The UV-vis spectra of CcNiR from *S. oneidensis*<sup>10</sup>. Fully oxidized in blue and fully reduced in red.

Spectroelectrochemistry combines the controlled potential electrolysis (CPE) experiment with a spectroscopy that is suitable for determining the analyte's spectral characteristics in different redox states.

The CPE experimental setup requires working and auxiliary electrodes that perform the reactions opposite each other. For example, when a working electrode reduces the sample in the reaction compartment, the auxiliary electrode performs oxidation in a separate compartment. In addition, a reference electrode monitors the potential during an experiment. References<sup>21,22</sup> provide examples of the apparatuses that can be used to combine CPE with UV-vis spectroscopy. The current versus time is observed at a fixed potential during an

experiment. When the current no longer changes and is essentially zero, the reaction is complete. In a spectroelectrochemical experiment a spectrum of the sample should be recorded at this point.

A challenging aspect of doing a CPE experiment on proteins is that CPE is diffusion limited. The Stokes equation (Equation 1.1) gives a frictional coefficient that is directly proportional to the molecular radius, which in turn is inversely proportional to the diffusion coefficient of the redox-active molecule (Equation 1.2). Hence, the diffusion coefficient of a molecule is inversely proportional to its radius. Proteins have relatively large molecular radii so an oxidation or reduction at electrode surfaces is impractically slow. For this reason in protein CPE experiments a set of smaller molecules (mediators) that can rapidly undergo reversible redox reactions are used to shuttle the electrons between the working electrode and protein. The set is chosen such that the mediators' midpoint potentials are fairly close to one another, and cover a desirable span of potentials. One such set is shown in Chapter 2, Table 2.1. This setup shortens the protein CPE experiments to reasonable timescales.

**Equation 1.1 The Stokes' equation correlates a frictional coefficient  $f$  with a molecular radius  $r$  and a medium of viscosity  $\mu$ .**

$$f = 6\pi\mu r$$

**Equation 1.2 The Einstein-derived relation between the diffusion coefficient  $D$  and the frictional coefficient  $f$ .  $k$  is the Boltzmann constant and  $T$  is temperature in Kelvin.**

$$D = \frac{k T}{f}$$

A detailed derivation of the Nernst equation for a protein with five distinct midpoint potentials was published before in Youngblut *et al.*,<sup>10</sup> and a similar method is used to fit the data in Chapter 2. The method is briefly described below for completeness. Equation 1.3 is an exponential form of the Nernst equation. The right side of this equation can be abbreviated as Q. Thus, Q is a function of the applied potential. The total amount of protein is measured at the beginning of the experiment, when all of it is fully oxidized. In Chapter 2, all CcNiR samples were initially oxidized. For UV-vis spectropotentiometry, the applied potentials were lowered in 10 mV increments so as to reduce the oxidized protein. Equation 1.4 can be used to solve for the concentration of the reduced species in a system with a single midpoint potential. However, this equation can be easily expanded to be applicable to systems with more than one midpoint potential, such as shown in Equations 1.5 and 1.6 for the case of two sequential reductions. A series of equations that have the same denominator, and a different numerator portion can be generated for each reduced species (Equation 1.6). These equations can be combined with the Beer-Lambert Law, Equation 1.7, to fit the spectropotentiometric data by adjusting the midpoint potentials until the calculated absorbances match the experimental ones. The method can be expanded to fit many midpoint potentials, and the entire spectral width, by organizing the data into matrices as was done in Youngblut *et al.*<sup>10</sup>, and in Chapter 2.

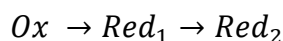
Equation 1.3  $Red$  is the concentration of reduced species.  $Ox$  is the concentration of oxidized species.  $n$  is the number of electrons transferred in the reaction.  $F$  is the Faraday constant, 96485 C/mole.  $T$  is the temperature in Kelvin.  $R$  is the gas constant, 8.314 J/mole K.  $\varepsilon^\circ$  is the midpoint redox potential, and  $\varepsilon_{app}$  is the applied potential.

$$\frac{Red}{Ox} = e^{\frac{nF}{RT}(\varepsilon^\circ - \varepsilon_{app})} \text{ or } Q = e^{\frac{nF}{RT}(\varepsilon^\circ - \varepsilon_{app})}$$

Equation 1.4  $Red$  is the concentration of reduced protein.  $Q$  is the exponential term from Equation 1.3.  $C_t$  is the total protein.

$$Red = \frac{QC_t}{1 + Q} \text{ Where } Ox = C_t - Red$$

Equation 1.5 A chemical process by which a completely oxidized species undergoes two sequential redox events. The events are signified by the arrows.



Equation 1.6  $Red_m$  stands for the concentration of  $m^{\text{th}}$  reduced species. The numerator contains  $m$   $Q$  terms.  $Q$  terms represent the exponential terms for each redox couple. The denominator remains the same for all  $Red_m$  and contains all  $Q$  terms.

$$Red_1 = \frac{C_t Q_1}{(1 + Q_1(1 + Q_2))} \text{ and } Red_2 = \frac{C_t Q_1 Q_2}{(1 + Q_1(1 + Q_2))}$$

$$\text{Where } Q_m = e^{\frac{nF}{RT}(\varepsilon_m^\circ - \varepsilon_{app})} \text{ For } \frac{Red_m}{Red_{m-1}}$$

Equation 1.7  $A_{exp}$  is the experimental absorbance,  $Red$  is the concentration of the reduced species obtained by setting the midpoint potential to a specific value, and  $l$  is the path-length of the cuvette.  $\varepsilon_{calc}$  is the extinction coefficient calculated based on the specific value of the midpoint potential.  $A_{calc}$  is the calculated absorbance.

$$\varepsilon_{calc} = \frac{A_{exp}}{Red(l)} \leftrightarrow A_{calc} = Red l \varepsilon_{calc}$$

### 1.2.2 Electron Paramagnetic Resonance (EPR)

An unpaired electron in an atom or molecule possesses an intrinsic angular momentum termed “spin” of value 1/2. According to Kramers’ theorem the excited  $m_s=1/2$  and ground  $m_s=-1/2$  states of that particle are degenerate in the absence of a magnetic field. An applied magnetic field,  $H$ , separates these

states by an energy  $h\nu$  according to the equation  $g\mu_b H = h\nu$  (Figure 1.3), where  $h$  is the Planck's constant,  $\nu$  is the frequency in GHz of appropriate incident radiation,  $\mu_b$  is the Bohr magneton  $9.27400968(20) \times 10^{-24}$  J/Tesla, and  $g$  is the proportionality Lande factor. For an electron with "spin" only and no orbital angular momentum,  $g_e$  equals 2.0023. The Hamiltonian that describes this separation energy is  $\mathcal{H} = g_e \mu_b H S$ , where  $S$  is the total spin. In a magnetic field the excited state ( $m_{1/2}$ ) will align with, and the ground state ( $m_{-1/2}$ ) opposite the field. If a sample is placed in an oscillating magnetic field perpendicular to the static (swept) field, the absorption can be observed when the energy of separation between two states equals that of oscillating field multiplied by  $h$ . X-band EPR spectroscopy uses microwaves of frequencies around 9.5 GHz, applied perpendicularly to the static magnetic field. The modulation of the swept magnetic field allows for phase sensitive detection, and the derivative of the absorption is recorded.<sup>23</sup>

Transition metal EPR experiments are often conducted at very low temperatures to boost the signal intensity and resolution. Since absorption is observed when a ground state transitions to an excited state, it is necessary to ensure that the ground state population exceeds that of the excited state. The population ratio of the ground and excited states is  $m_{1/2}/m_{-1/2} = e^{-(\Delta E/kT)}$  where  $\Delta E$  is the resonance energy,  $k$  is Boltzmann constant and  $T$  is the temperature in Kelvin. Since the ratio of excited over ground state approaches one as the temperature rises, a more intense signal is observed at the lower temperatures.

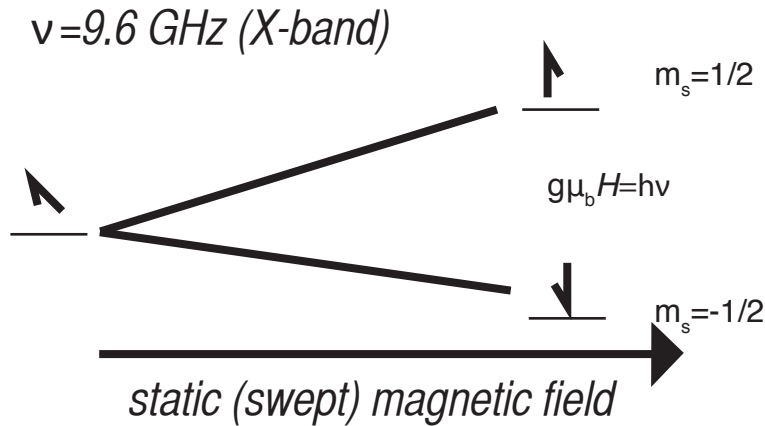


**Figure 1.3** The diagram represents the energy splitting between the excited  $m_s = 1/2$  and ground  $m_s = -1/2$  states as the static magnetic field increases.  $g$  is the Lande factor,  $h$  is Planck's constant,  $\nu$  is the frequency of the isolating magnetic field perpendicular to the static magnetic field,  $\mu_b$  is the Bohr magneton. The initial spin is pictured with a 45-degree tilt to represent that the two levels are degenerate in the absence of magnetic field.

Transition metal EPR experiments are often conducted at very low temperatures to boost the signal intensity and resolution. Since absorption is observed when a ground state transitions to an excited state, it is necessary to ensure that the ground state population exceeds that of the excited state. The population ratio of the ground and excited states is  $m_{1/2}/m_{-1/2} = e^{-(\Delta E/kT)}$  where  $\Delta E$  is the resonance energy,  $k$  is Boltzmann constant and  $T$  is the temperature in Kelvin. Since the ratio of excited over ground state approaches one as the temperature rises, a more intense signal is observed at the lower temperatures.

The EPR spectral resolution of transition metals is affected by their fast relaxation times. According to the Heisenberg's uncertainty principle,  $\Delta E \Delta t \geq \hbar$  ( $\hbar$  is the Planck's constant divided by  $2\pi$ ), when relaxation time is fast, the time uncertainty,  $\Delta t$ , is small, the energy uncertainty,  $\Delta E$ , is large and the spectrum is wide and shallow. The relaxation times are longer at lower temperatures, and as

a consequence the time uncertainty increases while the energy uncertainty decreases. In other words, sharper signals can be detected in the fast relaxing systems at lower temperatures.

EPR spectroscopy has been used to study heme proteins and models for many years<sup>24-30</sup>. For interpreting heme EPR spectra it is useful to view Fe<sup>III</sup> heme complexes as the Fe<sup>III</sup> placed in a distorted octahedral ligand field in which the pyrrole nitrogens are the ligands on the x and y axes, and the axial ligands, which in protein usually come from the amino acid side chains or substrate molecules, are on the z axis. The d-electrons of such complexes are concentrated around the iron nucleus, and within the ligand field approximation do not substantially contribute to the covalency. The electrons' total spin and orbital angular momenta depend on their environment. If we initially ignore distortions from pure octahedral symmetry, then the ligands split the iron 3d orbitals into two energetically distinct sets (Figure 1.4): the  $d_{xy}$ ,  $d_{xz}$  and  $d_{yz}$  real one-electron spatial wave functions form the lower energy  $t_{2g}$  basis set, while  $d_{z^2}$  and  $d_{y^2-x^2}$  form a higher energy  $e_g$  basis set that is separated from  $t_{2g}$  by an energy  $\Delta_o$ , referred to as the ligand-field splitting. We can now distinguish two possible electronic configurations for the Fe<sup>III</sup>  $d^5$  system (Figure 1.4). If the  $\Delta_o$  split is higher than the electron pairing energy, then all five d electrons are localized on the  $t_{2g}$  orbitals, and the total spin is  $S=1/2$  (low spin). If the pairing energy is higher than the ligand-field splitting then electrons are distributed amongst all five d orbitals and the total spin is  $S=5/2$  (high spin).

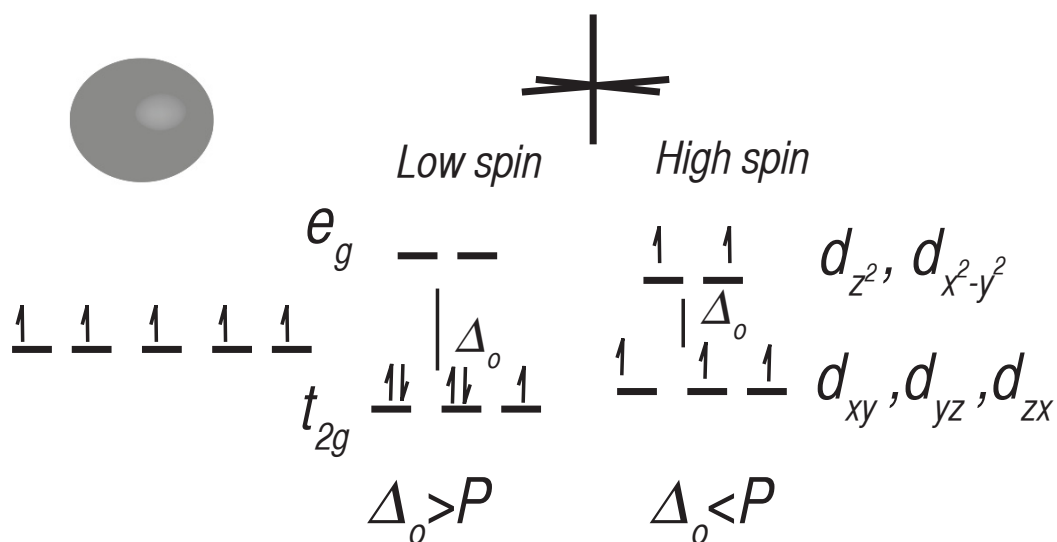


**Figure 1.4** The diagram represents the octahedral ligand-field splitting effect on the Fe(III) 3d orbitals. The strength of the ligand field in comparison with the strength of the pairing energy will determine the total spin configuration. This difference is detectable by EPR spectroscopy.

Both high-spin and low-spin hemes undergo distortions from octahedral symmetry<sup>24-30</sup>. Cylindrical or near-cylindrical axial ligands, such as cyanide, impose a tetragonal distortion in which the  $d_{xz}$  and  $d_{yz}$  orbitals are elevated in energy relative to  $t_{2g}$ , while the  $d_{xy}$  is lowered. Similarly  $d_{z^2}$  in the  $e_g$  set is stabilized, while  $d_{x^2-y^2}$  is destabilized (Figure 1.5). Further rhombic distortions can remove the degeneracy of  $d_{xz}$  and  $d_{yz}$  (Figure 1.5). For example, when two planar ligands such as histidines coordinate in plane with each other (Figure 1.6 A), they both interact with the metal along the z axis and *either* the x or y axis. The induced asymmetry breaks the degeneracy of  $d_{xz}$  and  $d_{yz}$  orbitals and produces the rhombic distortion. On the other hand if the histidines are perpendicular to each other (Figure 1.6 B), they interact with the metal along z, and x and y axes,

so that in practice the  $d_{xz}$  and  $d_{yz}$  orbitals remain practically degenerate, and spectra characteristic of axial symmetry are obtained (see below).

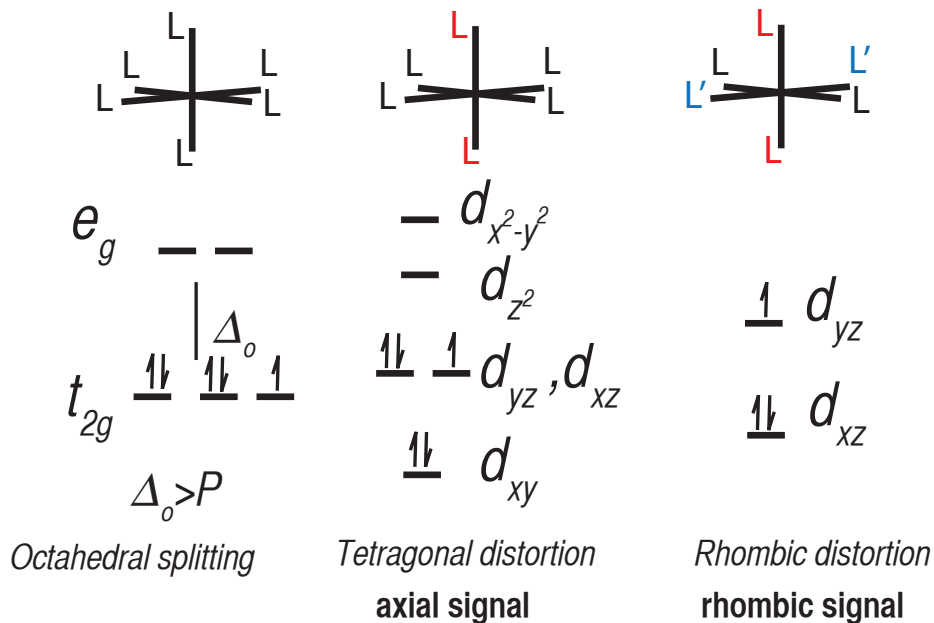


**Figure 1.5** The effects of strong octahedral ligand-field splitting followed by tetragonal and rhombic distortions on the energies of the d spatial orbitals. The bold labels are the terms for the EPR signals characteristic of these distortions. These terms are used throughout this thesis.

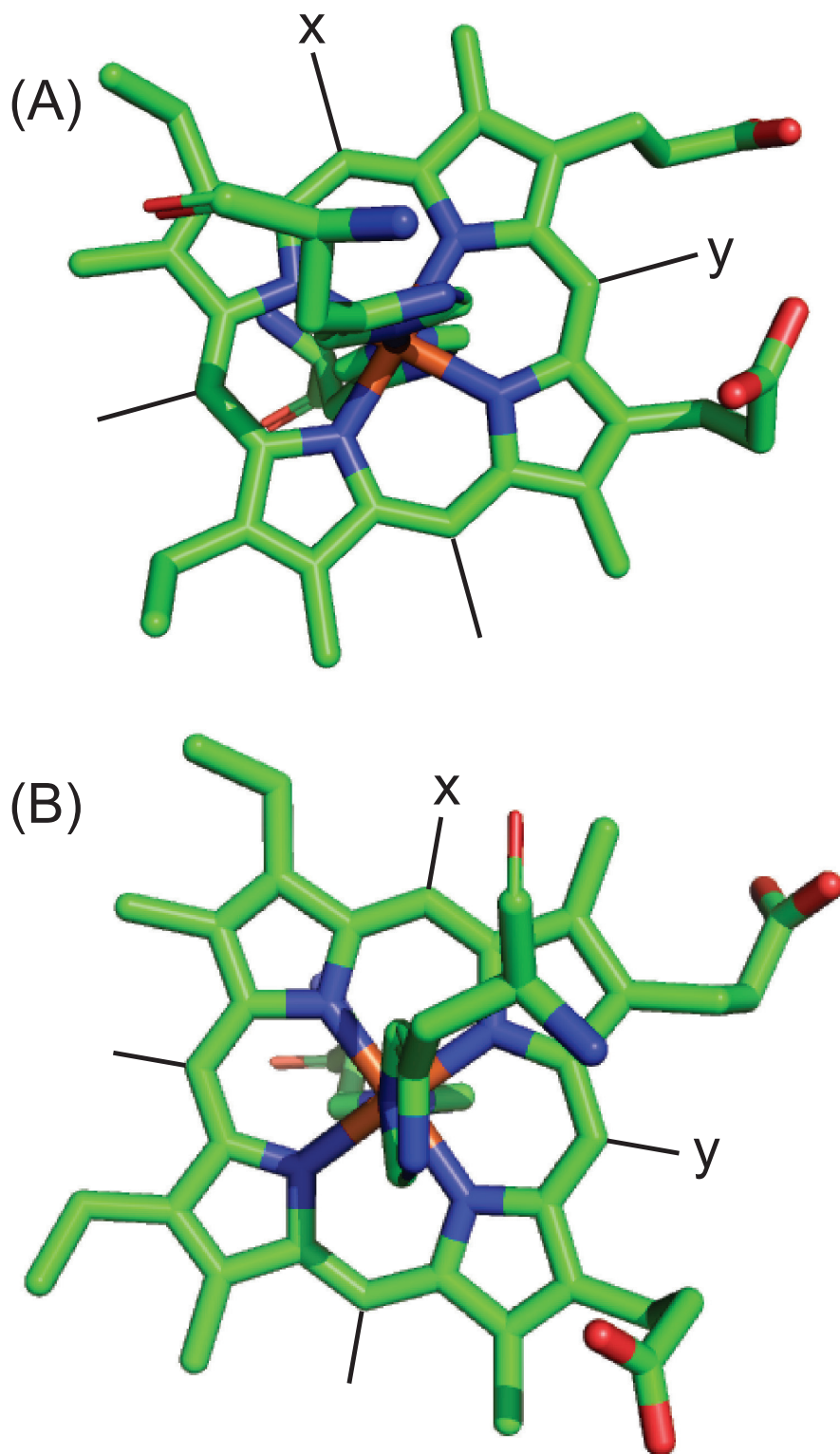


**Figure 1.6** (A) Two axial histidines aligned in plane with each other and only with the y axis, lower the symmetry of the complex. (B) Histidines aligned perpendicularly to each other and equally with the y and x axes, preserve the symmetry.

For EPR experiments with iron, low temperatures are required in order to maintain a sufficient population difference between ground and excited states, and more importantly to lower the relaxation time. As a consequence the samples are always frozen. Instead of the average  $g$  values, directional (anisotropic)  $g$  values can be measured. The new Hamiltonian for the resonance energy will be  $\mathcal{H} = (g_e + \Delta g_{(x,y \text{ or } z)}) \mu_B H S$ , where  $\Delta g_{(x,y \text{ or } z)}$  is the change of magnetic moment along the  $x$ ,  $y$  or  $z$  axis with respect to the value for the free electron. Griffith was perhaps the first to describe the relationship between the  $g$  values of a low-spin heme and the energies of distortions<sup>24</sup>. Taylor refined Griffith's method so that the crystal field parameters could be easily calculated using the following relationships, which provide the energy separations between  $d_{zx}$  and  $d_{yz}$  (A), and between  $d_{xy}$  and  $d_{yz}$  (B), in units of spin orbit coupling ( $\text{cm}^{-1}$ ):  $A = g_x/(g_z + g_y) + g_y/(g_z - g_x)$  and  $B = g_x/(g_z + g_y) + g_z/(g_y - g_x)$ <sup>26</sup>. More importantly in ref<sup>26</sup> Taylor also provides convenient calculations for determining the location of unpaired spin density and the degree of covalency that 3d electrons may experience. Harris-Loew did an in-depth computational analysis on how the  $g$  values vary with rhombicity, and compared them with several available heme systems<sup>29</sup>. Subsequently De Vries made an observation that the limit of the sum of squares of  $g$  values would equal sixteen at most if  $g_0 = 2$ <sup>30</sup>; while Walker correlated the rhombic and tetragonal distortions with the positions of axial ligand in bis-histidine ligated hemes<sup>27</sup>. Walker also used EPR and Mossbauer to demonstrate that the rhombic distortion increases as the angle between two

histidines nears zero. The identities of bis-histidine ligated hemes in this thesis were assigned based on these studies (Section 1.3 and Chapter 2).

In high-spin hemes the departure from octahedral symmetry is measured in terms of D and E parameters<sup>23</sup>. Because of the spin-spin interactions and electron-electron repulsions imposed on 3d electrons by the ligand field, the ground state sextet splits into three Kramer's doublets  $\pm 1/2$ ,  $\pm 3/2$  and  $\pm 5/2$ . These doublets are separated from each other by multiples of the parameter D:  $\pm 1/2$  and  $\pm 3/2$  are separated by 2D, and  $\pm 3/2$  and  $\pm 5/2$  by 4D<sup>23</sup>. These separations are present in the absence of magnetic field, which is why they are termed zero field splittings. The additional E parameter arises when a rhombic distortion occurs, and in essence is a combination of the D tensor diagonal elements:  $D=3D_z^2/2$ ,  $E=(D_x^2-D_y^2)/2$  and  $D_x^2+D_y^2+D_z^2=0$ . The complete Hamiltonian for the high-spin heme energies is  $\mathcal{H} = D(S_z^2-2)+E(S_x^2-S_y^2)+g\mu_bHS$ . In the absence of rhombic distortion, and with  $D \gg hv$ , only the ground state  $M_s = \pm 1/2$  doublet is appreciably populated, and characteristic resonances at  $g_{eff} = 6$  and 2 are observed.

Importantly, as will be discussed further in Section 1.3 and Chapter 2, all high-spin hemes observed in this work were coupled to at least one other heme, so  $g_{eff}=6$  was never observed. Coupling of two paramagnetic samples involves dipolar, exchange and zero-field interactions. The Hamiltonian for such coupling is  $\mathcal{H} = JS_1S_2 + S_1D'S_2 + d'S_1S_2 + \mu_bBg_1S_1 + \mu_bBg_2S_2$ , where J is the exchange tensor, D' is the traceless symmetric tensor similar to D, and d' is the antisymmetric

tensor of dipolar interactions<sup>31</sup>. The coupling signals are difficult to simulate because they depend strongly on intrinsic g tensors of two interacting magnetic centers. Hence, the g tensors can change with slight rotations of axial ligands in bis-histidine ligated hemes<sup>28</sup>, and with minor conformational changes of a protein around a high-spin heme<sup>25</sup>. A striking example of how minor structural changes can profoundly affect the EPR spectra of coupled hemes will be described in Chapter 3.

### **1.3 Electronic and magnetic properties of hemes in CcNiR and related proteins**

Chapter 2 describes UV-vis and electron paramagnetic resonance (EPR) based spectropotentiometry experiments used to determine the midpoint potentials of the redox centers in CcNiR from *S. oneidensis*. The UV-vis experiments provided quantitative midpoint redox potentials, and EPR provided the information necessary to assign these potentials to specific hemes. Analogous studies of CcNiRs from *Escherichia coli*<sup>7</sup> and *Desulfovibrio desulfuricans*<sup>32-34</sup> also involved potentiometric titrations in conjunction with EPR spectroscopy. In addition, UV-vis and MCD potentiometric titrations on *E.coli* CcNiR were done in a separate study<sup>35,36</sup>. Finally, studies of *D. desulfuricans* CcNiR included Mössbauer potentiometric titrations<sup>32-34</sup>. This section reviews the results of these earlier studies.

The utility of EPR in assigning specific hemes in a given enzyme comes from the technique's sensitivity to the hemes' structural microenvironment. To date, crystal structures for homodimeric CcNiR variants from six bacterial species have been obtained. The source organisms belong to three different branches of the bacterial phylogenetic tree ( $\epsilon$ -proteobacteria, *Sulfurospirillum deleyianum* and *Wollinella succinogenes*;  $\delta$ -proteobacteria, *Desulfovibrio vulgaris* and *D. desulfuricans*; and  $\gamma$ -proteobacteria, *E. coli* and *S. oneidensis*)<sup>4-10,37</sup>. The structures are all quite similar, and in particular the heme arrangements are highly conserved. As an example, Figure 1.1B shows the arrangement of the hemes within one subunit of the *S. oneidensis* CcNiR dimer, including the axial ligands, the orientations of which have a strong influence on EPR and other types of spectra.

The magnetic properties of low-spin hemes have been studied extensively, both in proteins and synthetic models<sup>24-26,38-40</sup>. The midpoint potentials and the spectroscopic signals of bis-histidine ligated hemes are affected by the orientation of the said histidines with respect to each other, and to the pyrrole nitrogens of the porphyrin (Section 1.2.2)<sup>28,38,40</sup>. In enzymes like CcNiR that have hemes in close proximity to each other magnetic coupling can arise between the hemes. For the purposes of this discussion it will thus be convenient to discuss the CcNiR hemes in terms of three groupings; using the numbering of Figure. 1.1B, these are hemes 2 and 5, which exhibit minimal or no coupling, the active site heme 1, and hemes 3 and 4. These last three hemes

typically exhibit coupling in CcNiRs, and heme 1 is additionally unique in being high-spin.

### 1.3.1 Peripheral hemes 2 and 5

In CcNiRs from various species heme 2 is the most magnetically isolated, and the EPR signal exhibits no evidence of spin-spin interaction. The axial imidazole rings are essentially parallel to each other, and impose a moderately rhombic symmetry, so the EPR signals' turning points exhibit three distinct Landé  $g$ -factors (usually referred to as " $g$ -values" in the literature)<sup>38</sup>, as seen in the example of heme 2, for which  $g_z > g_y > g_x$  (Table 1.1). The midpoint potentials for hemes 2 can be determined by EPR alone without any ambiguities, due to its distinct signal.

**Table 1.1** *E. coli*  $\tau$  values were obtained from Bamford et al.<sup>7</sup>. The angles between the imidazoles, and imidazoles and porphyrin, were measured using the “get dihedral” function in PyMol and the crystal structure published in Clarke *et al.*<sup>41</sup>. *D. desulfuricans*  $\tau$  values were obtained from a combination of studies<sup>32-34</sup>. The angles were measured by the same method as with *E. coli* using the structure published in by Cunha<sup>8</sup>. See Figure 1.7 for a more thorough description of the angle measurements.

Organism	Heme	$\tau_{obs}$ values	imidazole angles	imidazole porphyrin angle
<i>E. coli</i>	Heme1	not observed	N/A	N/A
	Heme2	1.5 2.3 2.92	16.488	-41.86 and -58.60
	Heme3	not observed	53.34	59.646 and 6.138
	Heme4	3.2	67.513	76.93 and 142.661
	Heme5	3.2	62.05	115.737 and 51.99
<i>D. desulfuricans</i>	Heme1	not observed	~6	N/A
	Heme2	1.5 2.18 2.96	22.97	-42.125 and -64.905
	Heme3	3.2	57.635	54.692 and 0.593
	Heme4	3.6	90.00	71.849 and 38.750
	Heme5	3.5	64.76	85.975 and 43.442

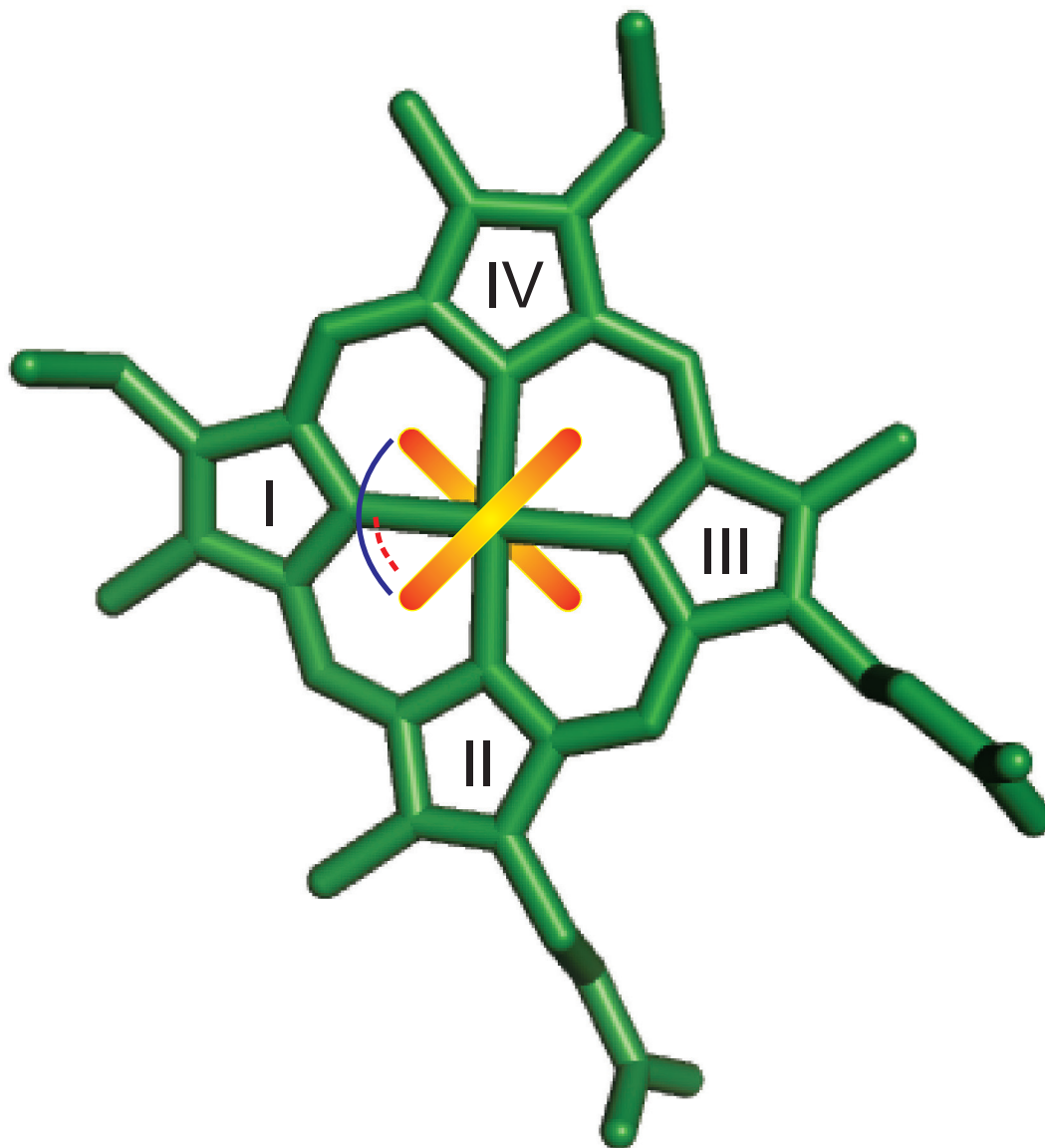


**Figure 1.7** Heme-heme and heme pyrrole nitrogen dihedral angles for Table 1.1 were measured as illustrated here. The pyrrole ring I was selected to serve as the reference in both cases. The central atom was used as the second atom for dihedral angle calculations all measurements.

On the same face of the enzyme as heme 2, though distant from it (Figure 1.1A), heme 5 has two histidines with the imidazole rings almost perpendicular to each other. EPR signals from these hemes are sometimes known, incorrectly, as highly anisotropic low-spin signals<sup>42</sup> or, more correctly, as highly axial low-spin signals (HALS)<sup>43</sup>. These signals are difficult to resolve, and are characterized by

$4 > g(\text{max}) > 3$  and  $g(\text{min}) \ll 2$ <sup>38</sup>. The confusion behind the terminology is due to the anisotropic appearance of the EPR signal's "folded" lineshape. The signal is in fact due to an almost axial symmetry at the Fe(III) center, and a reduction of the degeneracy of the  $d_{xz}$  and  $d_{yz}$  orbitals to the point where the unpaired electron can be considered to be shared between them; in the axial limit, the orbital energies converge and  $g_z$  approaches 4 (See Section 1.2.2).

### 1.3.2 Active site heme 1

Two prominent features of CcNiR X-band EPR are a resonance with a turning point at  $g = 3.5 - 3.9$ , along with absorption extending into low magnetic field with  $g' > 10$  (see, for example, Figure. 2.2, Chapter 2).<sup>†</sup> These features have been attributed to a weak magnetic coupling between the active site heme 1 with spin 5/2, and heme 3 with spin 1/2<sup>7,45</sup>. Where the exchange coupling,  $-2J$ , dominates, either (or both) resonances due to  $S = 2$  and  $S = 3$  would be expected with  $g' \approx 8$  and 12, respectively, and absorption possibly extending into zero-field<sup>46</sup>. A resonance at 3.5 - 3.9, would be consistent with a situation where  $-2J$  and  $D$  the zero-field parameter for the high-spin ferriheme are comparable<sup>47</sup>. Strains in either  $J$  and/or  $D$  could yield a distribution of  $D/J$  in the sample such that the conditions are satisfied for both signals

---

<sup>†</sup> The quantity  $g'$ , or  $g'$ -value, is used to denote the *effective*  $g$ -value of a resonance in the EPR spectrum that is not necessarily determined by the Landé  $g$ -factor, whereas  $g$ , or  $g$ -value, implies the Landé  $g$ -factor. In the case of high-spin systems (with  $S > 1/2$ ), the  $g'$ -value is often largely a function of the zero-field splitting constant,  $D$  (see Section 1.2.2). For  $S = 5/2$  and  $g = 2$ , the usual case for high-spin Fe(III),  $g' \leq 10$ ; if  $g' > 10$ , then either  $S > 5/2$ , if non-integer, or else  $S$  has an integer value ( see ref. 44 Hagen, W. R. EPR spectroscopy of iron-sulfur proteins. *Adv. Inorg. Chem.* **38**, 165-222 (1992).).

All available crystal structures of these CcNiR enzymes show the same arrangement of hemes 1, 3 & 4 in which the three heme planes are essentially parallel, hemes 1 and 4 are adjacent and in-plane with one another, and heme 3 is stacked beneath and centered midway between hemes 1 and 4 (Figure. 1.1 B). An analogous architecture was observed in HAO, which exhibits a similar EPR signal<sup>48</sup>. After the high-spin heme in that protein is reduced during potentiometric titrations, the low-spin heme to which it is coupled becomes independently observable by EPR<sup>49,50</sup>. Another multi-heme protein, cytochrome *c*<sub>554</sub> (C<sub>554</sub>), has two coupled heme systems: the first exhibits 1/2-1/2 coupling, and the second 5/2-1/2 coupling<sup>51,52</sup>. C<sub>554</sub> is the HAO's physiological electron acceptor. Its heme 2 is five co-ordinate with one axial histidine, has S=5/2 spin state, and is magnetically coupled to heme 4. In the oxidized state the five coordinate site is shielded from solvent. But once C<sub>554</sub> is fully reduced, it was shown to bind and reduce NO<sup>52</sup>. Five coordinate hemes have a diverse functionality, and a range of factors can influence their midpoint potentials and coupling state.

EPR potentiometric titrations of *E. coli* CcNiR did not elicit an isolated  $S = 1/2$  or  $S = 5/2$  signal assignable to the five coordinate heme 1 of the active site<sup>7</sup>. CcNiR complexed with NrfH, isolated from *D. desulfuricans*, did exhibit a resolved signal with  $g'(max) = 6$  upon application of potentials ranging from 7 to -120mV versus standard hydrogen electrode (SHE), although only with intensity corresponding to a small fraction of the spins<sup>32</sup>. The appearance of the  $g' = 6$  signal coincided with the appearance of another signal with  $g(max) = 3.2$ . It

seems likely, then, that the coupled signal is due to the interaction between the  $g' = 6$  and  $g = 3.2$  species.

Mössbauer spectroscopy allows examination of the iron species' oxidation states independent of spin-spin interactions, and a spectropotentiometric Mössbauer titration suggested that the active site heme 1 of the *D. desulfuricans* CcNiR has a midpoint potential of  $-80\text{mV}$  versus SHE, lower than the highest values exhibited by hemes 5 and 2, respectively, and higher than hemes 3 and 4<sup>33,34</sup>. Since the active site coupled signal at  $g=3.9$  disappears during the titrations of heme 5 and then the high-spin signal appears transiently at  $g\sim 6$  during the titration of heme 2, it is reasonable to suspect that the protein undergoes structural changes that influence the spin-Hamiltonian parameters and, therefore, the EPR signals. Changes in the EPR signals of high-spin ferrihemes as a result of protein conformational changes have been reported<sup>25</sup>. Changes which would reduce the exchange coupling between two hemes may include rotation of one or both  $g$ -tensors, or a change in the symmetry of the  $S = 1/2$  Fe(III) ion, and thus of the electron density distribution between the  $d_{xz}$  and  $d_{yz}$  orbitals, due to a change in the inter-imidazole angle of the two axial histidines.

### 1.3.3 Inner core hemes 3 and 4

While there are no reports on coupling between hemes 3 and 4 in CcNiR, similarly arranged hemes that *are* coupled are observed in C<sub>554</sub> and HAO. Heme 3 is positioned at equal angles and distances from hemes 1 and 4. If heme 3 couples to heme 1, it is plausible that the coupling also extends to heme 4.

Hemes 3 and 4 are reported to have the lowest potentials in *D. desulfuricans* CcNiR<sup>34</sup>, where EPR and Mössbauer spectroscopies were used for the assignment. EPR potentiometric titrations of *E. coli* CcNiR revealed a  $g = 3.2$  signal that is not very well resolved as the applied potential decreased. The authors attributed this signal to the putative HALS signals of hemes 4 and/or 5<sup>7</sup>.

## 1.4 Summary

As shown above in this section, the EPR and other types of spectra for multi-heme proteins with very similar heme arrangements, such as CcNiRs from *Desulfovibrio sp.* and *E. coli*, and HAO or C<sub>554</sub> from ammonia oxidizing bacteria, are similar to each other in many ways, but can differ significantly in others. The results presented in Chapters 2 and 3 extend the spectroscopic analyses to the *S. oneidensis* CcNiR. These results show that subtle variations in the midpoint potentials of the hemes from different homologues can change the spectroscopic behavior substantially, but without significantly affecting enzyme function.

## 1.5 References

- 1 Simon, J. Enzymology and bioenergetics of respiratory nitrite ammonification. *FEMS Microbiol. Rev.* **26**, 285-309 (2002).
- 2 Pooch, S., Leach, E., Moir, J., Cole, J. & Richardson, D. Respiratory Detoxification of Nitric Oxide by the Cytochrome *c* Nitrite Reductase of *Escherichia coli*. *J. Biol. Chem.* **277**, 23664-23669 (2002).
- 3 Einsle, O., Messerschmidt, A., Huber, R., Kroneck, P. M. H. & Neese, F. Mechanism of the six-electron reduction of nitrite to ammonia by cytochrome *c* nitrite reductase. *J. Am. Chem. Soc.* **124**, 11737-11745, doi:10.1021/Ja0206487 (2002).
- 4 Einsle, O. *et al.* Structure of cytochrome *c* nitrite reductase. *Nature* **400**, 476-480 (1999).
- 5 Einsle, O. *et al.* Cytochrome *c* nitrite reductase from *Wolinella succinogenes* - Structure at 1.6 angstrom resolution, inhibitor binding, and heme-packing motifs. *J. Biol. Chem.* **275**, 39608-39616 (2000).
- 6 Pereira, I., LeGall, J., Xavier, A. & Teixeira, M. Characterization of a heme *c* nitrite reductase from a non-ammonifying microorganism, *Desulfovibrio vulgaris* Hildenborough. *Biochim. Biophys. Acta* **1481**, 119-130 (2000).
- 7 Bamford, V. A. *et al.* Structure and spectroscopy of the periplasmic cytochrome *c* nitrite reductase from *Escherichia coli*. *Biochemistry* **41**, 2921-2931, doi:10.1021/Bi015765d (2002).
- 8 Cunha, C. A. *et al.* Cytochrome *c* nitrite reductase from *Desulfovibrio desulfuricans* ATCC 27774 - The relevance of the two calcium sites in the structure of the catalytic subunit (NrfA). *J. Biol. Chem.* **278**, 17455-17465, doi:10.1074/jbc.M211777200 (2003).
- 9 Rodrigues, M., Oliveira, T., Pereira, I. & Archer, M. X-ray structure of the membrane-bound cytochrome *c* quinol dehydrogenase NrfH reveals novel haem coordination. *EMBO Journal* **25**, 5951-5960 (2006).
- 10 Youngblut, M. *et al.* Laue crystal structure of *Shewanella oneidensis* cytochrome *c* nitrite reductase from a high-yield expression system. *J. Biol. Inorg. Chem.* **17**, 647-662 (2012).
- 11 Ehrlich, H. L. *Geomicrobiology*. 4th edn, (Marcel Dekker, Inc, 2002).
- 12 Fenchel, T., King, G. M. & Blackburn, T. H. *Bacterial Biogeochemistry*. 2nd edn, (Academic Press, 1998).
- 13 Kern, M., Volz, J. & Simon, J. The oxidative and nitrosative stress defense network of *Wollinella succinogenes*: cytochrome *c* nitrite reductase

- mediates the stress response to nitrite, nitric oxide, hydroxylamine and hydrogen peroxide. *Environ. Microbiol.* **13**, 2478-2494 (2011).
- 14 Tikhonova, T. *et al.* Comparative structural and functional analysis of two octaheme nitrite reductases from closely related *Thioalkalovibrio* species. *FEBS J.* **279**, 4052-4061 (2012).
  - 15 Mowat, C. G. & Chapman, S. J. Multi-heme cytochromes - new structures, new chemistry. *J. Chem. Soc. Dalton Trans.* **21**, 3381-3389 (2005).
  - 16 Bewley, K. D., Ellis, K. E., Firer-Sherwood, M. A. & Elliott, S. J. Multi-heme proteins: nature's electronic multi-purpose tool. *Biochim. Biophys Acta* **1827**, 938-948 (2013).
  - 17 Youngblut, M. *et al.* *Shewanella oneidensis* cytochrome *c* nitrite reductase (ccNiR) does not disproportionate hydroxylamine to ammonia and nitrite, despite a strongly favorable driving force. *Biochemistry* **53**, 2136-2144 (2014).
  - 18 Kostera, J., McGarry, J. M. & Pacheco, A. A. Enzymatic Interconversion of Ammonia and Nitrite: the Right Tool for the Job. *Biochemistry* **49**, 8546-8553 (2010).
  - 19 Kostera, J., Youngblut, M. D., Slosarczyk, J. M. & Pacheco, A. A. Kinetic and product distribution analysis of NO reductase activity in *Nitrosomonas europaea* hydroxylamine oxidoreductase. *J. Biol. Inorg. Chem.* **13**, 1073-1083, doi:10.1007/s00775-008-0393-4 (2008).
  - 20 Gouterman, M. in *The Porphyrins V3* (ed D. Dolphin) Ch. 1, 1-166 (Academic Press, Inc., 1978).
  - 21 Heineman, W. R., Norris, B. J. & Goelz, J. F. Measurement of enzyme  $E^0$  values by optically transparent thin layer electrochemical cells. *Anal. Chem.* **47**, 79-84 (1975).
  - 22 Pilkington, M. B. G., Coles, B. A. & Compton, R. G. Construction of an optically transparent thin layer electrode cell for use with oxygen-sensitive species in aqueous and non-aqueous solvents. *Anal. Chem.* **61**, 1787-1789 (1989).
  - 23 Rieger, P. H. *Electron spin resonance: analysis and interpretation*. (Royal Society of Chemistry, 2007).
  - 24 Griffith, J. S. Theory of electron resonance in ferrihaemoglobin azide. *Nature* **180**, 30-31 (1957).
  - 25 Peisach, J., Blumberg, W. E., Ogawa, S., Rachmilewitz, E. A. & Oltzik, R. The effects of protein conformation on the heme symmetry in high spin ferric heme proteins as studied by electron paramagnetic resonance. *J. Biol. Chem.* **246**, 3342-3355 (1971).

- 26 Taylor, C. P. The EPR of low-spin heme complexes. Relation of the t<sub>2g</sub> hole model to the directional properties of the g tensor, and a new method for calculating the ligand field parameters. *Biochim. Biophys. Acta* **491**, 137-138 (1977).
- 27 Walker, F. A., Boi Hanh, H., Scheidt, W. R. & Osvath, S. R. Models of the cytochromes b. Effect of axial ligand plane orientation on the EPR and Moessbauer spectra of low-spin ferrihemes. *Journal of the American Chemical Society* **108**, 5288-5297, doi:10.1021/ja00277a038 (1986).
- 28 Shokhirev, N. V. & Walker, F. A. Co- and counterrotation of magnetic axes and axial ligands in low-spin ferriheme systems. *J. Am. Chem. Soc.* **120**, 981-990 (1998).
- 29 Harris-Loew, G. M. An analysis of the electron spin resonance of low spin ferric heme compounds. *Biophysical journal* **10**, 196-212 (1970).
- 30 De Vries, S. & Albracht, S. P. J. Intensity of highly anisotropic low-spin heme EPR signals. *Biochimica et Biophysica Acta (BBA) - Bioenergetics* **546**, 334-340, doi:10.1016/0005-2728(79)90050-1 (1979).
- 31 Hendrich, M. P., Petasis, D., Arciero, D. M. & Hooper, A. B. Correlations of structure and electronic properties from EPR spectroscopy of hydroxylamine oxidoreductase. *J. Am. Chem. Soc.* **123**, 2997-3005 (2001).
- 32 Costa, C. *et al.* Hexaheme nitrite reductase from *Desulfovibrio desulfuricans*. *J. Biol. Chem.* **265**, 14382-14387 (1990).
- 33 Costa, C., Moura, J. J. G., Moura, I., Wang, Y. & Huynh, B. H. Redox properties of cytochrome c nitrite reductase from *Desulfovibrio desulfuricans* ATCC27774. *J. Biol. Chem.* **271**, 23191-23196 (1996).
- 34 Almeida, M. G. *et al.* The isolation and characterization of cytochrome c nitrite reductase subunits (NrfA and NrfH) from *Desulfovibrio desulfuricans* ATCC27774: Re-evaluation of the spectroscopic data and redox properties. *Eur. J. Biochem.* **270**, 3904-3915 (2003).
- 35 Eaves, D. J. *et al.* Involvement of products of the *nrfEFG* genes in the covalent attachment of haem c to a novel cysteine-lysine motif in the cytochrome *c*<sub>552</sub> nitrite reductase from *Escherichia coli*. *Mol. Microbiol.* **28**, 205-216 (1998).
- 36 Marritt, S. J. *et al.* Spectroelectrochemical characterization of a pentaheme cytochrome in solution and as electrocatalytically active films on nanocrystalline metal-oxide electrodes. *J. Am. Chem. Soc.* **130**, 8588-8589 (2008).
- 37 Rodrigues, M. L. *et al.* Crystallization and preliminary structure determination of the membrane-bound complex cytochrome c nitrite

- reductase from *Desulfovibrio vulgaris* Hildenborough. *Acta Cryst. F* **62**, 565-568 (2006).
- 38 Walker, F. A., Huynh, B. H., Scheidt, W. R. & Osvath, S. R. Models of the cytochromes *b*. Effect of axial ligand plane orientation on the EPR and Mossbauer spectra of low-spin ferrihemes. *J. Am. Chem. Soc.* **108**, 5288-5297 (1986).
- 39 Soltis, S. M. & Strouse, C. E. Electronic structure of low-spin ferric porphyrins: single-crystal EPR evidence for pseudo-Jahn-Teller distortion in (tetraphenylporphinato)iron(III) bis(imidazole) cations. *J. Am. Chem. Soc.* **110**, 2824-2829 (1988).
- 40 Bertini, I., Luchinat, C., Parigi, G. & Walker, F. A. Heme methyl <sup>1</sup>H chemical shifts as structural parameters in some low-spin ferriheme proteins. *J. Biol. Inorg. Chem.* **4**, 515-519 (1999).
- 41 Clarke, T. A. *et al.* Role of a conserved glutamine residue in tuning the catalytic activity of *Escherichia coli* Cytochrome *c* nitrite reductase. *Biochemistry* **47**, 3789-3799 (2008).
- 42 Gadsby, P. M. A. & Thomson, A. J. Low-temperature EPR and near-infrared MCD studies of highly anisotropic low-spin ferrihaem complexes. *FEBS* **197**, 253-257 (1986).
- 43 Spinner, F. *et al.* The haem *b*<sub>558</sub> component of the cytochrome *bd* quinol oxidase complex from *Escherichia coli* has histidine-methionine axial ligation. *Biochem. J.* **308**, 641-644 (1995).
- 44 Hagen, W. R. EPR spectroscopy of iron-sulfur proteins. *Adv. Inorg. Chem.* **38**, 165-222 (1992).
- 45 Oganessian, V. S. *et al.* Nature of the coupling between the high-spin (Fe(III) heme and Cu<sub>B</sub>(II) in the active site of terminal oxidases: dual-mode EPR spectra of fluoride cytochrome *bo*<sub>3</sub>. *J. Am. Chem. Soc.* **120**, 4232-4233 (1998).
- 46 Hendrich, M. P. & Debrunner, P. G. Integer-spin electron paramagnetic resonance of iron porphyrins. *Biophys J.* **56**, 489-506 (1989).
- 47 Rutter, R. *et al.* Chloroperoxidase compound I: electron paramagnetic resonance and mossbauer studies. *Biochemistry* **23**, 6809-6816 (1984).
- 48 Igarashi, N., Moriyama, H., Fujiwara, T., Fukumori, Y. & Tanaka, N. The 2.8 angstrom structure of hydroxylamine oxidoreductase from a nitrifying chemoautotrophic bacterium, *Nitrosomonas europaea*. *Nat. Struct. Biol.* **4**, 276-284 (1997).
- 49 Hendrich, M. P. *et al.* The Active-Site of Hydroxylamine Oxidoreductase from *Nitrosomonas* - Evidence for a New Metal Cluster in Enzymes. *J. Am. Chem. Soc.* **116**, 11961-11968 (1994).

- 50 Arciero, D. M., Golombek, A., Hendrich, M. P. & Hooper, A. B. Correlation of optical and EPR signals with the P460 heme of hydroxylamine oxidoreductase from *Nitrosomonas europaea*. *Biochemistry* **37**, 523-529 (1998).
- 51 Upadhyay, A. K., Petasis, D. T., Arciero, D. M., Hooper, A. B. & Hendrich, M. P. Spectroscopic characterization and assignment of reduction potentials in the tetraheme cytochrome c(554) from *Nitrosomonas europaea*. *J. Am. Chem. Soc.* **125**, 1738-1747, doi:Doi 10.1021/Ja020922x (2003).
- 52 Upadhyay, A. K., Hooper, A. B. & Hendrich, M. P. NO reductase activity of the tetraheme cytochrome c(554) of *Nitrosomonas europaea*. *J. Am. Chem. Soc.* **128**, 4330-4337, doi:Doi 10.1021/Ja055183+ (2006).

## **2 Correlations between the electronic properties of *S. oneidensis* CcNiR and its structure: effects of heme oxidation state and active site ligation, and implications for the CcNiR reaction mechanism**

### **2.1 Background**

Many aspects of the heme arrangement within CcNiR are replicated in other proteins<sup>1,2</sup>, and how a common structural motif is optimized for specialized roles is a subject of much investigation. For example, as mentioned in Chapter 1, comparative mechanistic studies of CcNiR and hydroxylamine oxidoreductase (HAO) have been carried out in order to understand how the two enzymes have been evolutionarily optimized to catalyze similar reactions in opposite directions<sup>3-6</sup>. Ultimately, meaningful interpretation of mechanistic data for CcNiR and HAO requires that the redox properties of the enzymes under reaction conditions be thoroughly understood. This chapter presents UV/Vis and EPR spectropotentiometric studies of CcNiR from *Shewanella oneidensis* in the presence of both weak-field and strong-field ligands, including the physiological substrate nitrite. It also explores the interaction of oxidized CcNiR with nitrite and cyanide using EPR spectroscopy. The major objective of these studies was to

obtain midpoint potentials for the CcNiR hemes in the presence of each given ligand. Addition of a ligand to a five coordinate active site is expected to shift its midpoint potential depending on the nature of ligand. This change is instrumental for the assignment of midpoint potentials in a multiheme protein such as CcNiR. EPR spectroscopy was also used to confirm that the concentrations of ligand used in potentiometric experiments were sufficient to fully occupy CcNiR's active sites. In addition to fulfilling this objective, the studies also provided several insights with possible mechanistic importance.

While the midpoint potential of the five-coordinate active site in CcNiR can be altered by exogenous ligand addition, to produce a similar effect for six-coordinate hemes a site directed mutagenesis is required. Here we report the effects of replacement of heme 5's axial ligand histidine 268 (H268) with methionine. This mutant helped to assign the heme 5 midpoint potential.

## **2.2 Materials and Methods**

### 2.2.1 General materials

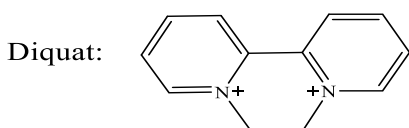
Potassium cyanide, sodium nitrite, ethylenediaminetetraacetic acid disodium salt (EDTA), anthroquinone-2-sulfonic acid sodium salt monohydrate, methyl viologen hydrate and safranine-O were purchased from Acros Organics. Anthroquinone-1,5-disulfonic acid disodium salt hydrate, hexaammineruthenium(III) chloride, potassium indigo trisulfonate, potassium indigo tetrasulfonate and indigo carmine were purchased from Sigma-Aldrich. Sodium chloride and 2-[4-(2-hydroxyethyl)-piperazin-1-yl]ethanesulfonic acid

(HEPES) sodium salt were from Fisher Scientific. The mediator Diquat (6,7-dihydrodipyrido[1,2-a:2',1'-c]pyrazinediium dibromide, Table 2.1) was synthesized using the method described by Homer and Tomlinson <sup>7</sup>.

**Table 2.1 Mediators used for spectropotentiometry**

Mediator	$\epsilon$ vs SHE	Used for	Conc. $\mu$ M
Phenazine methosulfate	0.08	UV/Vis	25
Gallocyanin	-0.020	UV/Vis EPR	25
Hexaammineruthenium(III) chloride	-0.020	UV/Vis	100
Indigo tetrasulfonate	-0.030	UV/Vis, EPR	25
Indigo trisulfonate	-0.080	UV/Vis, EPR	25
Indigo carmine	-0.125	UV/Vis, EPR	25
Anthraquinone 1,5-disulfonic acid	-0.175	UV/Vis, EPR	25
Anthraquinone 2-sulfonic acid	-0.255	UV/Vis, EPR	25
Safranin O	-0.289	UV/Vis, EPR	25
Diquat	-0.390	UV/Vis, EPR	25
Methyl viologen	-0.449	UV/Vis, EPR	25

a



### 2.2.2 Protein purification and handling

Wild type *S. oneidensis* CcNiR (CcNiRwt) was purified from a high yield expression system, and stored in aliquots at -80°C, as described previously <sup>4</sup>.

To prepare the H268M variant of CcNiR (CcNiRH268M), the gene from the original expression system was first extended with a deca-His tag and a tobacco etch Virus (TEV) protease site, separated from each other by the polyglycine linker as follows. First a 6Xhistidine tagged construct, in which the tag and

polyglycine linker are removable from the protein by TEV protease, was created in a series of overlapping PCR reactions as illustrated in Figure 2.1a using the primers as listed in Table 2.2. Unfortunately the histidine tag was found to partially degrade under the expression conditions. To circumvent this problem the construct was extended by an additional four histidine residues, yielding the CcNiR10XHispHSG298 construct as illustrated in Figure 2. B; the two five-prime phosphorylated primers used in the process are listed in Table 2.2.

Upon satisfactory verification of the sequence, CcNiR6XHispHSG298 was used to generate a H268M mutant<sup>‡</sup> using an Agilent QuikChange Lightning site-directed mutagenesis kit with the following primers:

5'GAGACCTGGAAGATGGGCATCATGGGTAAAAATAACGTCTCGTGT3' and 5'ACACGAGACGTTATTTTTACCCATGATGCCCATCTTCCAGGTCTC3'. The H268M construct was then transformed into *S. oneidensis* by electroporation.

The transformed bacteria yielded a His-tagged CcNiR product that could be separated from crude cell lysate in a single step using a Ni affinity column, with a yield of 3 mg of pure CcNiR per liter of culture. While this yield is considerably lower than that of the expression system used to obtain CcNiR<sub>wt</sub>, it allows mutants such as CcNiR<sub>H268M</sub> to be readily separated from the constitutively expressed wild type enzyme.

---

<sup>‡</sup> This work was done by Evan Judd at Boston University.

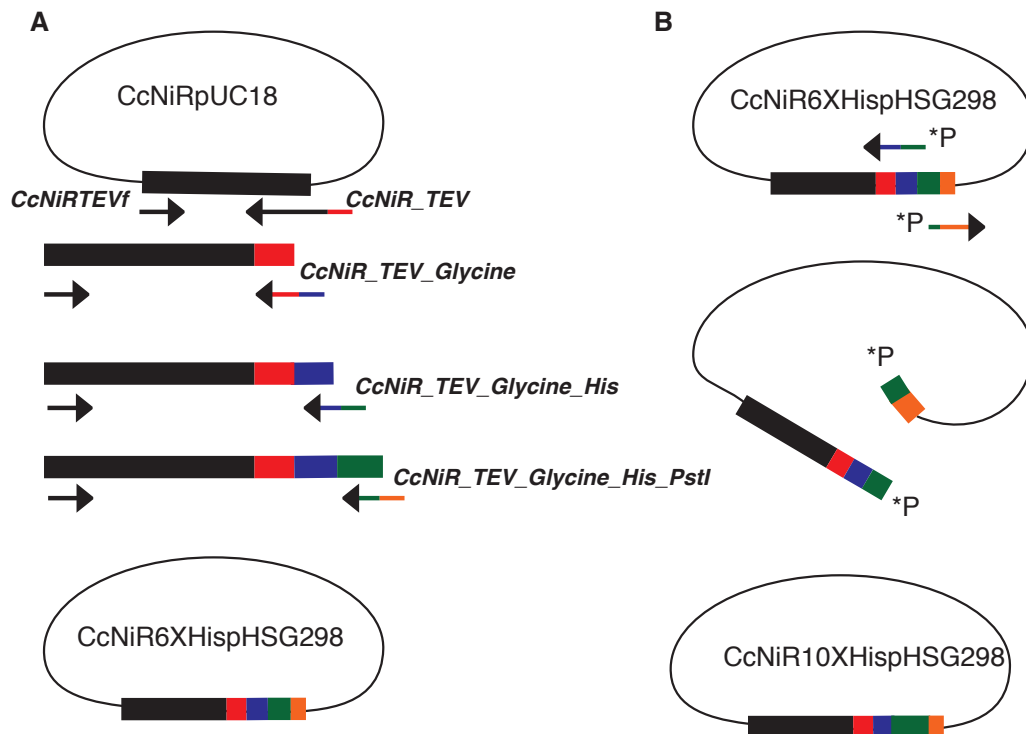


**Figure 2.1 (A)** The TEV tag, polyglycine linker and histidine tag were added to the CcNiR gene sequence at carboxyl terminus by serial PCR reaction. The forward primer CcNiRTEVf was used for all reactions. The primer sequences are listed in Table 2.2. Products from each reaction were cleaned by PCR clean up kit before subsequent amplification. Once the addition was complete, the pHSG298 and the final product were double-digested with EcoRI and PstI. The small DNA fragments that were generated by the digestion were removed using PCR clean up kit. The insert - CcNiR 6XHis and pHSG298 were ligated using T4 DNA ligase (HC) from Thermo. A maxi prep of the construct was prepared and the sequence was confirmed by Cancer Research Center DNA sequencing facility in Chicago. **(B)** Construction of 10X histidine tagged CcNiR by insertion mutagenesis. The five-prime phosphorylated primers (see Table 2.2) were used in PCR to amplify the CcNiR6XHispHSG298 construct adding four extra histidine residues. The reaction product was cleaned with PCR cleanup kit and ligated. A maxi prep was prepared for sequencing and subsequent electroporation into *S. oneidensis* TSP-C. This construct was used in site directed mutagenesis.

**Table 2.2 Primers used to generate 10X histidine tagged CcNiR in pHSG298 construct. Detailed explanation of the process is illustrated in Figure 2.1.**

Primer	Sequence	Description
CcNiRTEVf	5'AAAAAAGAATTTCGGAGGA <u>TACAATTATGTCGAAGAAAC</u> <u>TACT3'</u>	The underlined portions of the primers correspond to the template sequence, and the bold sequence corresponds to the EcoRI site.
CcNiR_TEV	5'TCCCTGAAAATACAGGTT <u>TTCCTTGTAGGTCGCCTCA</u> <u>CGC3'</u>	The underlined portions of the primers correspond to the template sequence. The rest of sequence is corresponds to reverse complement for TEV site.
CcNiR_TEV_Glycine	5'gccggaaccgccaccagagccacc <u>TCCCTGAAAATACAGGTTTT</u> <u>C3'</u>	The underlined portion corresponds to the TEV protease site. The rest of sequence is corresponds to reverse complement for poyglycine.
CcNiR_TEV_Glycine_His	5'ATGATGATGATGATGGTG <u>GCCGGAACCGCCACCAGA</u> <u>GCCACC3'</u>	The underlined portion corresponds to the glycine linker. The rest of sequence is corresponds to reverse complement for 6 histidine codones.
CcNiR_TEV_Glycine_His_PstI	5'ATATATCTGCAGTTATTAA <u>TGATGATGATGATGGTG3'</u>	The underlined portion corresponds to His-tag, the bold portion corresponds to the two stop codons, and the italicized portion is the PstI site.
NS_525(r)	5'ATGATGATGGTGGCCGGA <u>ACCGCCACCAGAGCCACC3</u> ,	The underlined portion corresponds to the glycine linker. The rest is of the sequence is corresponds to histidine.
NS_525(f)	5'CTGCAGTTATTAATGATG <u>ATGATGATGGTG3'</u>	The underlined portion corresponds to the histidine codons. The bolded sequence is two stop codons, and the italicized is the PstI recognition site.

#### 2.2.4 UV/Vis spectropotentiometric titrations of CcNiR

UV/Vis spectropotentiometry experiments were performed using a BASi Epsilon EC potentiostat to set the potential, and a CARY Bio 50 UV/Vis spectrophotometer to obtain the spectra at each applied potential. The complete apparatus was housed in an anaerobic glove box. Controlled potentiometric electrolysis of the solution was performed in an optically transparent thin-layer electrode cell similar to one used in earlier work by this group<sup>8</sup> and elsewhere<sup>9,10</sup>. A solution of CcNiR (25 – 30  $\mu$ M dimer) and redox mediators (Table 2.1) was prepared in 50 mM HEPES, 200 mM NaCl, pH 7.0. UV/Vis spectra in the range 250 – 800 nm were collected at 10 mV intervals between +50 mV and -600 mV (vs. SHE). An Ag/AgCl electrode (BASi, Model RE-5B) was used as a reference. Cyclic voltammograms of methyl viologen were collected before and after collecting the datasets, and the calculated midpoint potential ( $E_m^0 = -0.449$  V<sup>11</sup>) was used to account for any drift in the reference electrode. Spectra collected with the mediator solutions in the absence of CcNiR were subtracted from the corresponding CcNiR data sets, to account for any spectral changes due to the mediators during the titration. The corrected data sets were analyzed using programs written within the commercially available software package Mathcad 15 (PTC Software). Data analysis broadly followed the methodology used previously by this group<sup>8</sup>; details specific to this work are provided in the Results.

#### 2.2.5 Electron paramagnetic resonance (EPR) titrations of CcNiR

EPR spectra were recorded on an EleXsys E600 spectrometer (Bruker), equipped with an ER4122SHQ resonator, an Oxford Instruments ITC503 temperature controller and ESR900 helium flow cryostat (Oxford Instruments). A microwave frequency of 9.386 GHz was employed; precise frequencies were recorded for each spectrum by a built-in microwave counter. Background signals were recorded on a frozen water sample and subtracted in Xepr (Bruker Biospin) with small field corrections for slight frequency differences. Magnetic field modulation and phase-sensitive detection at 100 kHz were employed, with 5 G (0.5 mT) field modulation amplitude; other recording parameters (time constant, conversion time) were chosen such that the resolution was limited by the modulation amplitude. A microwave power of 1 mW and temperature of 10 K were employed. At higher power (*e.g.* 5 mW) rapid passage effects were clearly evident in the spectra, whereas at lower power or higher temperatures the spectra were either unacceptably noisy or certain features were relaxation-broadened beyond detection. The combination of 1 mW at 10 K with the high- $Q$  resonator thus provided the best compromise. Typical CcNiR concentrations for the experiments were 25 – 30  $\mu\text{M}$  of dimer. For EPR-spectropotentiometric titrations the samples were prepared using a bulk electrolysis cell with platinum mesh as the working electrode. In a typical experiment 4 mL of CcNiR solution were added to the bulk electrolysis cell. The sample was stirred rapidly, and the desired potential was applied. Upon stabilization, a 250  $\mu\text{l}$  subsample was removed from the cell and transferred in to an EPR tube. The EPR tube was then

placed into a test tube, which was stoppered with a butyl rubber stopper, removed from the glove box, and immediately submerged in liquid nitrogen. Samples were subsequently stored at  $-80\text{ }^{\circ}\text{C}$ , and kept on dry ice during transportation ( $< 8\text{ h}$ ).

## 2.3 Results

### 2.3.1 Effect of strong-field ligands on the EPR spectrum of CcNiR

Figure 2.2 shows the EPR spectral changes observed when a  $25\mu\text{M}$  solution of CcNiR dimer was exposed to varying concentrations of cyanide. The addition of just one equivalent of  $\text{CN}^-$  (*i.e.*  $25\text{ }\mu\text{M}$ ) extinguished a component signal of the spectrum that is characterized by a derivative-shaped signal with a trough at  $g' = 2.83$ , and diminished another characterized by EPR absorption extending from zero-field to  $g' \approx 10$ . The latter signal was enhanced in parallel mode ( $\mathbf{B}_0 \parallel \mathbf{B}_1$ ; not shown) and is characteristic of an integer-spin system. These features were previously assigned to the high-spin ( $S = 5/2$ ) Fe(III) active site, weakly exchange-coupled to one of the low-spin ( $S = 1/2$ ) hemes<sup>3</sup>, and are similar to those assigned earlier to the active site of *E. coli* CcNiR<sup>12</sup>. The effect of cyanide addition suggests that the strong-field ligand cyanide has bound to the active site and effected a high-spin to low-spin transition. Note however that because CcNiR is a dimer, addition of a single cyanide equivalent is enough to titrate only one of the two active sites in the enzyme.<sup>§</sup> In fact, residual low-field

---

<sup>§</sup> To clarify: in this article the true concentration of CcNiR dimer is reported. For convenience many earlier articles reported the concentration of CcNiR protomers in solution, which will be twice the concentration of the dimer. Extinction coefficient spectra later in the article are still reported in terms of the protomer concentration.

and  $g=3.4$  EPR absorption persisted with up to 4 eq  $\text{CN}^-$ , though with very low intensity and with a turning point at an upshifted resonant field. One can speculate, although there is no direct evidence as yet, that binding of  $\text{CN}^-$  to one active site in the dimer alters the zero-field splitting,  $\Delta$ , of the remaining high-spin ferric ion and/or the spin-spin coupling,  $\mathbf{J}$ , between the remaining high-spin and a low-spin heme, rendering the new spin system EPR-invisible (*e.g.* if some function  $f(D, J) > h\nu$ , or if  $D/J$  is such that  $g_z' \approx 0$ ; *c.f.* Hendrich & Debrunner 1989<sup>13</sup>, and Rutter et al<sup>14</sup>).

Titration of 25  $\mu\text{M}$  of CcNiR dimer with nitrite leads to EPR spectral changes very similar to those that accompany titration with cyanide (Figure 2.3). However, whereas addition of 1 equivalent cyanide leads to major suppression of the  $g = 2.92$  and  $g > 10$  signals characteristic of the coupled high-spin active site, about 200  $\mu\text{M}$  (8 equivalents) of nitrite are required to effect comparable changes. Continued addition of up to 2.7 mM of nitrite leads to subtler changes in the EPR spectrum between 1800 G and 3400 G, and also below 1000 G (changes indicated by arrows in Figure 2.3b). These changes are presumably associated with binding of nitrite to the active site of the second protomer. Around 100 equivalents (2.7 mM) of  $\text{NO}_2^-$  are required to saturate the EPR titration (bottom 3 traces of Figure 2.3a, and Figure 2.3b), compared to only 4 equivalents of  $\text{CN}^-$ .

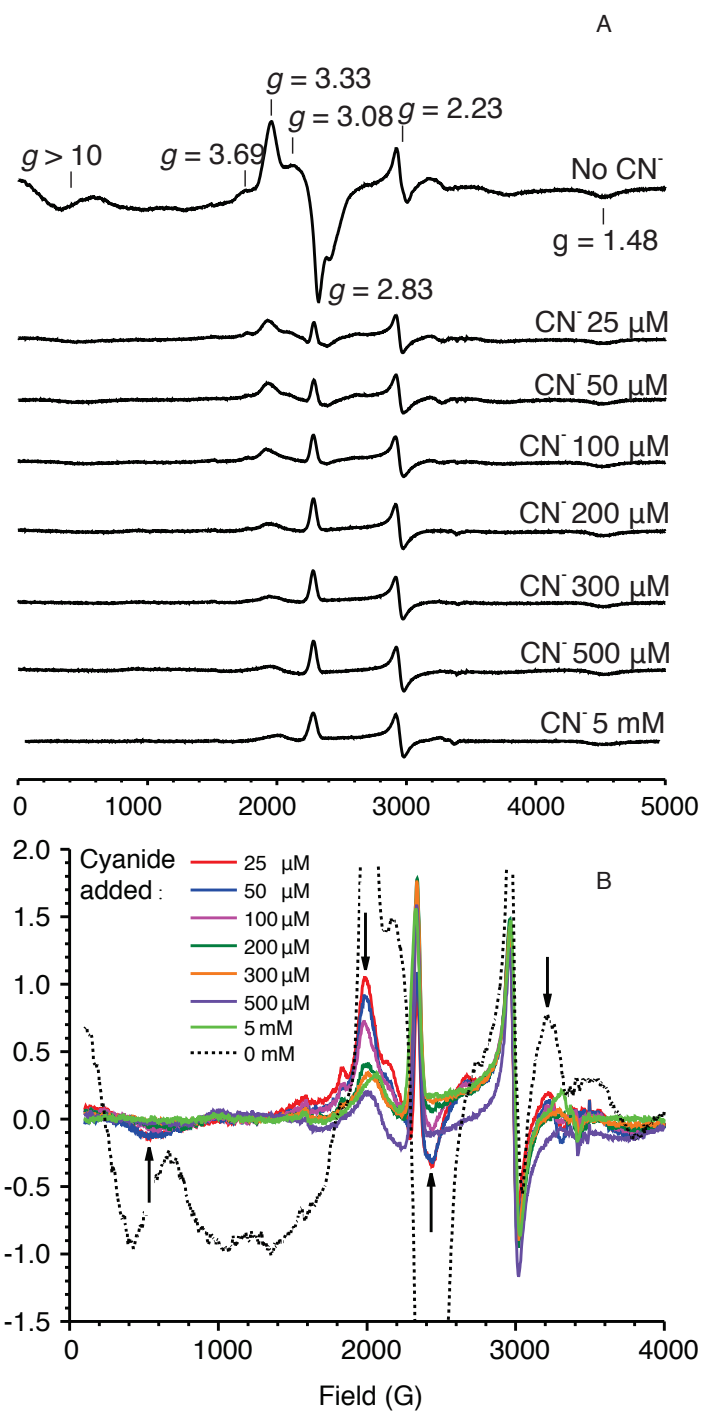


**Figure 2.2 EPR spectral changes observed when a 25 μM CcNiR dimer solution is exposed to varying concentrations of cyanide. (A) Full spectral range where signals are observed; (B) magnified view of the signals that remain after addition of the first 25 μM aliquot of cyanide.**

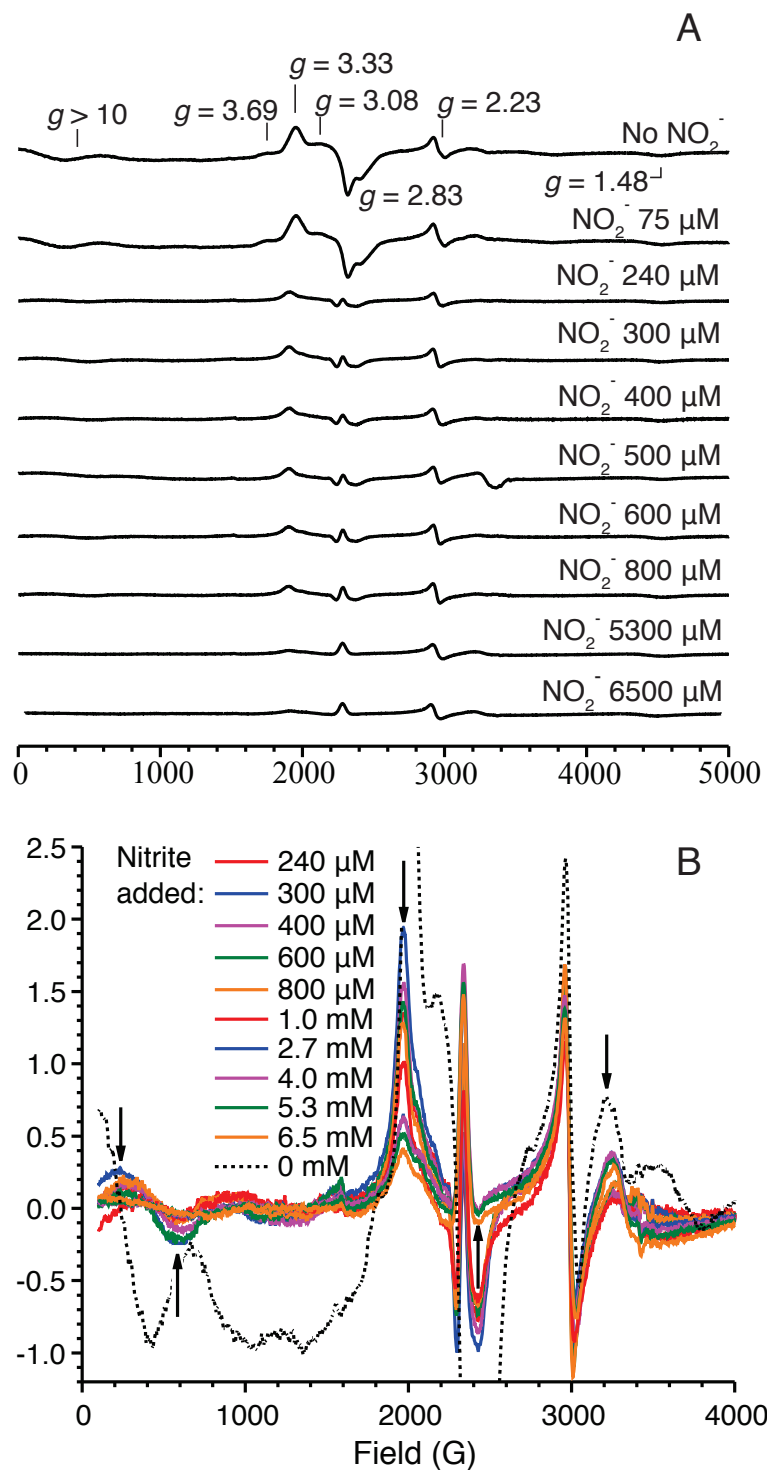


**Figure 2.3** EPR spectral changes observed when a 25  $\mu\text{M}$  ccNiR dimer solution is exposed to varying concentrations of nitrite. (A) Full spectral range where signals are observed; (B) magnified view of the signals that remain in the presence of 200  $\mu\text{M}$  nitrite.

In Figure 2.4, the spectrum obtained in the presence of 100  $\mu\text{M}$  cyanide is compared with that obtained in the presence of 2.7 mM nitrite. The two spectra are very similar, demonstrating that the ligands have comparable effects on the CcNiR EPR spectrum, though nitrite binds more weakly than cyanide. The remaining signals are assignable to low-spin Fe(III) hemes in a variety of environments. Three features at  $g_x = 2.87$ ,  $g_y = 2.24$  and  $g_z = 1.48$  can be attributed to low-spin ferric hemes with imidazoles that are parallel to each other on opposite sides of the heme plane. The weak feature seen at  $g = 3.39$  is likely of a type referred to as a “Highly Axial Low-Spin” (HALS) signal (see Section 1.2.1), which has been attributed to low-spin ferric hemes with imidazoles perpendicular to each other on opposite sides of the heme plane<sup>12,15</sup>, and/or to hemes with the plane of the axial imidazole(s) *meso* with respect to the heme nitrogens (*i.e.* bisecting the N-Fe-N right-angle<sup>16</sup>). However, HALS-type signals are also found to be typical of low-spin ferric heme cyanide model compounds<sup>17</sup>. The  $g_y$  and  $g_z$  features are also visible in the top spectra of Figures 2.2a and 2.3a, but the  $g_x$  and HALS features are obscured by the active site high-spin heme features.

The *S. oneidensis* CcNiR crystal structure reveals two hemes with imidazoles roughly perpendicular (hemes 4 and 5, Figure 2.5), and two with imidazoles parallel (hemes 2 and 3, Figure 2.5)<sup>4</sup>; more specific assignment of the corresponding EPR features is provided below.

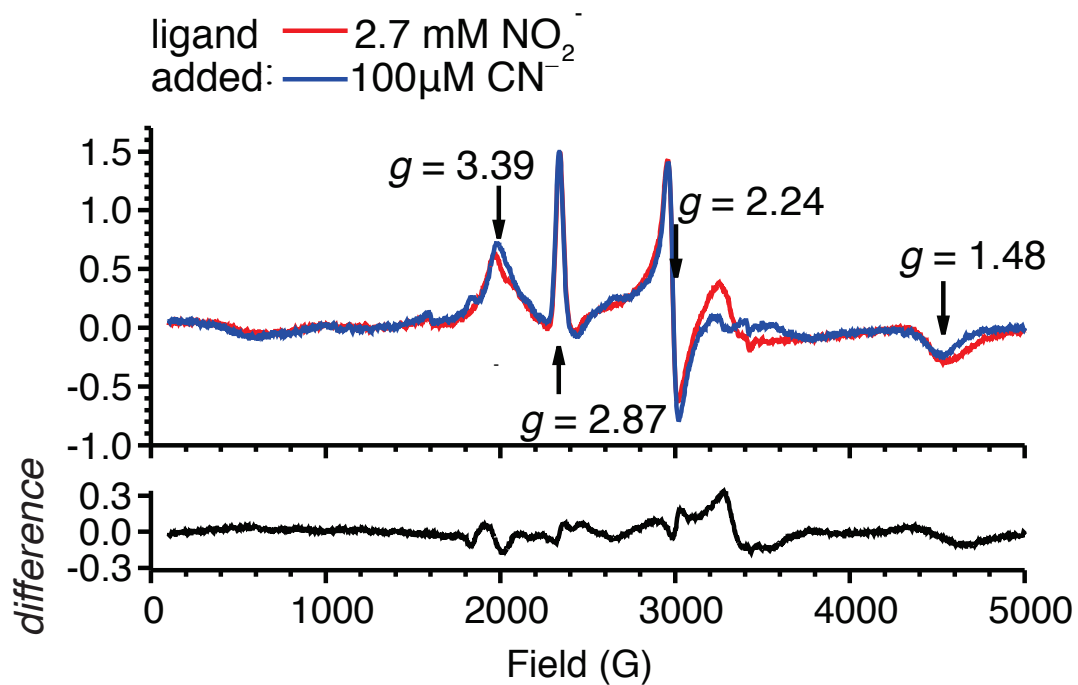


**Figure 2.4** Comparison of the EPR spectra obtained in the presence of 100  $\mu\text{M}$  cyanide (blue trace) and 2.7 mM nitrite (red trace). The residual difference between the two spectra is plotted in black below the full traces.

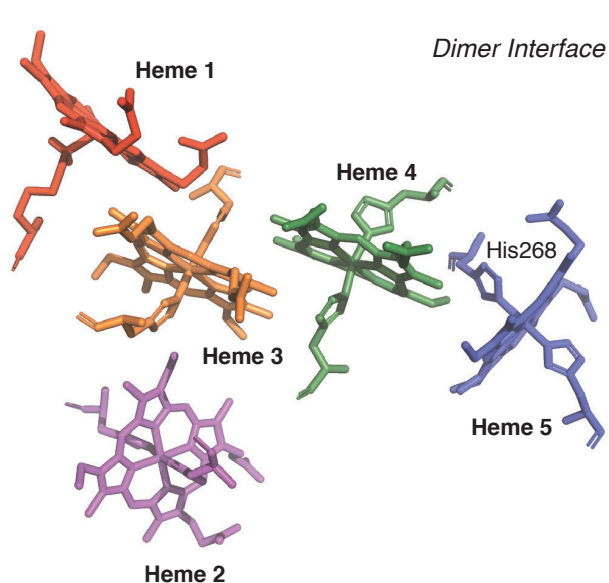
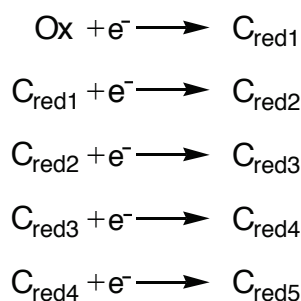


**Figure 2.5** The five hemes from one of the ccNiR protomers. The dashed vertical line represents the interface for the complete dimer. The hemes are color-coded to match spectral assignments made in the main text and Table 2.3. Histidine 268 is labeled.

### 2.3.2 Effect of cyanide on the electrochemical properties of CcNiR

Figure 2.6 shows selected UV/Visible spectral changes observed upon decreasing the potential applied to a solution initially containing 23.3  $\mu\text{M}$  fully oxidized CcNiR dimer and 75  $\mu\text{M}$  cyanide. Singular value decomposition (SVD) analysis<sup>18,19</sup> showed that five components contribute to the spectral changes. The data were thus fit to a model in which the five structurally distinct hemes in each protomer of the CcNiR dimer are successively reduced in 1-electron increments as shown in Scheme 2.1. The fitting procedure was analogous to that described previously<sup>4</sup>, and the calculated least-squares best fits are overlaid on the experimental data in Figure 2.6. By fitting the entire dataset simultaneously, extinction coefficient difference spectra were obtained for the CcNiR species  $C_{\text{red1}} - C_{\text{red5}}$  (Scheme 2.1) at varying stages of reduction (Figure 2.7 A). In addition, the concentrations of the partially reduced species as a function of applied potential were readily deconvoluted (Figure 2.7 B).

**Scheme 2.1 Reduction of fully oxidized CcNiR (Ox).  $C_{\text{red1}} - C_{\text{red5}}$  refer to the one-electron-reduced to five-electron-reduced species, respectively.**



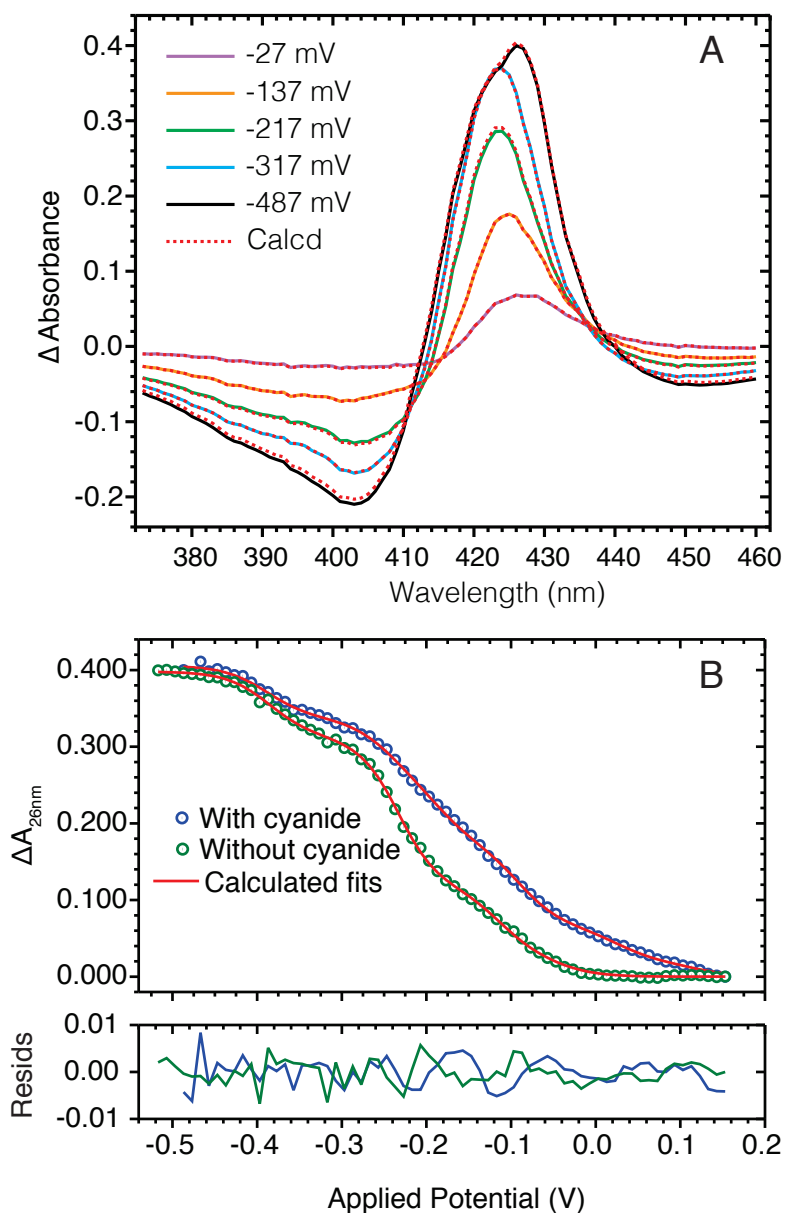


**Figure 2.6 (A) UV/Vis spectral changes obtained upon exposing a solution initially containing 23.3  $\mu$ M of fully oxidized CcNiR dimer and 75  $\mu$ M cyanide to applied potentials of -27, -137, -217, -317, and -487 mV vs the standard hydrogen electrode (SHE). Solid lines show the experimentally obtained data, whereas the dashed red lines were calculated from least-squares fitting to five Nernstian potentials, as described in ref. 4. (B) Blue circles: an absorbance difference vs. applied potential slice taken at 426 nm from the spectra of part (A); green circles: an equivalent slice obtained from a global fit of the spectral changes accompanying potentiometric reduction of a 23.3  $\mu$ M solution of CcNiR dimer in the absence of cyanide. In both cases the solid red traces are the least-squares best fits obtained from a global analysis of the data.**

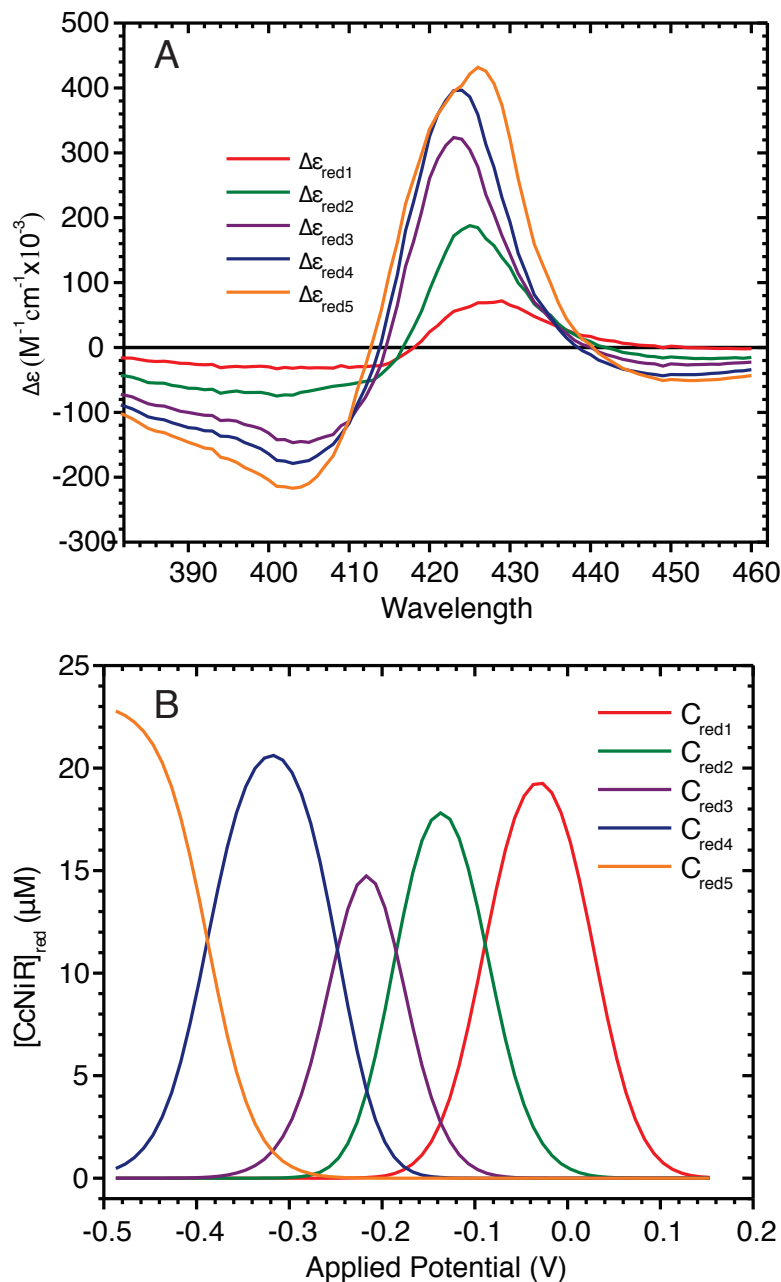


**Figure 2.7 (A)** Extinction coefficient difference spectra corresponding to each of the reduced CcNiR species  $C_{red1} - C_{red5}$  (Scheme 2.1), as calculated by the procedure described in ref. 4 for the data obtained in the presence of cyanide (Figure 2.6a). **(B)** Calculated concentrations of  $C_{red1} - C_{red5}$  as a function of the applied potential (vs SHE) for the same data. Both here and in (A) the traces are color coded to match the hemes in Figure 2.5 to which they are tentatively assigned (see text for details). Note: the values of  $C_{red1} - C_{red5}$  are given in terms of dimer concentrations, but those of  $\Delta\epsilon$  are given in terms of the protomer concentrations, to allow direct comparison with earlier reports where this was done (for example in refs. 3 and 4). The amplitudes for the  $\Delta\epsilon$  spectra corresponding to the CcNiR dimer will be twice those shown in (A).

The most striking difference observed between data collected in the presence and absence of cyanide is a 70 mV positive shift in the first midpoint potential when cyanide is present. This is seen graphically in Figure 2.6 B, and also in Table 2.3, which compare data collected using the same apparatus: the first CcNiR midpoint potential is seen to shift from -42 mV to +24 mV vs SHE. Some variability in the calculated midpoint potentials accompanies changes in apparatus (ref. 4) but in all cases the characteristic shift to higher potential was observed. Differences in the midpoint potentials associated with the remaining reduction events were much less pronounced (Table 2.3), from which we conclude that  $C_{\text{red1}}$  in Scheme 2.1 corresponds to the active site, and that binding of cyanide to this site effects the shift to higher potential.

**Table 2.3 Midpoint redox potentials for wild type CcNiR (CcNiR<sub>wt</sub>) under a variety of conditions, and for the H268M mutant (CcNiR<sub>H268M</sub>). Colors suggest possible assignments to the hemes in Figure 4, but see text for more discussion on this point.**

	CcNiR <sub>wt</sub> <sup>a</sup>	CcNiR <sub>wt</sub> + CN <sup>-</sup>	CcNiR <sub>wt</sub> + NO <sub>2</sub> <sup>-</sup>	CcNiR <sub>H268M</sub>
$\varepsilon_1^0$	-0.0440±002	0.027	0.020	0.050
$\varepsilon_2^0$	-0.110±0.004	-0.089	-0.101	-0.059
$\varepsilon_3^0$	-0.21±0.02	-0.185	NA <sup>b</sup>	-0.134
$\varepsilon_4^0$	-0.257±0.017	-0.248	NA <sup>b</sup>	-0.219
$\varepsilon_5^0$	-0.382±0.004	-0.388	NA <sup>b</sup>	-0.332

a Average of two experiments performed using the same apparatus, but different ccNiR batches. Experiments obtained using different spectroelectrochemical apparatus, or different techniques, exhibited greater variability in the midpoint potential values obtained (Supporting Information and ref 4).

b Beyond -100 mV added electrons go towards catalytically reducing nitrite, rather than towards reducing the ccNiR heme pool (see text for details).

The spectropotentiometric titrations of CcNiR in the presence and absence of added cyanide were repeated using EPR spectroscopy in place of UV/Vis, in order to correlate the observed spectral changes to specific hemes. Figure 2.8 shows the EPR spectral changes observed upon decreasing the potential applied to a solution initially containing 25  $\mu\text{M}$  fully oxidized CcNiR dimer and 100  $\mu\text{M}$  cyanide. At an applied potential of 0 mV vs SHE the most notable change is a decrease in the intensity, and shift to slightly higher field, of the  $g = 3.4$  HALS signal. This change is attributed to reduction of the active site heme, on the basis of the UV/Vis spectropotentiometric results of Figure 2.6 B that show the cyanide-bound active site reducing with a midpoint potential of +20 mV.

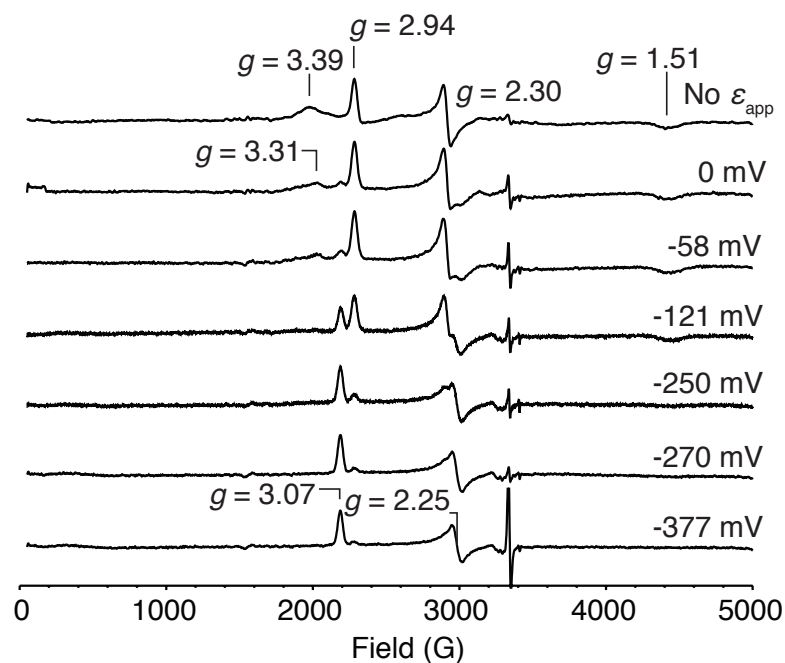


**Figure 2.8** X-band EPR spectra obtained for a solution initially containing 25  $\mu\text{M}$  of fully oxidized CcNiR dimer and 100  $\mu\text{M}$  cyanide, upon exposing it to the applied potentials shown (vs SHE).

As the potential is decreased further from 0 mV to -377 mV, a second set of rhombic signals appear with  $g_x = 3.066$ ,  $g_y = 2.300$  and  $g_z = 1.31$ , while the set with  $g_x = 2.938$ ,  $g_y = 2.248$  and  $g_z = 1.48$  eventually disappears. The residual HALS signal, now with maximum intensity at  $g = 3.32$ , disappears concomitantly with the appearance of the new rhombic set of signals. The low-spin ferric hemes 2 and 3 (Figure 2.5) with the axial imidazoles that are parallel to each other on opposite sides of the heme plane and aligned along an Fe-N axis of the heme typically display rhombic signals with two  $g$ -values  $> 2$  and  $g_3 < 2$ , with  $g_{\max} \leq \sim 3$ , while the mutually perpendicular imidazoles of hemes 4 and 5 more likely give rise to the HALS signals with  $g_{\max} \gg 3$ <sup>12,20</sup>. We attribute the rhombic signal set that grows in as the applied potential is decreased to heme 3, and the one that decreases at somewhat lower applied potential to heme 2. In this interpretation hemes 3 and 4 are coupled while both are in the ferric state, and the coupled hemes give rise to a HALS-like signal. As heme 4 is reduced the HALS-like signal disappears, and the now uncoupled heme 3 begins to display its typical rhombic signals. By correlating the UV/Vis and EPR results the midpoint potential of heme 4 is thus assigned as -89 mV, and that of heme 2 as -185 mV. (The disappearance of the heme 2 signal set somewhat lags the appearance of the heme 3 set.)

The rhombic signal set attributed to heme 3 is still present at an applied potential of -377 mV, a potential at which the UV/Vis data results show that only one heme (with midpoint potential of -388 mV, Table 2.3) remains partially

unreduced. Heme 3 is thus seen to be the last one reduced with a midpoint potential of -388 mV, while the midpoint potential of -248 mV (Table 2.3) is assigned to heme 5. The HALS signal expected for this heme was not detectable; however, a site-directed mutagenesis experiment (described below) provides additional support for the assignment of the -248 mV midpoint potential to heme 5. The color coding of the midpoint potentials listed in Table 2.3 suggests plausible assignments to the hemes in Figure 2.5, on the basis of the UV/Vis and EPR spectropotentiometric results.

At low applied potentials the EPR spectral changes that accompany a decrease in potential in the absence of cyanide (Figure 2.9) are similar to those seen in its presence (Figure 2.8). At higher potentials the changes in the absence of cyanide are different because the ferric active site starts out as high-spin, and coupled to at least one nearby low-spin heme (Figure 2.9, and also Figure 2.2). Previously the active site's characteristic signals at  $g = 2.87$  and  $g > 10$  were attributed to weak exchange-coupling with one low-spin heme, presumably heme 3 which is nearest (Figure 2.5)<sup>3,12</sup>. However, as explained above, ferric heme 3 already appears to be coupled to ferric heme 4, which raises the possibility that the characteristic active site signals actually arise from a more complex 3-way interaction between the active site (heme 1), heme 3 and heme 4.

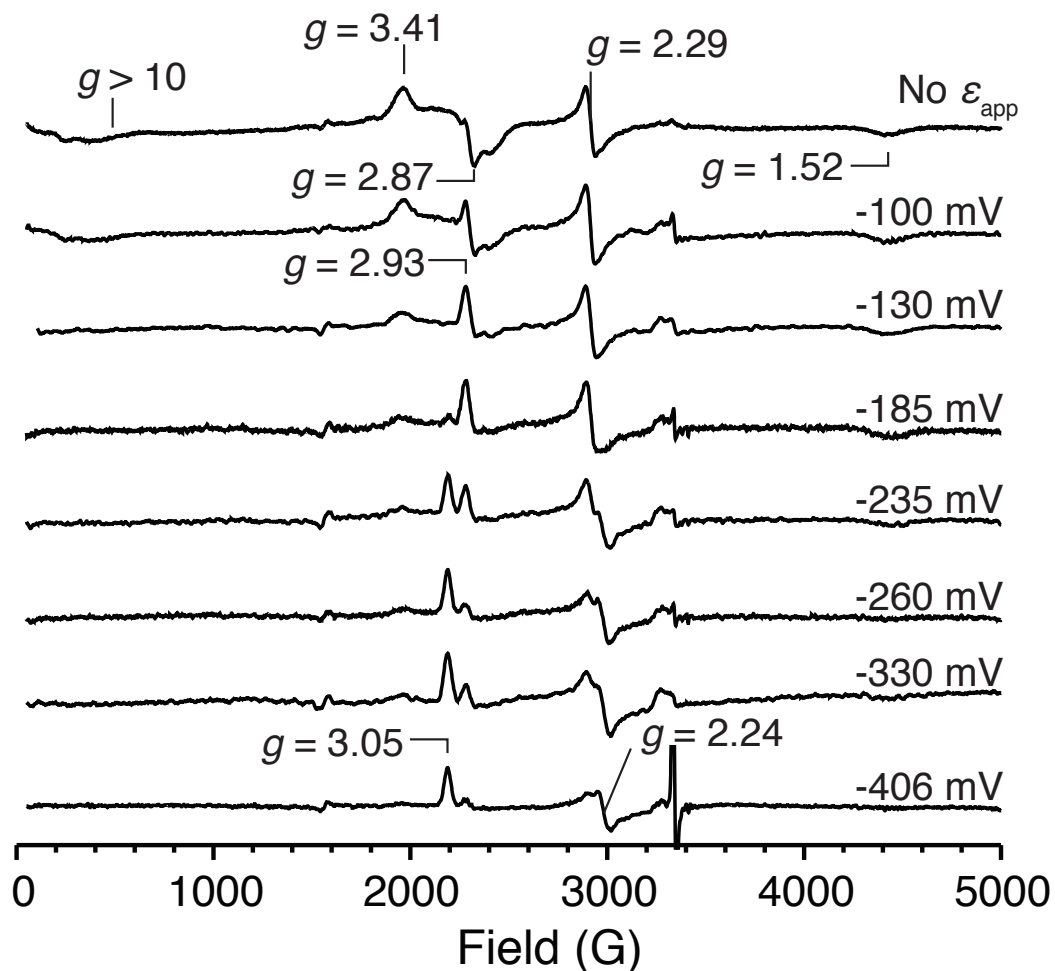


**Figure 2.9** X-band EPR spectra obtained for a solution initially containing 25  $\mu\text{M}$  of fully oxidized CcNiR dimer in the absence of any strong-field ligands, upon exposing it to the applied potentials shown (vs SHE).

### 2.3.3 UV/Vis spectropotentiometry of the H268M *S. oneidensis*

#### CcNiR mutant\*\*

In CcNiR, His268 is one of the axial ligands for heme 5 in each protomer (Figure 2.5). Figure 2.10 shows selected UV/Vis spectral changes observed upon

\*\* This work was done by undergraduate student Dan Love.

decreasing the potential applied to a solution initially containing 19.9  $\mu\text{M}$  of oxidized CcNiR<sub>H268M</sub> dimer. SVD analysis showed that only four spectral components were present above the noise level, even though CcNiR has five distinct hemes, and attempts to fit the data with four Nernstian components gave very poor results. A good fit to the data was obtained by combining the Nernst equation components for the first and second potentials into a single non-linear expression, corresponding to a single extinction coefficient spectrum. An additional parameter allowed different weight to be given to the Nernstian components corresponding to the first and second potentials. The best fit was obtained by assigning a relative contribution of 0.26 to the amplitude of the first Nernstian component, and one of 0.74 to the amplitude of the second. The calculated least-squares best fits are overlaid on the experimental data in Figure 2.10; the calculated midpoint potentials associated with each reduction event are listed in Table 2.3, together with those of wild type CcNiR (CcNiR<sub>wt</sub>) in the presence and absence of the strong-field ligands cyanide and nitrite.

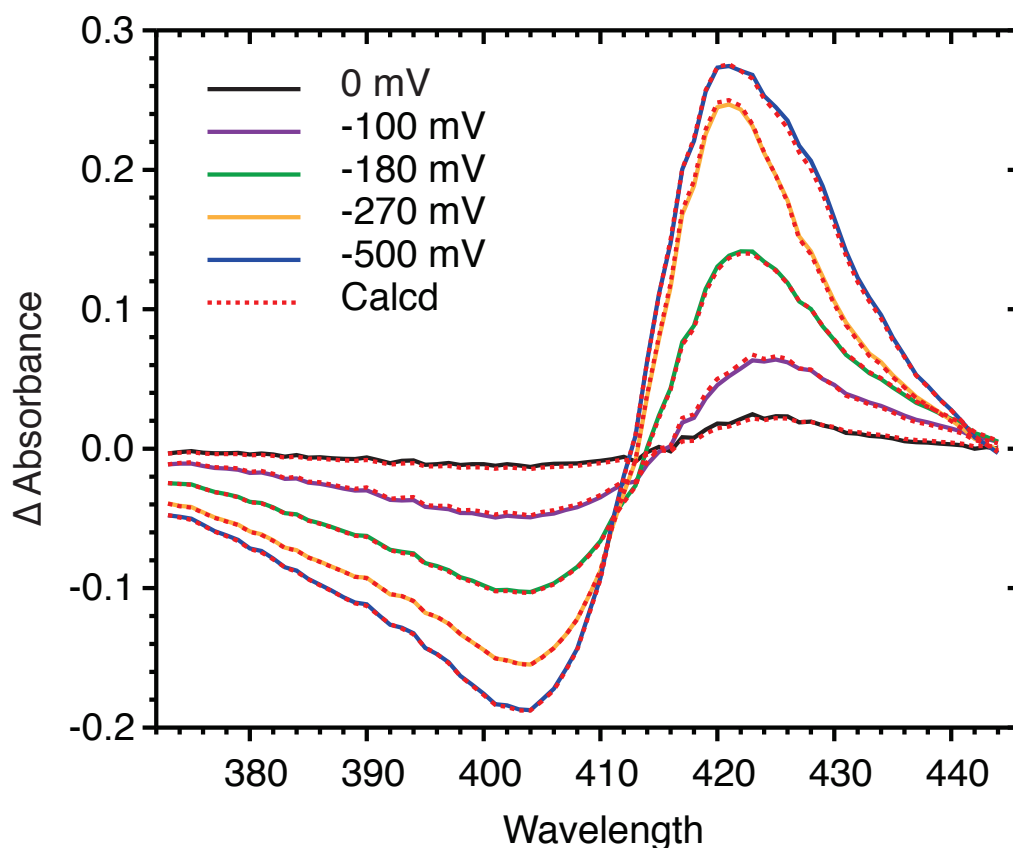


**Figure 2.10 UV/Vis spectral changes obtained upon exposing a solution initially containing 19.9  $\mu\text{M}$  of fully oxidized CcNiR<sub>H268M</sub> dimer to applied potentials of 0, -100, -180, -270, and -500 mV vs SHE. Solid lines show the experimentally obtained data, whereas the dashed red lines were calculated from least-squares fitting to four Nernstian potentials.**

As indicated by the color coding of the midpoint potentials in table 2.3,  $\varepsilon^0_2 - \varepsilon^0_5$  for CcNiR<sub>H268M</sub> most closely match  $\varepsilon^0_1 - \varepsilon^0_3$  and  $\varepsilon^0_5$  for CcNiR<sub>wt</sub>; CcNiR<sub>H268M</sub> shows no midpoint potential that closely corresponds to CcNiR<sub>wt</sub>  $\varepsilon^0_4$ . Similarly, CcNiR<sub>wt</sub> exhibits no midpoint potential that corresponds to the high potential  $\varepsilon^0_1$  of CcNiR<sub>H268M</sub>. Thus, it appears that the H268M mutation causes the CcNiR<sub>wt</sub>  $\varepsilon^0_4$  to shift dramatically to the positive, becoming  $\varepsilon^0_1$  in CcNiR<sub>H268M</sub>. This provides strong evidence that CcNiR<sub>wt</sub>  $\varepsilon^0_4$  corresponds to heme 5, whose axial ligand was mutated in CcNiR<sub>H268M</sub>.

Figure 2.11 compares the extinction coefficient difference ( $\Delta\epsilon_{\text{red1}} - \Delta\epsilon_{\text{red5}}$ ) spectra for the reduced species  $C_{\text{red1}} - C_{\text{red5}}$  obtained from the UV/Vis spectropotentiometric titrations of CcNiR<sub>H268M</sub> and CcNiR<sub>wt</sub>, respectively. For the wild type the extinction coefficient difference spectra for  $C_{\text{red4}}$  and  $C_{\text{red5}}$  ( $\Delta\epsilon_{\text{red4}}$  and  $\Delta\epsilon_{\text{red5}}$  in Figure 2.11 B) exhibit noticeable red-shifts in the signals that have maximum amplitude above 420 nm. This shift is completely absent in the spectrum  $\Delta\epsilon_{\text{red3}}$  of CcNiR<sub>H268M</sub>, but appears as a shoulder in that of  $\Delta\epsilon_{\text{red4}}$  (Figure 2.11 A). Again, this is consistent with assignment of  $\Delta\epsilon_{\text{red4}}$  to reduction of heme 5 in the wild type CcNiR<sub>wt</sub>, but not in CcNiR<sub>H268M</sub>.

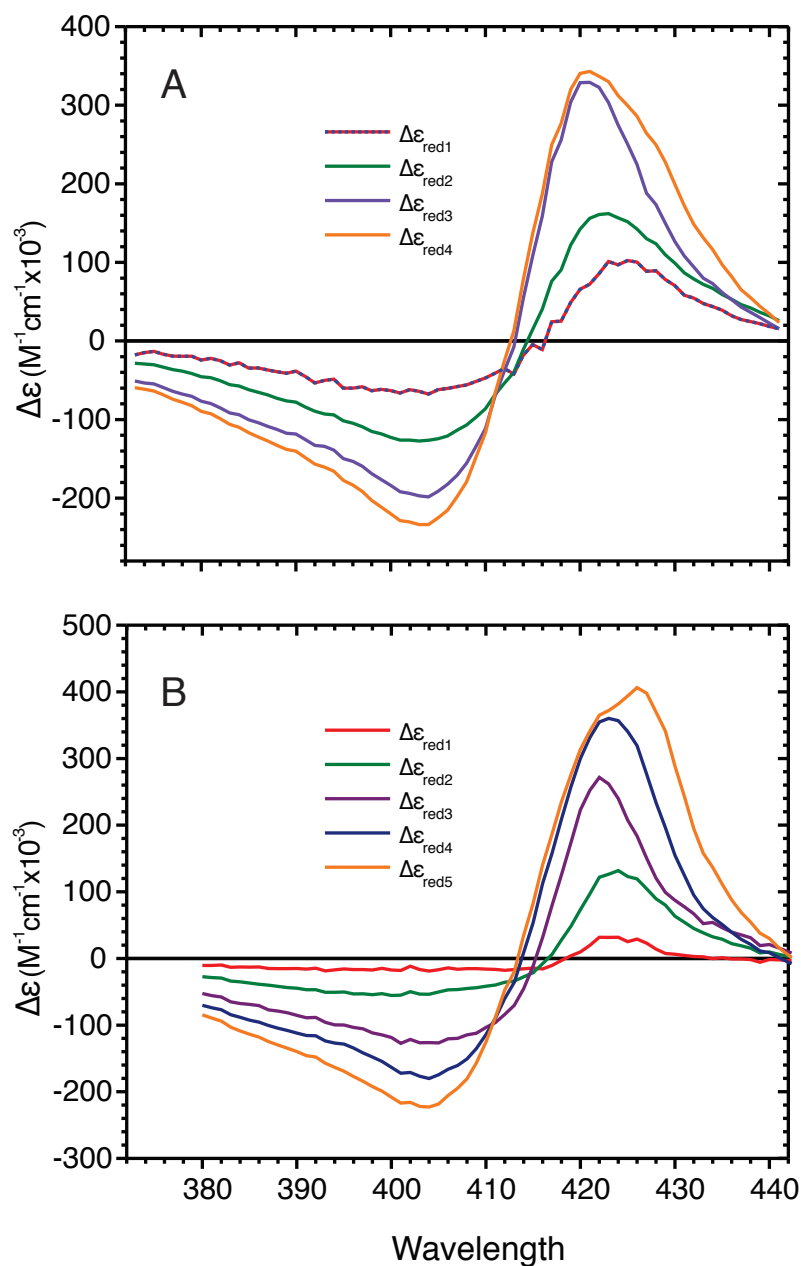


**Figure 2.11 (A)** Extinction coefficient difference spectra corresponding to spectroscopically distinct products of reduction for the mutant  $CcNiR_{H268M}$  for the data shown in Figure 2.10. **(B)** Equivalent extinction coefficient difference spectra obtained for  $CcNiR_{wt}$ ; both (A) and (B) were obtained in the absence of strong-field ligands. The spectra are color-coded to match the hemes in Figure 2.5, to which they are tentatively assigned.  $\Delta\epsilon_{red1}$  in (A) is drawn in both blue and red because in the mutant this spectral component is believed to arise from reduction of both hemes 1 and 5. Note the much-diminished red-shift in the two lowest-potential components of  $CcNiR_{H268M}$ , as compared to those of  $CcNiR_{wt}$ .

#### 2.3.4 Effect of nitrite on the electrochemical properties of CcNiR

Like cyanide, CcNiR's physiological substrate nitrite is a strong-field ligand. Figure 2.12 shows selected UV/Visible spectral changes observed upon decreasing the potential applied to a solution initially containing 29  $\mu\text{M}$  of fully oxidized CcNiR dimer and 5 mM nitrite. Slices taken in the applied potential domain (Figure 2.12 B) clearly show two distinct reduction events, one centered near 20 mV vs SHE and the other near -100 mV vs SHE. Thus, as it is in the presence of cyanide, the first reduction event is shifted roughly 70 mV to the positive compared to the first reduction event observed in the absence of strong-field ligands (Table 2.3). Of note SVD analysis reveals only a single spectral component characteristic of *c*-heme reduction, which is also revealed by the presence of a tight isosbestic point at 418 nm in Figure 2.12 A, without the need for sophisticated analysis. This result means that the two electrochemical events generate reduced heme species that are spectroscopically indistinguishable from one another.

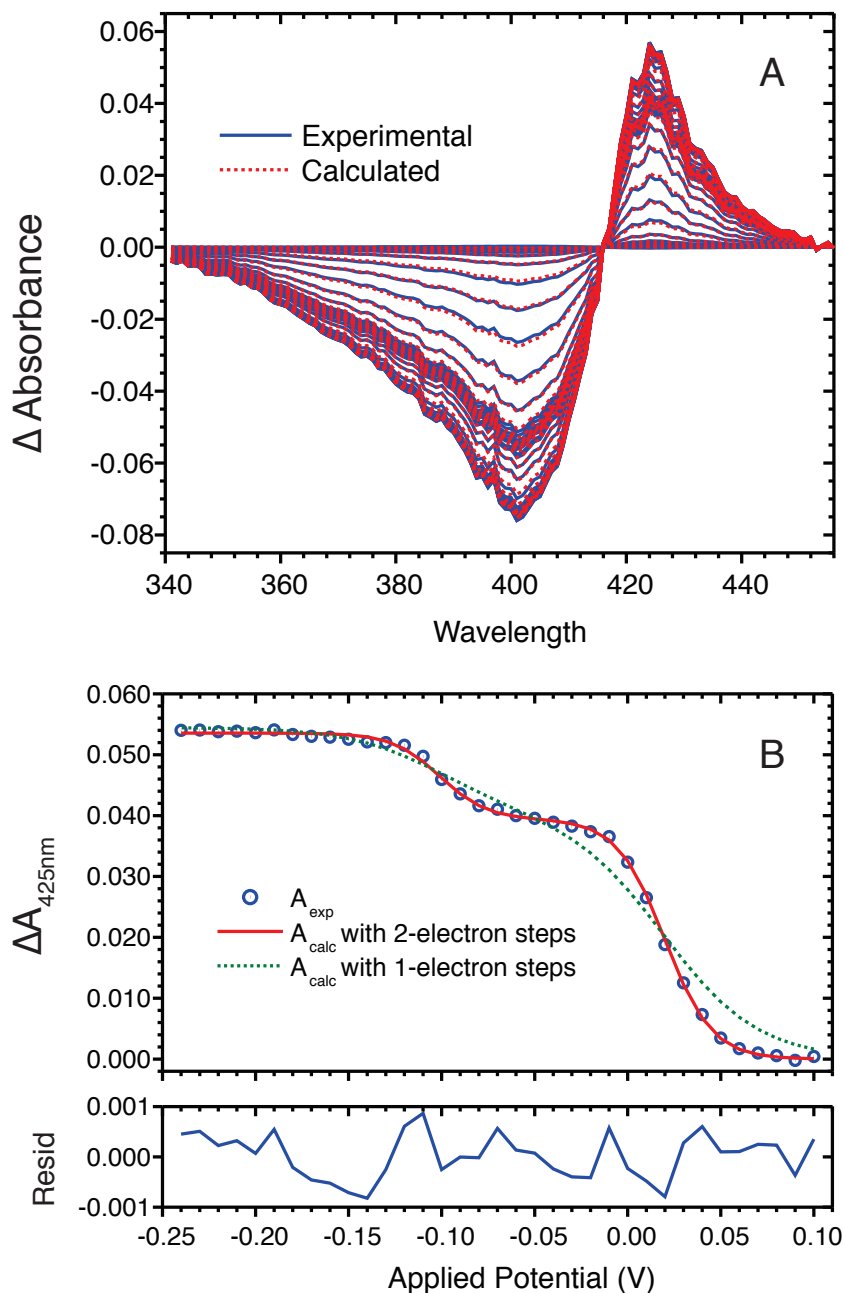


**Figure 2.12(A)** UV/Vis spectral changes obtained upon exposing a solution initially containing 29  $\mu\text{M}$  of fully oxidized CcNiR<sub>wt</sub> dimer and 5 mM nitrite to progressively lower potentials. Solid blue lines show the experimentally obtained data, whereas the dashed red lines were calculated from least-squares fitting with two Nernstian 2-electron reduction events, and one spectral component. **(B)** Blue circles: an absorbance difference vs. applied potential slice taken at 425 nm from the spectra of part (A); solid red line: least-squares best fit obtained from global analysis of the data with two Nernstian 2-electron reduction events; dotted green line: least-squares best fit obtained from global analysis of the same data with two Nernstian 1-electron reduction events.

Beyond the first two, no further heme reduction steps can be observed using spectropotentiometry, presumably because as the applied potential is decreased below about -120 mV vs SHE, catalytic reduction of the bound nitrite ensues. Stated another way, additional electrons go to reducing the bound substrate rather than to the CcNiR heme pool. The onset of catalysis at potentials below -120 mV vs SHE is in agreement with protein film voltammetry (PFV) results reported earlier for *S. oneidensis* CcNiR<sup>8</sup>.

The Figure 2.12 data were fit in a manner analogous to that described earlier for CcNiR under other conditions (above and in ref 4), but with one important difference in the model used. Under all conditions previously investigated, CcNiR heme reductions invariably proceeded via 1-electron steps as shown in Scheme 2.1. On the other hand, each reduction event in the presence of nitrite was clearly seen to be a concerted 2-electron process (Figure 2.12 B). The results of EPR spectropotentiometry experiments provide explanation for the concerted two electron transfer (Figure 2.13). When the applied potential was poised below the first midpoint potential of 20 mV, major new signals appeared at  $g = 2.08$  and  $g \sim 2.0 - 2.2$ . This pattern of  $g$  values is characteristic of  $\{\text{Fe}(\text{NO})\}^7$  heme moieties<sup>21-25</sup>, where  $\{\text{Fe}(\text{NO})\}^7$  is the Enemark-Feltham notation representing resonance forms of a species that formally has  $\text{NO}^{\bullet}$  bound to Fe(II) or  $\text{NO}^-$  bound to Fe(III)<sup>26</sup>. Unlike  $\{\text{Fe}(\text{NO})\}^7$  in other ligand systems, all heme  $\{\text{Fe}(\text{NO})\}^7$  systems characterized to date display an  $S = 1/2$  ground state, and their EPR signals are typically broadened substantially by <sup>14</sup>N

ligand hyperfine splitting<sup>21</sup>. Thus it appears that, when nitrite is bound at the CcNiR active site, the first reduction event proceeds via a concerted 2-electron process that formally places one electron on the iron and the second on the nitrogen moiety (Scheme 2.2).

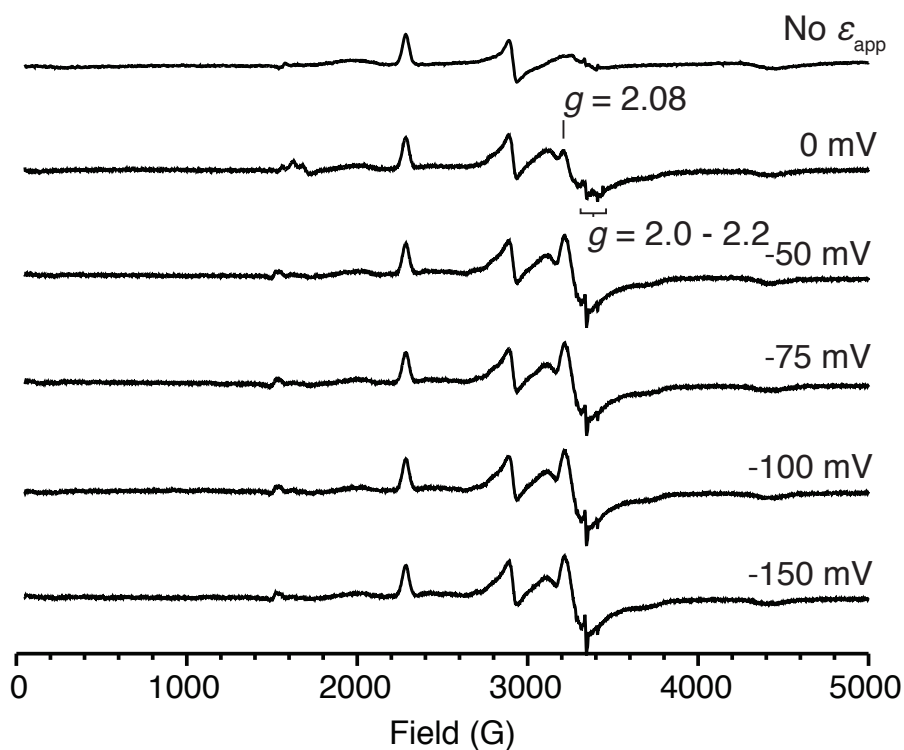
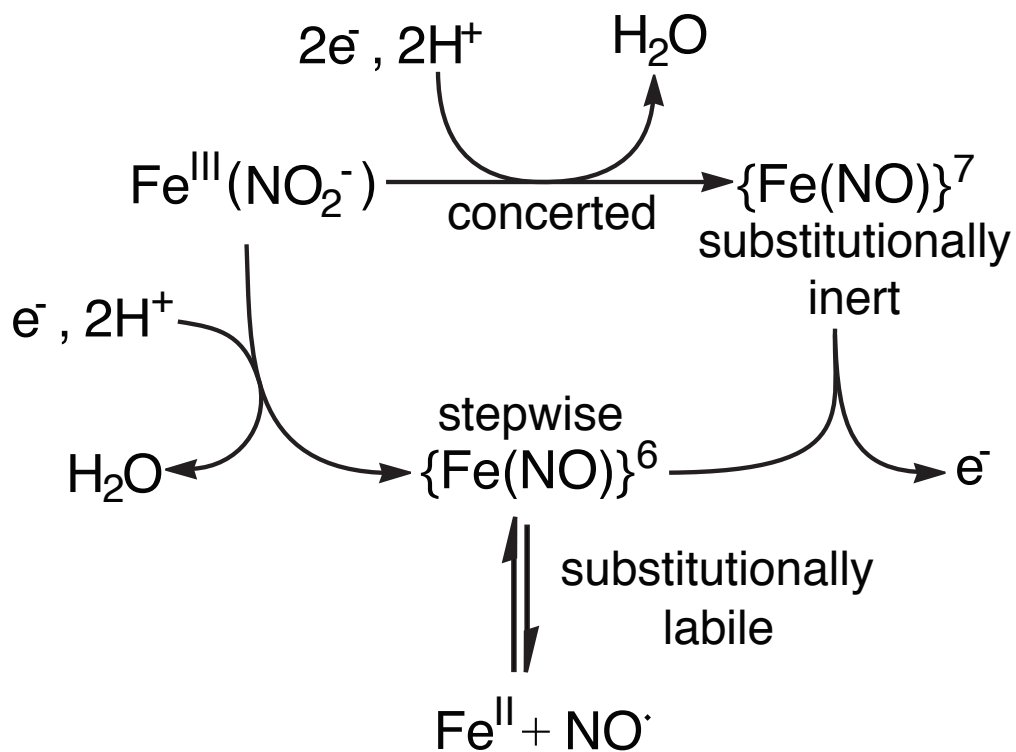


**Figure 2.13** X-band EPR spectra obtained for a solution initially containing 25  $\mu\text{M}$  of fully oxidized CcNiR dimer and 5 mM nitrite, upon exposing it to the applied potentials shown (vs SHE).

Scheme 2.2 An  $\{\text{Fe}(\text{NO})\}^7$  species may form in two ways; concerted or stepwise reduction of iron nitrite complex. This study suggests that concerted mechanism is more likely.



The UV/vis results of Figure 2.12 show that the second reduction event is also best fit as a two-electron process. However, the amplitude of the spectral change associated with this event is only about 1/3 that associated with the first event. No obvious EPR spectral changes are associated with the second reduction, with the exception of a set of minor signals at  $g = 4.13$  and  $g = 3.95$ ,

that appear as the potential is reduced to 0 mV, but then decrease again as the potential is lowered further (Figure 2.13). Signals in this region are characteristic of ferric hemes with intermediate spin states  $S = 3/2$ , and are typically observed in model ferric heme complexes that have very weak field axial ligands, and thus very large tetragonal distortion<sup>27</sup>. Such a set of signals was observed in EPR spectra of the tetraheme protein cytochrome *c<sub>554</sub>* in the presence of its electron donor HAO when this was partially reduced, but in that case was attributed to the presence of an impurity<sup>28</sup>. For the present we defer judgment on whether the  $S = 3/2$  signals seen in Figure 2.13 arise from a functional CcNiR or from an impurity. Even if they do arise from a functional CcNiR, they do not for the moment provide any clues as to the nature of the second 2-electron reduction event seen in Figure 2.12; hence, this question is not considered further herein.

## 2.4 Discussion

### 2.4.1 Titrations of CcNiR with cyanide and nitrite

Shortly after publication of the first CcNiR structures, Einsle and coworkers predicted on the basis of a computational study that the active site iron of CcNiR would be low-spin when nitrite occupied the distal site, whether the iron was oxidized or reduced<sup>29</sup>. This was confirmed experimentally for the oxidized enzyme in a resonance Raman investigation of *D. vulgaris* CcNiR<sup>30</sup>, and more recently in an EPR experiment by this group for the *S. oneidensis* CcNiR<sup>3</sup>. The original computational studies also showed that the bias towards low-spin would be significantly more pronounced for the ferrous active site due to nitrite's  $\pi$ -

accepting properties<sup>29</sup>. The current investigation has shown that nitrite binds to the oxidized active site several orders of magnitude more weakly than cyanide, another strong-field ligand. Moreover, Figures 2.2 and 2.3 clearly show that binding of a ligand to the second protomer is significantly more difficult than binding to the first.

The active site EPR spectral features that remain after the first protomer has been bound by nitrite or cyanide retain the essential characteristics of the enzyme in the absence of these ligands. However, the signal at  $g > 10$  has shifted somewhat, and both this signal and the ones at  $g \approx 3.3$  and  $2.8$  have diminished in intensity much more dramatically than would be expected for titration of half the active sites if the two protomers were behaving identically (Figures 2.2b and 2.3b). A likely explanation is that, after titration of the first protomer, the second protomer remains in the  $S = 5/2$  and continues to interact with at least one nearby  $S = 1/2$  heme, but that subtle conformational changes triggered by cyanide or nitrite binding to the first protomer change the coupling constant  $J$  for the spin-spin interactions of the second protomer. It has been noted that the shapes and intensities of EPR signals arising from weak ( $J \sim 1 \text{ cm}^{-1}$ ) coupling between  $S = 5/2$  and  $S = 1/2$  metal centers, such as those seen for CcNiR, are extremely sensitive to small changes in  $J$ <sup>31,32</sup>. We return to this point in Chapter 3.

Asymmetric behavior by the essentially identical CcNiR subunits has been noted on several occasions in the past. For example, protein film voltammetry

(PFV) revealed the presence of two distinct sites for cyanide binding and inhibition of *E. coli* CcNiR, one with higher and the other with lower binding affinity<sup>33</sup>. The PFV study identified cyanide as a mixed inhibitor, and suggested cooperative binding to the CcNiR active sites as one of several possible explanations. In a more recent PFV study, negative cooperativity was observed during hydroxylamine reduction catalyzed by *S. oneidensis* CcNiR<sup>8</sup>. Perhaps the most intriguing example of asymmetric behavior was observed in the crystal structure of the complex between *D. vulgaris* CcNiR and its physiological electron donor, a tetraheme quinol dehydrogenase referred to as NrfH<sup>34</sup>. CcNiR and NrfH formed a large quaternary complex consisting of two CcNiR dimers and two NrfH monomers, in which only one CcNiR protomer from each dimer was in intimate contact with NrfH. This finding suggested that even under physiological conditions the CcNiR subunits behave asymmetrically, with the electrons entering via one subunit only, and then spreading to the two active sites via inter-subunit electron transfer.

#### 2.4.2 Order of heme reduction in CcNiRs from different organisms

By combining results of the UV/Vis and EPR spectropotentiometric titrations it proved possible to assign midpoint potentials to the five hemes in each protomer of *S. oneidensis* CcNiR<sub>wt</sub> and CcNiR<sub>H268M</sub>, under a variety of conditions (Table 2.3). Some of the *E. coli* CcNiR heme midpoint potentials were similarly assigned in two earlier studies, using a combination of magnetic circular dichroism<sup>35</sup> and EPR<sup>12</sup> spectropotentiometries. Though the

spectropotentiometric behaviors for the *S. oneidensis* and *E. coli* CcNiRs are similar superficially, closer inspection reveals some striking differences between the two enzymes.

The biggest difference observed between the *S. oneidensis* and *E. coli* CcNiR spectropotentiometric profiles is seen in the midpoint potential of heme 2 (Figure 2.5), which is substantially higher in *E. coli* CcNiR than it is in the *S. oneidensis* enzyme (-37 mV, ref. <sup>12</sup> vs -214 mV, Table 2.3, in the absence of strong-field ligands). The *E. coli* and *S. oneidensis* enzymes are structurally very similar, but the region in which they differ most significantly is on the protein surface near heme 2 <sup>4</sup>. This region appears to be the physiological entry point for electrons <sup>12,34</sup>, and the structural difference is believed to reflect the fact that *E. coli* and *S. oneidensis* CcNiR use different physiological electron donors, with *E. coli* using NrfB and *S. oneidensis* using CymA <sup>4</sup>. Visual inspection of the *E. coli* and *S. oneidensis* CcNiR structures in space-filling mode (Figure 2.14) reveals that the propionate group of heme 2 is neutralized by hydrogen bonding with Arg 201 in the *E. coli* structure, whereas it is solvent exposed in the *S. oneidensis* CcNiR. Propionate neutralization has been shown to provoke significant positive shifts in heme midpoint potentials <sup>36</sup>, and thus could account for the difference observed here. The heme edge in the *S. oneidensis* enzyme also appears to be somewhat more solvent exposed than that in the *E. coli* enzyme (Figure 2.14); a decrease in solvent exposure is likewise known to shift heme midpoint potentials in the positive direction <sup>37</sup>.

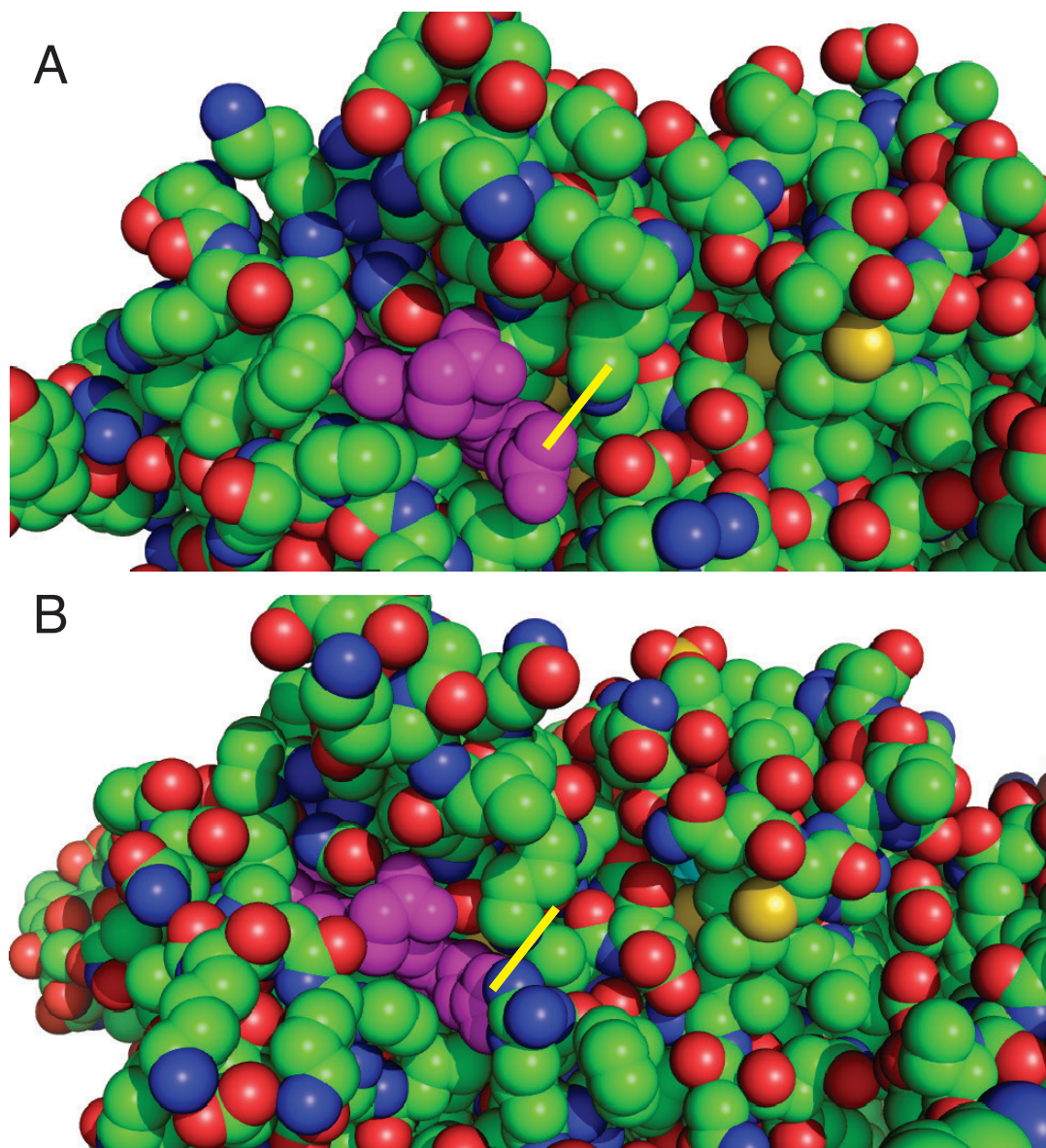


**Figure 2.14** Space-filling view of the CcNiR surface in the vicinity of heme 2 (purple) for (A) the *S. oneidensis* enzyme; and (B) the *E. coli* enzyme. The yellow arrows point to the heme propionate that is solvent-exposed in the *S. oneidensis* enzyme, but hydrogen-bonded to Arg 201 in the *E. coli* enzyme.

For *E. coli* CcNiR both MCD and EPR clearly show that the active site (heme 1, Figure 2.5) is the second heme reduced, after heme 2, with a midpoint potential of -107 mV<sup>12,35</sup>. By contrast, in the *S. oneidensis* enzyme the active site reduces first, with a midpoint potential of -44 mV in the absence of strong field ligands, and one of +20 mV in their presence (Table 2.3). Interestingly, an early EPR spectropotentiometric titration of the *D. Vulgaris* CcNiR suggested that the active site of this enzyme was one of the *last* hemes to reduce, with a midpoint potential of ~ -210 mV<sup>38</sup>.

For *S. oneidensis* CcNiR, reduction of the heme with the second-highest midpoint potential (-110 mV, Table 2.3) triggered the appearance of a rhombic signal (Figures 2.8 and 2.9), which was assigned to heme 3 (Figure 2.5; see Results section). From this observation the -110 mV midpoint potential was assigned to heme 4 (Figure 2.5), based on the rationale that hemes 3 and 4 are magnetically coupled when they are oxidized, so that the heme 3 signals become visible only after heme 4 is reduced. The assignment is further supported by the concomitant disappearance of the HALS signal at  $g \approx 3.3$  (Figures 2.8 and 2.9), which can only arise from either heme 4 or 5 (since heme 1 is already reduced). Pereira et al. also reported seeing signals appear in the EPR spectrum of the *D. vulgaris* CcNiR as hemes uncoupled during reduction<sup>38</sup>, though in that case spectral interpretation was complicated by the fact that the *D. vulgaris* enzyme is isolated as a complex with the tetraheme NrfH (see above), which adds four extra hemes to the mix.

Detection of the heme 3 signals for *S. oneidensis* CcNiR greatly simplified the unambiguous assignment of the EPR spectra for this enzyme. These signals are still visible at the lowest potential monitored (-377 mV and -406 mV in Figures 2.8 and 2.9, respectively), showing that heme 3 is the last one reduced. With the reduction order of hemes 1, 2 and 4 also assigned above, this leaves heme 5 as the only one whose reduction order can't be assigned directly from the combination of EPR and UV/Vis spectropotentiometry. Nevertheless heme 5 can be shown to reduce fourth (with midpoint potential of -257 mV, Table 2.3) by a process of elimination, and also by comparing the electrochemical behaviors of CcNiR<sub>wt</sub> and CcNiR<sub>H268M</sub> (see Results). In the case of *E. coli* CcNiR the trio of rhombic signals expected for heme 3 was not detected at any applied potential, which to date has made it impossible to unambiguously assign any low-spin hemes other than heme 2<sup>12,35</sup>. As for *S. oneidensis* CcNiR only one HALS signal was clearly detectable in the *E. coli* enzyme, and this was associated with a reduction event centered at a midpoint potential of -292 mV<sup>12,35</sup>. Such a value most closely corresponds to that of the *S. oneidensis* enzyme's heme 5 midpoint potential, though as seen above one can't assume that hemes from the two enzymes will exhibit comparable potentiometric behavior, despite their structural similarity.

It is perhaps instructive to rationalize some aspects about the order of heme reduction for *S. oneidensis* CcNiR on the basis of the following simple Coulombic argument. First, when electrons are added to hemes 1, 2 and 4, the reduced hemes are separated from each other by the oxidized hemes 3 and 5 (Figure 2.5). This arrangement will lead to lower coulombic repulsions between reduced hemes than any permutation in which three electrons are added to each protomer so as to reduce either heme 3 or heme 5; such permutations all force electrons to go on adjacent hemes. Once three electrons have been added to each protomer, the fourth electron will have to go to either heme 3 or heme 5. Both options will put reduced hemes in direct contact with each other. However, heme 3 sits at the branch point between hemes 1, 2 and 4 within one protomer, and so will be surrounded by *three* reduced hemes, whereas heme 5 will be surrounded by two: heme 4 from the same protomer, and heme 5 from the adjacent one (Figure 2.5). Clearly an electron added to heme 5 would experience less repulsion, so one would predict that this heme would reduce before heme 3, as is observed experimentally. A similar pattern in the order of heme reduction was observed for HAO from the ammonia oxidizing bacterium *Nitrosomonas europaea*, a homotrimer that contains 8 hemes/monomer, and whose arrangement bears many similarities to the heme arrangement in the CcNiR dimer<sup>39,40</sup>. In the case of HAO, the coulombic rationale was supported by a computational study<sup>41</sup>. Note also that this rationale doesn't contradict anything that has been confirmed so far for the order of heme reduction in *E. coli* CcNiR:

hemes 1 and 2 are among the first reduced, even if in a different order than seen for the *S. oneidensis* enzyme, and heme 5 *may* be among the last reduced<sup>12,35</sup>.

The observed difference in order of heme reduction between the *S. oneidensis* and *E. coli* CcNiRs suggests that a specific order is not critical to CcNiR function, since the two enzymes exhibit virtually identical specific activities<sup>4</sup>. This might seem surprising, but one should bear in mind that differences in midpoint potentials measured experimentally in a protein with multiple redox-active sites are typically much larger than the differences felt by a single electron moving from site to site in an otherwise fully oxidized protein, which is a much more physiologically relevant scenario. The reason for this is that it is impossible to measure the midpoint potential of a low potential redox-active site until one has reduced the higher-potential sites in the same protein, and each additional electron added to the protein will decrease the midpoint potentials of the remaining sites due to increased coulombic repulsion<sup>41</sup>. An extraordinary example of this is observed for the midpoint potentials of HAO<sup>41-43</sup>. The midpoint potentials of the 8 HAO hemes from each protomer were resolved using spectropotentiometry, and found to span a dramatically wide range of 700 mV, from +288 mV to -412 mV<sup>42,43</sup>. However, in a computational study wherein a single electron was moved from heme to heme in fully oxidized HAO, the heme midpoint potentials spanned a range of only 417 mV, from +264 mV to -153 mV<sup>41</sup>. The 417 mV range reflects the effects of the local environment on the individual HAO hemes, while the additional ~300 mV difference observed in the

spectropotentiometric titrations arises because the lower potential hemes are reduced *after* the higher potential ones, and their midpoint potentials are affected by these prior reductions.

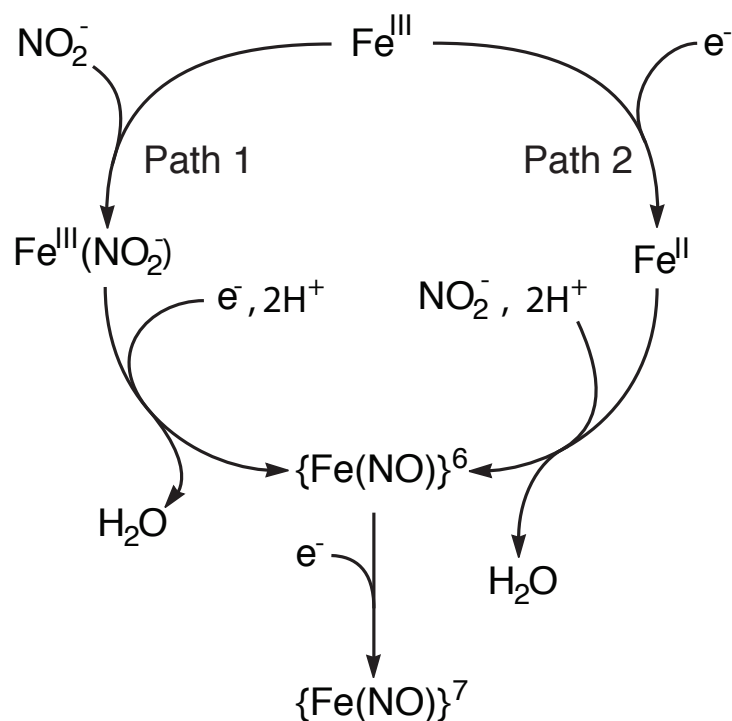
### 2.4.3 Nitrite reduction at the CcNiR active site

The results of this study show that, when occupied with nitrite, reduction of the CcNiR active site occurs by a concerted 2-electron process, which generates the  $\{\text{Fe}(\text{NO})\}^7$  moiety (Figures 2.12 and 2.13, and Scheme 2.2). Interestingly, the  $\{\text{Fe}(\text{NO})\}^7$  signal was previously observed in a very early EPR study of the *D. desulfuricans* CcNiR<sup>44</sup>, but has since been discounted as a putative reactive intermediate (see below). Physically a concerted 2-electron reduction indicates that addition of a second electron to a redox-active center is much more favorable than addition of the first. Under these circumstances, applying a potential sufficient to prompt the first reduction step simultaneously initiates the second step as well. In the case of CcNiR it appears that reduction of the  $\text{Fe}^{\text{III}}(\text{NO}_2^-)$  active site to  $\{\text{Fe}(\text{NO})\}^6$  has the measured midpoint potential of 20 mV, but subsequent reduction of  $\{\text{Fe}(\text{NO})\}^6$  to  $\{\text{Fe}(\text{NO})\}^7$  has a much higher midpoint potential, so the intermediate  $\{\text{Fe}(\text{NO})\}^6$  can't accumulate (Scheme 2.2).

Evolution of CcNiR so that it reduces bound nitrite in a 2-electron process makes sense from a physiological standpoint. Previous studies with both model and hemoprotein systems have shown that NO typically binds very tightly within  $\{\text{Fe}(\text{NO})\}^7$  species, but weakly in  $\{\text{Fe}(\text{NO})\}^6$  species<sup>45-48</sup>. Thus, by disfavoring the  $\{\text{Fe}(\text{NO})\}^6$  intermediate, the CcNiR design ensures that toxic NO is not released

from the enzyme during catalytic turnover. Of course the conditions employed in this study, whereby the oxidized active site was first saturated with millimolar concentrations of nitrite and then reduced, are unlikely to ever occur physiologically. Instead, active site reduction almost certainly precedes nitrite binding *in vivo*<sup>29,49</sup>; as a strong  $\pi$ -acceptor nitrite will bind much more strongly to the electron-rich ferrous active site, thus allowing the site to be fully occupied at much lower concentrations. The relative order of nitrite and electron addition, however, will not affect the thermodynamic conclusions made above (Scheme 2.3).

**Scheme 2.3** In the experiments described herein active site reduction in the presence of nitrite appears to proceed via Path 1. Under physiological conditions it will likely proceed via path 2.



Computational studies described in previous reports predicted that a  $\{\text{Fe}(\text{NO})\}^7$  active site will constitute a thermodynamic minimum in CcNiR<sup>29,50</sup>. This in turn led to the suggestion that  $\{\text{Fe}(\text{NO})\}^7$  constitutes a kinetic trap that sits off of the reaction pathway from nitrite to ammonia, and to several suggestions for how the species could be bypassed during catalysis<sup>29,50</sup>. The present results confirm that the  $\{\text{Fe}(\text{NO})\}^7$  active site does indeed constitute a thermodynamic minimum, but in no way rule out its possible role as a catalytic intermediate. The results show that at applied potentials between  $\sim 0$  mV and  $-100$  mV nitrite reduction at the active site will lead to formation of  $\{\text{Fe}(\text{NO})\}^7$  only, with no catalysis. However, if the potential is further decreased below  $-120$  mV, catalytic reduction to ammonia will then ensue. Whether reduction starting from  $\{\text{Fe}(\text{NO})\}^7$  is slower than the CcNiR catalytic turnover rate remains an open question. The alternative possibility is that  $\{\text{Fe}(\text{NO})\}^7$  is a true catalytic intermediate whose degree of accumulation depends exclusively on the applied potential: at low potentials the species is rapidly reduced and doesn't accumulate, while at higher potentials it is trapped and catalysis ceases. Studies to distinguish between these possibilities are now under way.

Future studies will also be needed in order to understand the significance of the fact that, even at very low applied potentials in which CcNiR is turning over nitrite, the predominant CcNiR species has only a small fraction of the heme pool reduced. One possibility is that this observation is an artifact of the experimental method being used (bulk electrolysis is not an ideal tool for investigating catalytic

reactions because mass transport can play a major role). However, the observation may yet prove to have physiological significance.

## 2.5 References

- 1 Mowat, C. G. & Chapman, S. J. Multi-heme cytochromes - new structures, new chemistry. *J. Chem. Soc. Dalton Trans.* **21**, 3381-3389 (2005).
- 2 Bewley, K. D., Ellis, K. E., Firer-Sherwood, M. A. & Elliott, S. J. Multi-heme proteins: nature's electronic multi-purpose tool. *Biochim. Biophys Acta* **1827**, 938-948 (2013).
- 3 Youngblut, M. *et al.* Shewanella oneidensis Cytochrome c Nitrite Reductase (ccNiR) Does Not Disproportionate Hydroxylamine to Ammonia and Nitrite, Despite a Strongly Favorable Driving Force. *Biochemistry* **53**, 2136-2144, doi:10.1021/bi401705d (2014).
- 4 Youngblut, M. *et al.* Laue crystal structure of Shewanella oneidensis cytochrome c nitrite reductase from a high-yield expression system. *JBIC* **17**, 647-662, doi:10.1007/s00775-012-0885-0 (2012).
- 5 Kostera, J., McGarry, J. M. & Pacheco, A. A. Enzymatic Interconversion of Ammonia and Nitrite: the Right Tool for the Job. *Biochemistry* **49**, 8546-8553 (2010).
- 6 Kostera, J., Youngblut, M. D., Slosarczyk, J. M. & Pacheco, A. A. Kinetic and product distribution analysis of NO reductase activity in *Nitrosomonas europaea* hydroxylamine oxidoreductase. *J. Biol. Inorg. Chem.* **13**, 1073-1083, doi:10.1007/s00775-008-0393-4 (2008).
- 7 Homer, R. F. & Tomlinson, T. E. The stereochemistry of the bridged quaternary salts of 2,2'-bipyridyl. *J. Chem. Soc.*, 2498-2503 (1960).
- 8 Judd, E. T., Youngblut, M., Pacheco, A. A. & Elliott, S. J. Direct Electrochemistry of Shewanella oneidensis Cytochrome c Nitrite Reductase: Evidence of Interactions across the Dimeric Interface. *Biochemistry* **51**, 10175-10185, doi:10.1021/bi3011708 (2012).
- 9 Heineman, W. R., Norris, B. J. & Goelz, J. F. Measurement of enzyme  $E^0$  values by optically transparent thin layer electrochemical cells. *Anal. Chem.* **47**, 79-84 (1975).
- 10 Pilkington, M. B. G., Coles, B. A. & Compton, R. G. Construction of an optically transparent thin layer electrode cell for use with oxygen-sensitive species in aqueous and non-aqueous solvents. *Anal. Chem.* **61**, 1787-1789 (1989).
- 11 Watanabe, T. & Honda, K. Measurement of the extinction coefficient of the methyl viologen cation radical and the efficiency of its formation by semiconductor photocatalysis. *J. Phys. Chem.* **86**, 2617-2619 (1982).

- 12 Bamford, V. A. *et al.* Structure and spectroscopy of the periplasmic cytochrome c nitrite reductase from *Escherichia coli*. *Biochemistry* **41**, 2921-2931 (2002).
- 13 Hendrich, M. P. & Debrunner, P. G. Integer-spin electron paramagnetic resonance of iron proteins. *Biophysical Journal* **56**, 489-506, doi:10.1016/s0006-3495(89)82696-7 (1989).
- 14 Rutter, R. *et al.* Chloroperoxidase compound I: electron paramagnetic resonance and Moessbauer studies. *Biochemistry* **23**, 6809-6816, doi:10.1021/bi00321a082 (1984).
- 15 Bertini, I., Luchinat, C., Parigi, G. & Walker, F. A. Heme methyl <sup>1</sup>H chemical shifts as structural parameters in some low-spin ferriheme proteins. *JBIC* **4**, 515-519, doi:10.1007/s007750050337 (1999).
- 16 Shokhirev, N. V. & Walker, F. A. Co- and Counterrotation of Magnetic Axes and Axial Ligands in Low-Spin Ferriheme Systems. *Journal of the American Chemical Society* **120**, 981-990, doi:10.1021/ja972265s (1998).
- 17 Li, J., Noll, B. C., Schultz, C. E. & Scheidt, W. R. New insights on the electronic and molecular structure of cyanide-ligated iron(III) porphyrinates. *Inorg. Chem.* **46**, 2286-2298 (2007).
- 18 Press, W. H., Teukolsky, S. A., Vetterling, W. T. & Flannery, B. P. 65-75 (Cambridge University Press, 2007).
- 19 Henry, E. R. & Hofrichter, J. in *Meth. Enzymol.* Vol. 210 (eds L. Brand & M. L Johnson) 129-192 (Academic Press, 1992).
- 20 Walker, F. A. Magnetic spectroscopic (EPR, ESEEM, Mossbauer, MCD and NMR) studies of low-spin ferriheme centers nad their corresponding heme proteins. *Coord. Chem. Rev.* **186**, 471-534 (1999).
- 21 Westcott, B. L. & Enemark, J. H. in *Inorganic Electronic Structure and Spectroscopy* Vol. 2 (eds E. I. Solomon & A. B. P. Lever) Ch. 7, 435-439 (John Wiley and Sons, Inc., 1999).
- 22 Nasri, H., Ellison, M. K., Chen, S., Huynh, B. H. & Scheidt, W. R. Sharing the p-bonding. An iron porphyrin derivative with trans p-accepting axial ligands. Synthesis, EPR and Mossbauer spectra, and molecular structure of two forms of the complex nitronitrosyl(a,a,a,a-tetrakis(*o*-pivalamidophenyl)-porphinato)ferrate(II). *J. Am. Chem. Soc.* **119**, 6274-6283 (1997).
- 23 Wayland, B. B. & Olson, L. W. Spectroscopic studies and bonding model for nitric oxide complexes of iron porphyrins. *J. Am. Chem. Soc.* **96**, 6037-6041 (1974).
- 24 Einsle, O. *et al.* Cytochrome c Nitrite Reductase from *Wolinella succinogenes*: Structure at 1.6 a resolution, inhibitor binding, and heme-

- packing motifs. *Journal of Biological Chemistry* **275**, 39608-39616, doi:10.1074/jbc.M006188200 (2000).
- 25 Hendrich, M. P., Upadhyay, A. K., Riga, J., Arciero, D. M. & Hooper, A. B. Spectroscopic characterization of the NO adduct of hydroxylamine oxidoreductase. *Biochemistry* **41**, 4603-4611 (2002).
- 26 Enemark, J. H. & Feltham, R. D. Principles of Structure, Bonding and Reactivity for Metal Nitrosyl Complexes. *Coord. Chem. Rev.* **13**, 339-406 (1974).
- 27 Solomon, E. I. & Hanson, M. A. in *Inorganic Electronic Structure and Spectroscopy* Vol. 2 (eds E. I. Solomon & A. B. P. Lever) Ch. 1, 54-59 (John Wiley and Sons, Inc., 1999).
- 28 Upadhyay, A. K., Hooper, A. B. & Hendrich, M. P. NO reductase activity of the tetraheme cytochrome C554 of *Nitrosomonas europaea*. *Journal of the American Chemical Society* **128**, 4330-4337, doi:10.1021/ja055183+ (2006).
- 29 Einsle, O., Messerschmidt, A., Huber, R., Kroneck, P. M. H. & Neese, F. Mechanism of the six-electron reduction of nitrite to ammonia by cytochrome c nitrite reductase. *J. Am. Chem. Soc.* **124**, 11737-11745, doi:10.1021/Ja0206487 (2002).
- 30 Martins, G. *et al.* Substrate binding to a nitrite reductase induces a spin transition. *J. Phys. Chem. B.* **114**, 5563-5566 (2010).
- 31 Cheesman, M. R., Oganessian, V. S., Watmough, N. J., Butler, C. S. & Thomson, A. J. The nature of the exchange coupling between high-spin Fe(III) heme  $o_3$  and  $Cu_B$ (II) in *Escherichia coli* quinol oxidase, cytochrome  $bo_3$ : MCD and EPR studies. *J. Am. Chem. Soc.* **126**, 4157-4166 (2004).
- 32 Clarke, T. A. *et al.* Role of a conserved glutamine residue in tuning the catalytic activity of *Escherichia coli* Cytochrome c nitrite reductase. *Biochemistry* **47**, 3789-3799 (2008).
- 33 Gwyer, J. D., Richardson, D. J. & Butt, J. N. Resolving the complexity in the interactions of redox enzymes and their inhibitors: contrasting mechanisms for the inhibition of a cytochrome c nitrite reductase revealed by protein film voltammetry. *Biochemistry* **43**, 15086-15094 (2004).
- 34 Rodrigues, M., Oliveira, T., Pereira, I. & Archer, M. X-ray structure of the membrane-bound cytochrome c quinol dehydrogenase NrfH reveals novel haem coordination. *EMBO Journal* **25**, 5951-5960 (2006).
- 35 Marritt, S. J. *et al.* Spectroelectrochemical Characterization of a Pentaheme Cytochrome in Solution and as Electrocatalytically Active Films on Nanocrystalline Metal-Oxide Electrodes. *Journal of the American Chemical Society* **130**, 8588-8589, doi:10.1021/ja802641a (2008).

- 36 Rivera, M. *et al.* The reduction potential of cytochrome b(5) is modulated by its exposed heme edge. *Biochemistry* **37**, 1485-1494 (1998).
- 37 Wirtz, M., Oganessian, V., Zhang, X. J., Studer, J. & Rivera, M. Modulation of redox potential in electron transfer proteins: Effects of complex formation on the active site microenvironment of cytochrome b(5). *Faraday Discussions*, 221-234 (2000).
- 38 Pereira, I., LeGall, J., Xavier, A. & Teixeira, M. Characterization of a heme *c* nitrite reductase from a non-ammonifying microorganism, *Desulfovibrio vulgaris* Hildenborough. *Biochim. Biophys. Acta* **1481**, 119-130 (2000).
- 39 Igarashi, N., Moriyama, H., Fujiwara, T., Fukumori, Y. & Tanaka, N. The 2.8 Å structure of hydroxylamine oxidoreductase from a nitrifying chemoautotrophic bacterium, *Nitrosomonas europaea*. *Nature structural biology* **4**, 276-284 (1997).
- 40 Youngblut, M. *et al.* Laue crystal structure of *Shewanella oneidensis* cytochrome *c* nitrite reductase from a high-yield expression system. *J. Biol. Inorg. Chem.* **17**, 647-662 (2012).
- 41 Kurnikov, I. V., Ratner, M. A. & Pacheco, A. A. Redox equilibria in hydroxylamine oxidoreductase. Electrostatic control of electron redistribution in multielectron oxidative processes. *Biochemistry* **44**, 1856-1863, doi:10.1021/Bi048060v (2005).
- 42 Collins, M. J., Arciero, D. M. & Hooper, A. B. Optical Spectropotentiometric Resolution of the Hemes of Hydroxylamine Oxidoreductase - Heme Quantitation and Ph-Dependence of  $E_m$ . *J. Biol. Chem.* **268**, 14655-14662 (1993).
- 43 Hendrich, M. P., Petasis, D., Arciero, D. M. & Hooper, A. B. Correlations of structure and electronic properties from EPR spectroscopy of hydroxylamine oxidoreductase. *J. Am. Chem. Soc.* **123**, 2997-3005 (2001).
- 44 Costa, C. *et al.* Hexaheme nitrite reductase from *Desulfovibrio desulfuricans*. *J. Biol. Chem.* **265**, 14382-14387 (1990).
- 45 Hoshino, M., Ozawa, K., Seki, H. & Ford, P. C. Photochemistry of Nitric-Oxide Adducts of Water-Soluble Iron(III) Porphyrin and Ferrihemoproteins Studied by Nanosecond Laser Photolysis. *J. Am. Chem. Soc.* **115**, 9568-9575 (1993).
- 46 Bohle, S. D. & Hung, C.-H. Ligand-promoted rapid nitric oxide dissociation from ferrous porphyrin nitrosyls. *J. Am. Chem. Soc.* **117**, 9584-9585 (1995).
- 47 Ellison, M. K. & Scheidt, W. R. Synthesis, molecular structures, and properties of six-coordinate  $[\text{Fe}(\text{OEP})(\text{L})(\text{NO})]^+$  derivatives: Elusive nitrosyl ferric porphyrins. *J. Am. Chem. Soc.* **121**, 5210-5219 (1999).

- 48 Ford, P. C. & Lorkovic, I. M. Mechanistic aspects of the reactions of nitric oxide with transition-metal complexes. *Chem. Rev.* **102**, 993-1017, doi:10.1021/Cr0000271 (2002).
- 49 Bykov, D. & Neese, F. Substrate binding and activation in the active site of cytochrome *c* nitrite reductase: a density functional study. *J. Biol. Inorg. Chem* **16**, 417-430 (2011).
- 50 Bykov, D. & Neese, F. Reductive activation of the heme iron-nitrosyl intermediate in the reaction mechanism of cytochrome *c* nitrite reductase: a theoretical study. *J. Biol. Inorg. Chem.* **17**, 741-760 (2012).

## 3 Nitrite and sulfate binding to CcNiR

### 3.1 Background

In Chapter 2 EPR titrations of CcNiR with nitrite and cyanide were described. Two distinct spectroscopic events were observed as the ligand concentrations were varied. However, only a few points were taken at the lower ligand concentrations. The initial objective for the nitrite titrations reported here was to get more points at the lower concentrations of ligand in order to determine a  $K_d$ . However, a small change in the CcNiR purification method relative to that used in the previous experiments<sup>1-3</sup> had an unexpected effect on the results. Previously, an FPLC hydrophobic interaction column was used for the final step, in which the protein was loaded onto the column in a buffer containing 2M ammonium sulfate, and then eluted with a decreasing gradient of the salt. CcNiR elutes somewhere in the middle of the gradient, and consequently the eluant still contains approximately 1M ammonium sulfate. The ultimate concentration of residual ammonium sulfate depended on how thoroughly the buffer was exchanged before the sample of the pure protein was stored. Recently, Dan Pauly of the Pacheco group developed a new preparation of the enzyme, in which the final HIC step was replaced with cation exchange. This alteration excluded any sulfate in the final preparation. As reported in this chapter differences in sulfate concentration resulted in notable changes in the CcNiR EPR spectra, and even detectable changes to the UV/Vis spectra.

## 3.2 Methods

### 3.2.1 Purification

The CcNiR protein was purified as described in Youngblut *et al.*<sup>3</sup> up to the point where the flow-through from the Q anion exchange column was collected. At that point the flow-through was exchanged into 25 mM HEPES free acid adjusted to pH = 6.5 and 1 mM EDTA from Fisher and Sigma respectively, and loaded onto a 5 mL SP cation exchange column from GE that was pre-equilibrated with the same buffer. After loading, a 50 mL gradient was set with an elution buffer B consisting of 25 mM HEPES free acid adjusted to pH = 7.0 and 1 mM EDTA. CcNiR eluted at the very end of that gradient. All the fractions containing heme were collected and exchanged once into buffer B, before storing at  $-80\text{ }^{\circ}\text{C}$  as a sample labeled NS\_798i.

### 3.2.2 Sulfate titrations

Sixteen microliters of NS\_798i was diluted in 4mL of 25mM HEPES pH=7.0 to give a 1.8  $\mu\text{M}$  solution of CcNiR (protomer concentration) with  $A_{410} \sim 1$ . This mixture was used for the subsequent titrations. Ten mL of 0.98 M sulfate was prepared when 2.436g of  $\text{MgSO}_4 \cdot 7\text{H}_2\text{O}$  from Sigma was dissolved in 10 mL 25mM HEPES pH = 7.0. This solution was diluted to make the 0.1 M and 0.5 M stock solutions for each titration. A Cary 50 UV-Vis spectrophotometer was used to collect UV-Vis scans. A 2 mL cuvette with 1cm pathlength containing 1 mL of 25mM HEPES pH=7.0 was used to blank the instrument. For each titration a spectrum of 1mL of the 1.8  $\mu\text{M}$  CcNiR solution in the same cuvette was first

obtained in the absence of added sulfate. Subsequently one-microliter aliquots of the particular sulfate stock solution (see results) were added, and the mixture homogenized by pipetting up and down with a Pasteur pipet. A scan was taken following each addition, and the final concentration of sulfate was calculated using equation 3.1.

**Equation 3.1**  $n$  is the total number of microliters of the sulfate stock added to the initial 1mL solution of CcNiR.

$$\frac{n \cdot 10^{-6} \cdot [SO_4^-]_{stock}}{0.001 + n \cdot 10^{-6}} = [SO_4^-]_{final}$$

Difference spectra were calculated by subtracting the initial spectrum without sulfate from each subsequent one. The difference spectra were analyzed for the number of components using the Mathcad15 built-in SVD subroutine. The procedure was also used to remove noise. After SVD analysis an absorbance vs concentration slice of the clean spectra was obtained at 411 nm, where the spectral change is most profound, and fit to equation 3.2 to obtain the dissociation constant.

**Equation 3.2**  $\Delta A$  is the change in absorbance at 411 nm,  $\Delta A_{max}$  is the maximum change in absorbance at 411 nm, and  $K_d$  is the dissociation constant.

$$\Delta A = \frac{\Delta A_{max} \cdot [SO_4^-]}{K_d + [SO_4^-]}$$

### 3.2.3 Nitrite titration (EPR) of sulfate free CcNiR solution

The samples were prepared with the same CcNiR, NS\_798i stock as was used for UV-vis sulfate titrations. A solution of 25 $\mu$ M dimer in 25mM HEPES pH=7.0 was used in each titration while varying the concentration of nitrite. A

blank sample was prepared with the buffer. The TEleXsys E600 EPR spectrometer (Bruker) was set at 9.63GHz, with microwave power of 12.60 mW; the modulation amplitude was 1 Gauss, and the temperature was 10K during all observations.

### **3.3 Results**

#### 3.3.1 Sulfate titrations monitored by UV-Vis

Figure 3.1 shows the UV/Vis spectral changes that accompany titration of CcNiR with sulfate. SVD analysis and the presence of isosbestic points at 350 and 460nm reveal a single spectral change in the Soret region. The most profound change occurs at 411nm, with another significant change also seen at 310nm. The change in absorbance at 411 nm as a function of sulfate concentration is shown in Figure 3.2. That plot was used to extract  $K_d$  using Eq. 3.2. The calculated  $K_d$  value of 2.87 mM shows that 90% of available sites on CcNiR are occupied by sulfate when the total sulfate concentration is 20 mM.

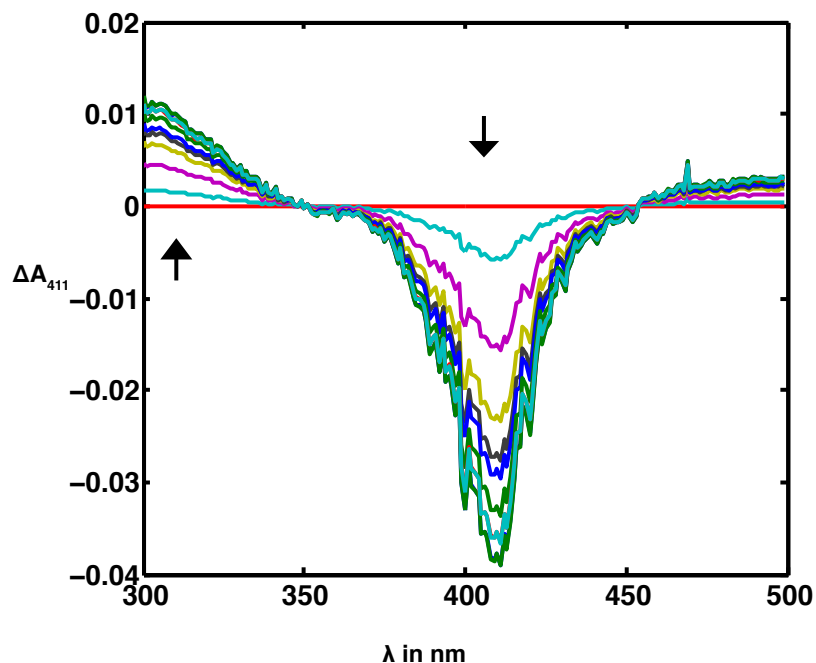


Figure 3.1 Difference UV-Vis spectra of CcNiR titrated with sulfate. Arrows indicate the direction of change. The most profound change is at 411 nm. While not as profound, a second change in absorbance can be seen at 310nm. Two isosbestic points are seen at 350 and 460 nm.

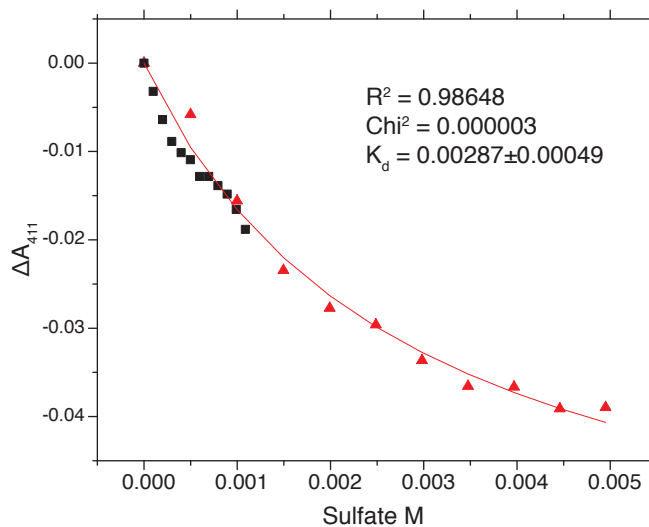
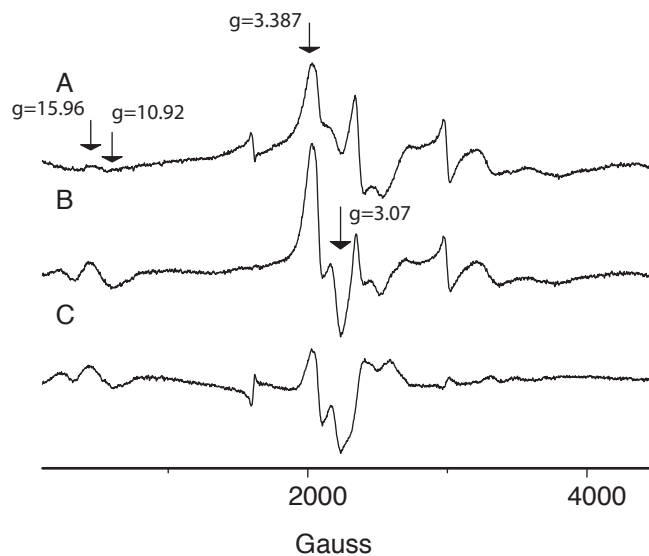


Figure 3.2 Change in absorbance at 411 nm with respect to sulfate concentration. The black squares and red triangles are titration points with 0.1 M with 0.5 M sulfate respectively. The red line is the fit of the data to equation 2, which yielded optimized parameters  $K_d = 2.87$  mM and  $\Delta A_{\max} = -0.05$ .

### 3.3.2 Nitrite titrations of sulfate free CcNiR monitored by EPR

An EPR spectrum of resting CcNiR is illustrated in Figure 3.3A. Addition of up to 100  $\mu\text{M}$  nitrite contributes to the increase of signals with derivative maxima and minima at  $g=3.87$  and  $3.07$ , and  $g= 16$  and  $11$  (Figure 3.3 B). The difference between the spectra obtained in the presence and absence of added sulfate is illustrated in Figure 3.3C. The stepwise changes in these signals' intensities, estimated from the difference between the maxima and minima of the derivative  $g$ -values, are illustrated in Figure 3.4. The low magnetic field signal ( $g' = 16$  and  $11$ ) increased approximately ten times. The signal at around 2000 gauss increased to twice its original intensity. All intensities remain approximately constant between 100 and 150  $\mu\text{M}$  nitrite. Both signals declined in what appears to be a sigmoidal fashion at higher concentration of nitrite until they disappear by 1 mM nitrite. At that point the spectrum has the same overall appearance as the spectra obtained in the presence of nitrite or cyanide *and* sulfate (Figure 2.4 in Chapter 2).



**Figure 3.3 (A) EPR spectrum of resting CcNiR. (B) EPR spectrum of CcNiR in the presence of 50  $\mu$ M nitrite. (C) Difference between A and B.**

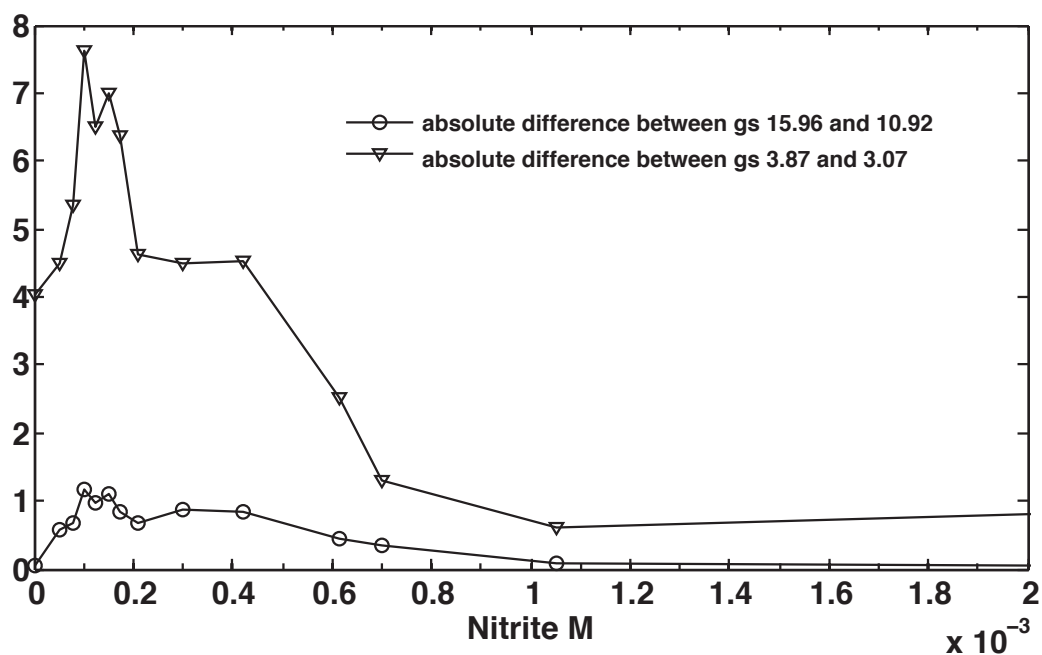


**Figure 3.4 Net differences between g values as indicated in text and in Figure 3.5 below.**

The changes in X-band EPR spectra of CcNiR produced by the increased concentrations of nitrite are due to nitrite binding to the five-coordinate active site heme. As discussed in Chapter 2, the coupling between this high-spin heme and

its neighbors, hemes 3 and 4, complicates the EPR signal. However, the spectral changes seen in figure 3.5, using a CcNiR sample that was rigorously sulfate-free, are quite different from those seen when nitrite was added to CcNiR containing unspecified amounts of sulfate figure 3.6

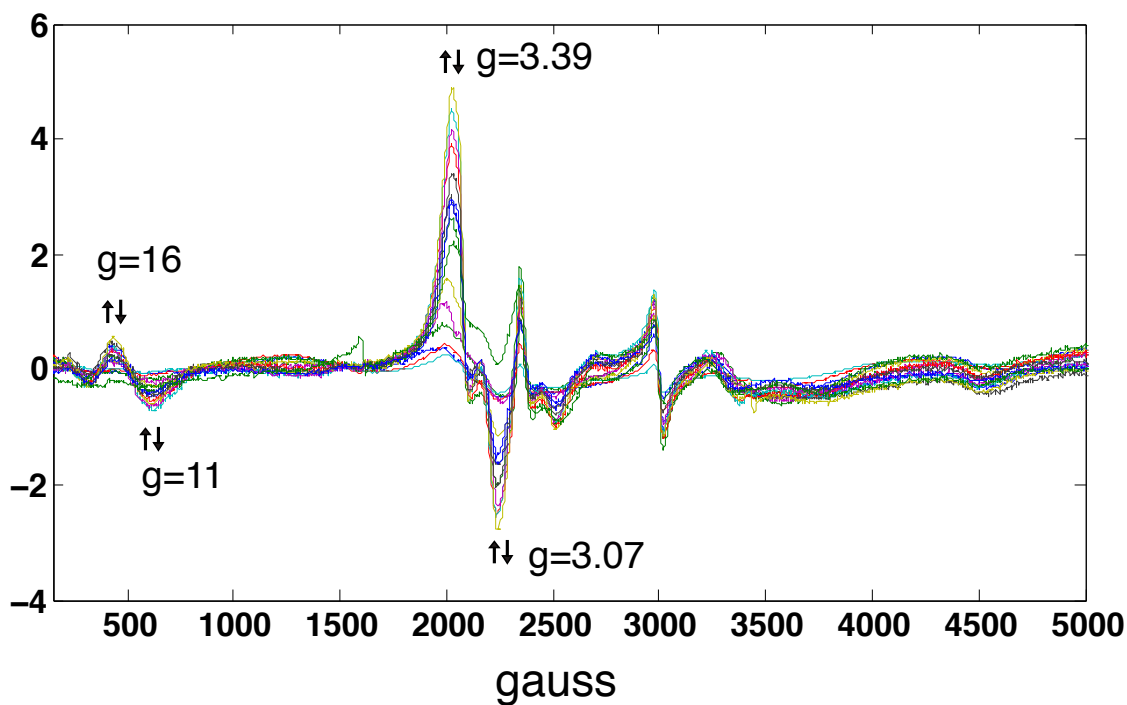


**Figure 3.5** The overlaid spectra conveys the entire titration of sulfate free CcNiR. The up and down arrows indicate the g values that increase and subsequently decrease as the concentration of nitrite increases (see Figure 3.4).

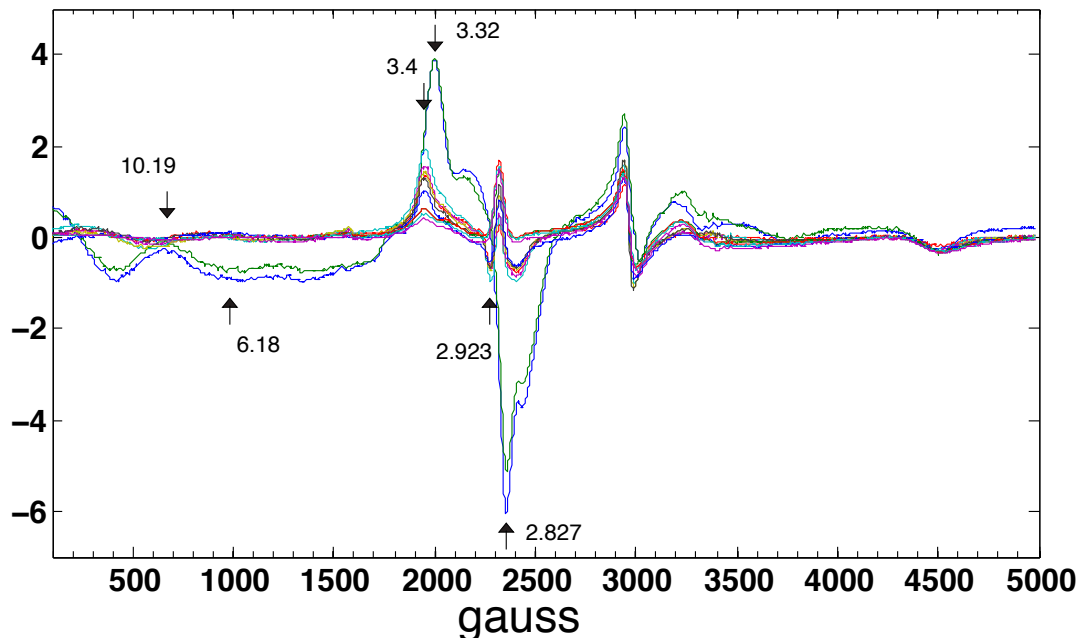


**Figure 3.6** The overlaid spectra of sulfate-containing CcNiR solutions as they are titrated with nitrite from Chapter 2 replotted here for convenience. The arrows indicate the g-values. The notable difference between these and the spectra in Figure 3.5 is that here only two distinct, decreasing signals observed and not intermediates.

Figure 3.7 shows the distances and the potential ways for coupling between hemes 1, 3 and 4. The potentiometric titrations in Chapter 2 demonstrated that hemes 3 and 4 are coupled in bound and unbound enzyme, since reduction of heme 4 decouples the signal of heme 3. It is unclear whether heme 1 can also interact with heme 4 through the imidazole that axially ligates heme 3. Due to the plethora of coupling possibilities, and asymmetry of CcNiR dimer as discussed below, attempts to simulate these spectra have not been successful to date.

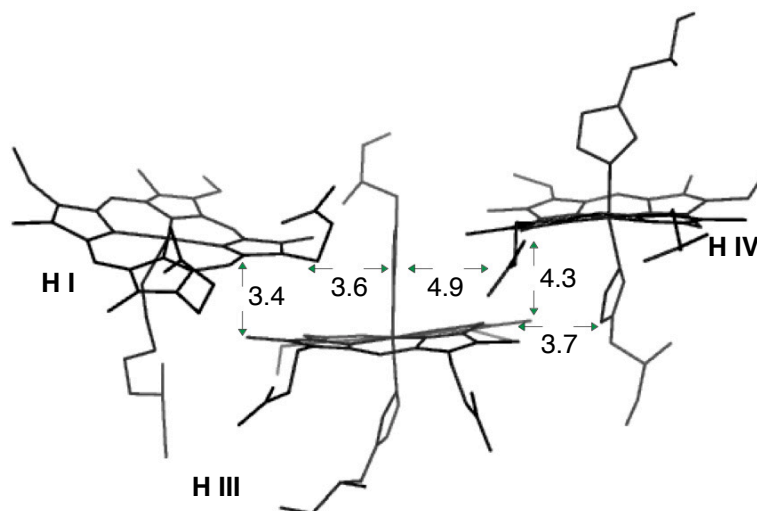


**Figure 3.7** The edge-to-edge distances between hemes, and select imidazole rings of the axial histidine ligands, for hemes 1, 3 and 4 of CcNiR.

### 3.4 Discussion

A possible model for binding of nitrite to oxidized CcNiR, that explains the intermediate signal at low magnetic field and at  $g = 3.87$  and  $3.07$ , is illustrated in Figure 3.8. When the distal pocket of the active site heme is vacant, the enzyme can exist in two states: in state 1 hemes 1, 3, and 4 are coupled in a way that doesn't give rise to a low magnetic field transition, while in state 2 the coupling is such that a low magnetic field signal *is* observed. Upon binding of nitrite to the active site in either state 1 or 2, the bound site will switch to state 3, in which the active site, heme 1, is low spin and appears as a broad HALS signal. In state 3 hemes 3 and 4 are coupled so that they are EPR silent (See Chapter 2). In addition, whenever a nitrite molecule binds to the one protomer's active site, if the active site on the adjacent protomer is vacant, it will switch to state 2. Hence,

state two is observed to increase in concentration, and then to decrease as the enzyme is saturated with nitrite and all the sites convert to state 3.

Sulfate is known to bind to CcNiRs from other species as a weak competitive inhibitor<sup>4,5</sup>. This consideration was overlooked in the initial study (Chapter 2), where two independent events were being inadvertently observed, as illustrated in Figure 3.8. A signal with maxima and minima at  $g=3.329$  and  $2.827$  that correlates with a low magnetic field signal with maxima and minima at  $g=10.2$  and  $g=6.18$ , disappears after addition of approximately  $200\mu\text{M}$  nitrite. The other signal with maxima and minima at  $g=3.4$  and  $2.923$  is titrated away at approximately  $2\text{mM}$  nitrite. Given that sulfate is a weak-field ligand, the sulfate-bound active site should be stabilized in a high-spin state. Higher nitrite concentration needed to reach the titration end point in the presence of sulfate ( $\sim 2\text{mM}$  in Chapter 2 versus  $1\text{mM}$  in this report), can be explained by sulfate acting as a competitive ligand that stabilizes the high-spin form.

Given that binding of a ligand to the active site of one protomer elicits changes in the active site of the adjacent protomer, it is unlikely that the binding and catalysis at the adjacent site would remain unaffected in the presence of sulfate. A logical question to ask would be how sulfate binding at one site might affect binding and catalysis at the second site? Sulfate is competitive inhibitor, but is it also an *allosteric* inhibitor or activator? This is an interesting question that should be addressed in future studies.

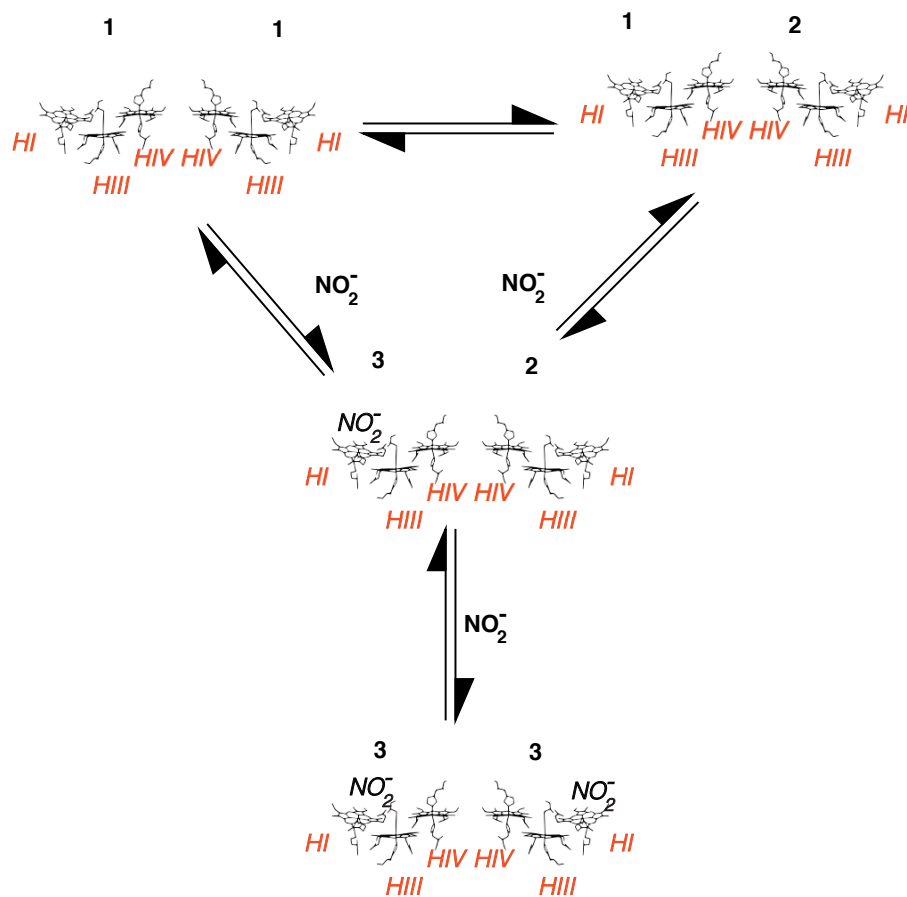


Figure 3.8 Illustration of the possible state changes that CcNiR dimer may undergo as it saturates with nitrite.

### 3.5 References

- 1 Youngblut, M. *et al.* *Shewanella oneidensis* Cytochrome c Nitrite Reductase (CcNiR) Does Not Disproportionate Hydroxylamine to Ammonia and Nitrite, Despite a Strongly Favorable Driving Force. *Biochemistry* **53**, 2136-2144, doi:10.1021/bi401705d (2014).
- 2 Judd, E. T., Youngblut, M., Pacheco, A. A. & Elliott, S. J. Direct Electrochemistry of *Shewanella oneidensis* Cytochrome c Nitrite Reductase: Evidence of Interactions across the Dimeric Interface. *Biochemistry* **51**, 10175-10185, doi:10.1021/bi3011708 (2012).
- 3 Youngblut, M. *et al.* Laue crystal structure of *Shewanella oneidensis* cytochrome c nitrite reductase from a high-yield expression system. *JBIC* **17**, 647-662, doi:10.1007/s00775-012-0885-0 (2012).
- 4 Einsle, O. *et al.* Structure of cytochrome c nitrite reductase. *Nature* **400**, 476-480, doi:10.1038/22802 (1999).
- 5 Einsle, O. *et al.* Cytochrome c Nitrite Reductase from *Wolinella succinogenes*: Structure at 1.6 Å resolution, inhibitor binding, and heme-packing motifs. *Journal of Biological Chemistry* **275**, 39608-39616, doi:10.1074/jbc.M006188200 (2000).

## 4 Octaheme tetrathionate reductase

### 4.1 Background

Octaheme Tetrathionate Reductase (OTR) from *Shewanella Oneidensis* is coded by locus SO4144. It was first over-expressed and purified by Chapman et al. <sup>1,2</sup>. The crystal structure was solved and revealed an octaheme protein with seven bis-histidine ligated six-coordinate hemes, and one lysine-ligated five-coordinate heme. The arrangement of hemes resembles those found in Cytochrome C Nitrite Reductases (CcNiRs) and Hydroxylamine Oxidoreductases (HAOs). While no specific biological role was assigned to OTR, the protein was reported to catalyze nitrite and hydroxylamine reduction to ammonia, and interconversion of tetrathionate and thiosulfate <sup>3</sup>. When our group first started to work on *S. oneidensis* CcNiR the structure of this enzyme was unavailable, whereas that of *S. oneidensis* OTR had already been solved. This, coupled to the fact that OTR is a monomer whereas CcNiR is a dimer, made attractive a comparative study of the nitrite and hydroxylamine reductase activities of the two enzymes. This chapter describes the optimization of an OTR expression system, and partial purification and characterization of the enzyme

#### 4.1.1 Subcloning and expression

The plasmid pMMB503EH, illustrated in Figure 4.1, is a broad host shuttle vector that was previously used for OTR expression <sup>1,3</sup>. Genscript synthesized the gene sequence for OTR with the optimized codons for *E. coli* expression. In

this gene the OTR leader peptide sequence and ribosomal binding site were replaced with those of SO\_2727 small tetraheme-c (STC), a strategy previously found to be very efficient for the expression of CcNiR in *S. oneidensis* species<sup>4</sup>. The OTR gene was supplied in a pUC18 vector, and was made excisable with EcoRI/PstI endonucleases. pMMB503EH was purified out of NEB5 $\alpha$  cells using a Five Prime maxi prep kit from Fisher. The Genscript OTR construct and pMMB503EH were over-digested with EcoRI/PstI enzymes supplied by New England Biolabs (NEB). The fragment that corresponded to 1400bp (the length of OTR gene sequence) was separated from pUC18 on a 1% agarose Tris Acetic acid EDTA (TAE) gel. The fragment was excised and purified using a QIAquick Gel Extraction Kit from Qiagen. QAIEXII from Qiagen was used to separate the digested pMMB503EH from the small polylinker region fragment generated by the over-digestion. The QIAquick Gel Extraction kit and other column based kits proved ineffective for purification of the large plasmid.

The digested OTR and pMMB503EH fragments were combined in 5:1 molar ratio and ligated overnight using T4 DNA ligase from Fisher Scientific. A control reaction was set up using only the double-digested pMMB503EH fragments, and completing the volume for the reaction with water instead of the OTR fragment. The next morning 5 $\mu$ L of the ligation and the control reactions were used to transform NEB5 $\alpha$  cells. The cells from the outgrowth stage were collected by a brief centrifugation in a table-top centrifuge (1 minute at 10,000 rpm). The cells were resuspended in 250 $\mu$ L SOC media each and plated on 2

LB-agar plates supplemented with streptomycin sulfate (from Fisher) at 50 $\mu$ g/mL (LB-agar<sup>strp50</sup>) each, one with 200 $\mu$ L and the other with 50 $\mu$ L the cell suspension of either ligation or control. The plates were incubated at 37°C overnight.

The colonies from the reaction plates were tested using a colony polymerase chain reaction (PCR) for the proper insert. The reactions were set up as follows:

6 $\mu$ L of nanopure water

2 $\mu$ L pMMB503EHr 5'CCGCGCTACTGCCGCCAGGC3' 10 $\mu$ M

2 $\mu$ L pMMB503EHf 5'GGCTCGTATAATGTGTGG3' 10 $\mu$ M

10 $\mu$ L of 2X Phusion PCR Mix from Fisher

a small amount of a colony introduced with a sterile pipette tip

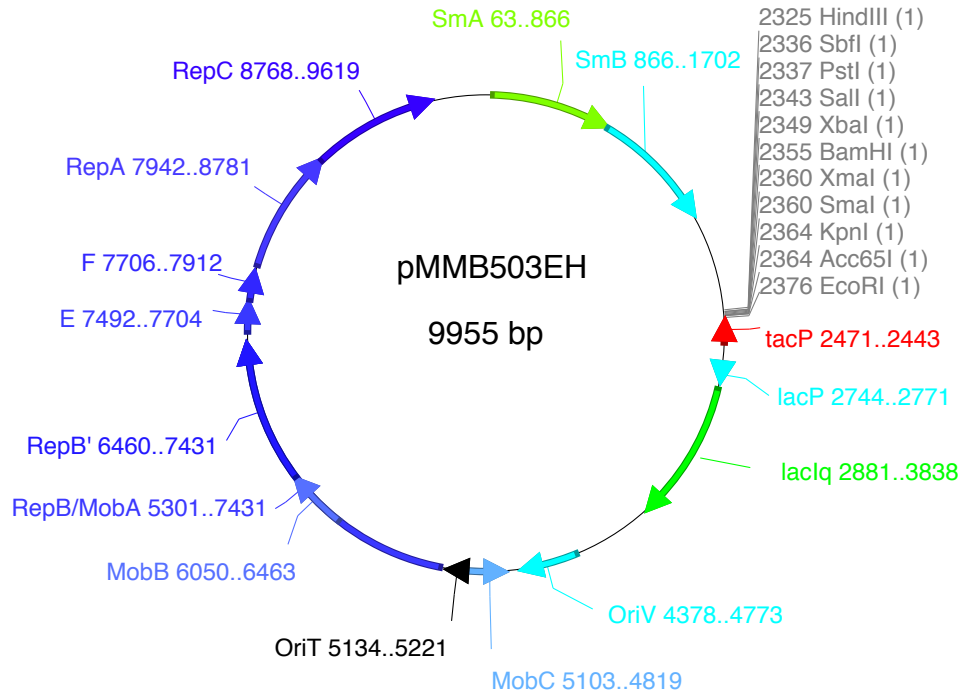
### **20 $\mu$ L total**

Figure 4.2 illustrates the cycling parameters for the PCR reactions. The products were analyzed using 1% agarose TAE gel. One of the colonies that contained the 1.4 kb band, hereafter referred to as NS\_423a, was selected for tri-parental mating.

For tri-parental mating *E. coli* E746 helper cells carrying the F plasmid with Tra genes necessary for pili construction, kindly provided by Dr. Mark McBride of the University of Wisconsin Milwaukee Biosciences Department, were grown overnight, at 37°C with agitation, in 10 mL of LB broth supplemented with 50 $\mu$ g/mL kanamycine sulfate from Fisher (LB kan<sup>50</sup>). *S. oneidensis* MR-1  $\Delta$ fccA cells, kindly provided by Dr. Daad Saffarini of the University of Wisconsin

Milwaukee Biosciences Department, were cultured in a similar manner but at 30°C. NS\_423a cells were grown following the same protocol used for the *E. coli* E746 cells, except that LB was supplemented with streptomycin sulfate at 50µg/mL instead of kanamycin. The following morning the cultures were collected by centrifugation and washed with LB broth 2 times. The three cultures were then combined and centrifuged one more time. After centrifugation the supernatant was removed, and the pellet was spotted on an LB agar plate. The plate was left to incubate right side up at 30°C for 6 hours. Following this incubation the transconjugation mixtures were streaked for isolation on LB-agar<sup>strp50/kan50</sup> plates. These plates were allowed to incubate overnight at 30°C, upside down. The following day the reddish cells were picked and re-streaked for isolation on LB-agar<sup>strp50/kan50</sup> plates. Upon confirmation that pure *Shewanella* cultures had been isolated, colony PCRs were performed as described above.

Once the identity of the successful transconjugant was confirmed, stock solutions in 20% glycerol were prepared, labeled as NS\_432f, and stored in liquid nitrogen or in a -80°C freezer.



**Figure 4.1** pMMB503EH is a broad-host range mobilize-able expression vector based on the rsf1010 plasmid<sup>5</sup>. Rep genes, together with F and E genes, act on the origin of replication OriV that allows for replication in gram negative bacteria. Mob genes act on OriT to initiate conjugative transfer; however, for successful transfer, Tra genes that encode for proteins that make pili also need to be provided. The plasmid carries resistance to streptomycin (SmA and SmB). The polycloning site that allows one to subclone the gene for expression is located downstream of the tac promoter, which is a synthetic promoter that has a higher affinity for RNA polymerase than the lac promoter. The tac promoter also contains a lac repressor region where the repressor protein lacIq suppresses gene expression in the absence of IPTG or allolactose (see main text). LacIq is expressed constitutively under the lac promoter.

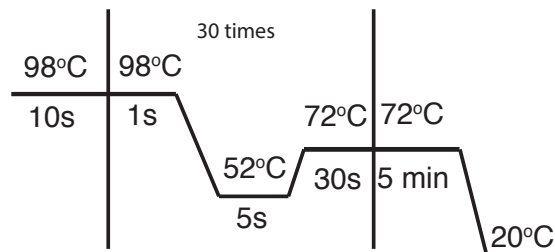


**Figure 4.2.** The PCR cycling parameters used to check for a ~1.4 kb OTR fragment in the colonies purportedly containing the OTR-pMMB503EH construct. The PCR mixture used is described in the text

#### 4.1.2 Activity assays

The activity of OTR was inferred from its ability to enhance the rate of re-oxidation of reduced methyl viologen ( $MV_{red}$ ) by a suitable oxidant/substrate (see below).  $MV_{red}$  is blue and has a molar absorptivity of  $13,600M^{-1}cm^{-1}$  at 600nm, whereas oxidized methyl viologen ( $MV_{ox}$ ) has no significant absorptivity at this wavelength. The activity was measured using a Cary 50 UV-vis spectrometer. The activity assay was performed in a glove box under a nitrogen atmosphere, with oxygen not exceeding 10ppm. A typical assay was done in a 2mL plastic cuvette with 1cm path-length, containing the following reagents in a 1 mL total volume:

970 $\mu$ L 50mM HEPES from Fisher Scientific at pH=7.0

10 $\mu$ L electrochemically reduced  $MV_{red}$ ,  $\sim 80\mu$ M final concentration

10 $\mu$ L of OTR sample (diluted to produce a readable rate)

10 $\mu$ L of electron-accepting substrate ( $\sim 10$ mM, see below)

The background rate was established prior to substrate addition, and control assays without samples were also performed to check for possible reduction of substrate without OTR present as a catalyst. Sample dilutions were chosen such that the initial rate was linear for at least 20 to 30 seconds (Figure 4.3). The midpoint potential of MV is  $-450$ mV versus SHE. When reduced, it is a strong reducing agent capable of transferring electrons to an oxidizing substrate via OTR. Three molecules that were identified as electron-accepting substrates in previous publications were tested: nitrite, hydroxylamine and tetrathionate<sup>3</sup>

(Figure 4.4). The results of the assays were analyzed in units of enzymatic activity, where 1  $\mu\text{mole}$  of substrate converted per minute constitutes 1 unit of enzymatic activity (EU). Equation 4.1 describes the calculation of EU in the assay. The total EUs were calculated by taking into consideration any dilution factors and the total volume of the sample.

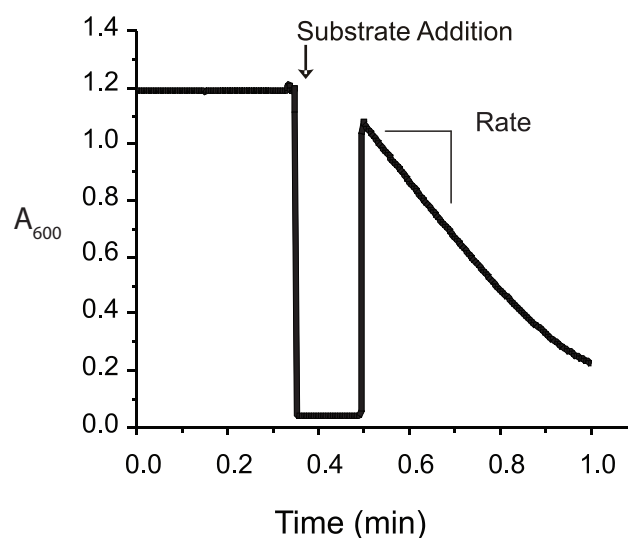


**Figure 4.3** A sample activity assay. The segment up to  $\sim 0.3$  minutes (min) is absorbance at 600nm of 50mM HEPES,  $\sim 80\mu\text{M}$   $MV_{\text{red}}$  and OTR prior to addition of oxidizing substrate. The latter is added at the time shown by the downward arrow. The dip in absorbance is due to lifting of the cuvette during sample mixing. The initial rate is taken from the slope of the linear portion of the trace that follows substrate addition.

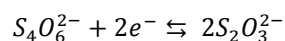
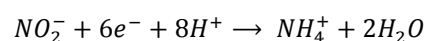


**Figure 4.4** Balanced chemical equations for reactions reported for OTR in previous publications <sup>3</sup>.

**Equation 4.1**  $AU_{600}/\text{min}$  is the change in absorbance per minute.  $13600 \text{ (M}^{-1}\text{cm}^{-1}\text{)}$  is the  $MV_{\text{red}}$  extinction coefficient.  $0.001\text{L}$  is the volume of the assay.  $\#e^{-}$  stands for number of electrons transferred in order to reduce the substrate to product.  $\mu\text{moles}/\text{min}$  are the EU in the assay.

$$\frac{AU_{600} \times 10^6}{\text{min} \times 13600 \times 0.001\text{L} \times \#e^{-}} = \frac{\mu\text{moles}}{\text{min}}$$

#### 4.1.3 Optimization of OTR expression

An overnight starter culture inoculated with a few shavings of NS\_432f permanent stock was grown on  $20\text{mL LB}^{\text{kan}50/\text{strp}50}$  in a  $100\text{mL}$  culture flask overnight with agitation at  $30^{\circ}\text{C}$ . The following morning  $10\text{ mL}$  aliquots of the starter culture were added to each of two  $2\text{L}$ -flasks, each containing  $1\text{L LB}^{\text{kan}50/\text{strp}50}$ . The flasks were placed in the shaking incubator at  $30^{\circ}\text{C}$ , and the observed density at  $600\text{nm}$  ( $OD_{600}$ ) was monitored. Once it reached 1, one flask was induced with  $100\ \mu\text{M}$  (final concentration) of Isopropyl  $\beta$ -D-1-thiogalactopyranoside (IPTG) from Fisher Scientific. This compound is a non-metabolizable analogue of allolactose that removes repressor protein from the operator region on pMMB503EH, and opens the promoter for RNA polymerase. Subsamples of  $100\text{mL}$  were taken from each flask at regular time intervals as indicated in the results section, and the cells were collected by centrifugation. The cell pellets were re-suspended in  $25\text{mL}$  of  $25\text{mM HEPES pH}=7.5$ , containing  $1\text{mM EDTA}$  and a protease inhibitor cocktail, and sonicated on ice for 15 minutes in 30 second bursts with 45 seconds cool down periods to ensure that solution temperatures did not exceed  $5^{\circ}\text{C}$ . Sonic waves are destructive to the cellular membrane, and even to such polymeric molecules as DNA. Insoluble cell debris

was removed by centrifugation at 30,600 **g**, 4°C for 30 min. The supernatant was used in the activity assays where tetrathionate, nitrite and hydroxylamine were substrates, and in further purification steps described below.

#### 4.1.4 Streptomycin sulfate additions

Streptomycin sulfate (Fisher) from a concentrated stock in nanopure water was added dropwise to the ice-cooled, slowly stirred supernatant from the sonication lysate, until the desired weight over volume concentrations specified in the results section were attained. Streptomycin is a positively charged molecule that is known to bind nucleic acids, and it will precipitate genomic DNA. Although genomic DNA is sheared by sonication, it is still a source of viscosity in the sample that complicates subsequent chromatography. The resulting precipitate was removed by centrifugation at 30,600 **g**, 4°C for 15 min. The hydroxylamine reductase assay and UV-vis absorption measurements of the  $A_{410}/A_{280}$  ratios were used to assess the effects of streptomycin on OTR present in the supernatants.

#### 4.1.5 Ammonium sulfate fractionation

The amount of ammonium sulfate (Fisher) needed for the desired concentrations was calculated using the online calculator from <http://www.encorbio.com/protocols/AM-SO4.htm>. The salt was added to the slowly stirred, ice-cooled lysate at a steady pace such that all of the ammonium sulfate was added in about 20-30 minutes. To ensure that all of the ammonium

sulfate was dissolved, and that the final mixture was homogenous, the lysate was allowed to stir for 5 minutes after all the ammonium sulfate was added.

Ammonium sulfate increases ionic strength of a solution, forcing less hydrophilic proteins (those that contain fewer charges) to aggregate together and precipitate. Precipitated proteins were pelleted by centrifugation at 30,600 g, 4°C for 15 min. The hydroxylamine reductase assay and UV-vis absorption measurements of the  $A_{410}/A_{280}$  ratios were used to assess the effects of ammonium sulfate treatment on both the supernatants and re-dissolved pellets.

#### 4.1.6 Chromatographic separation using octyl-sepharose hydrophobic interaction chromatography

Chromatography resins used in this and the following sections were purchased from GE Healthcare. A 50 mL starter culture from the frozen NS\_432f stocks, prepared as described in Section 4.2.3, was distributed evenly between four 2-L culture flasks that contained 1-L LB<sup>strp50/kan50</sup>. The flasks were incubated in a shaking incubator at 30°C. The OD<sub>600</sub> was monitored, and once it reached 1 IPTG was added to each flask to give 100µM final concentrations. The cultures were incubated for 6 more hours. The cells were collected by centrifugation at 1,000 g, 4°C for 30 minutes. The supernatant broth was removed, and the cells stored at -80°C overnight.

After fractionation with 30% ammonium sulfate as described in Section 4.2.5, the supernatant was loaded onto a 40mL octyl sepharose column that was previously equilibrated with 20mM HEPES pH=7.5, 1mM EDTA and 30%

ammonium sulfate. The column was developed with a 600mL gradient against 20mM HEPES pH=7.5, 1mM EDTA. The eluent was collected in 6mL fractions. Every ten fractions were pooled together for activity assay analysis using tetrathionate, nitrite and hydroxylamine. Chromatography using octyl sepharose is known as hydrophobic interaction chromatography (HIC) because the molecules are separated based on their hydrophobicity. It is also called reverse phase chromatography, so called because unlike conventional chromatography, where a sample binds at the low salt and elutes with high salt concentration, here the sample binds at high salt and is eluted at lower salt concentrations. Reverse phase columns are more hydrophobic than HIC columns, and are typically used for peptide and small molecule separations.

#### 4.1.7 Chromatographic separation using hydrophobic interaction, anion exchange and size exclusion columns in series

OTR from four liters of culture prepared as described in Section 4.2.6 were re-suspended in Tris-HCl pH=8.5, 1mM EDTA and protease inhibitor cocktail. The suspension was sonicated and the cell debris removed by centrifugation. Ammonium sulfate was added to the clarified lysate such that the final concentration reached 25%. The precipitate formed by the addition was removed by centrifugation as described above. The supernatant was loaded onto a 20mL butyl sepharose column that was equilibrated with Tris-HCl pH=8.5, 1mM EDTA and 25% ammonium sulfate. Once loaded, the column was washed with the equilibration buffer. Protein was eluted with Tris-HCl pH=8.5, 1mM EDTA. Butyl

sepharose is another type of HIC column. The principles for the sample separation are the same as those for octyl sepharose mentioned before. The major difference between octyl and butyl sepharose is the level of hydrophobicity; octyl sepharose is more hydrophobic due to its longer aliphatic side-chain.

The eluent from the previous column was loaded onto a 5mL Q-sepharose column that was equilibrated with Tris-HCl pH=8.5, 1mM EDTA. The column was developed with a 50mL (10 column volumes) gradient against Tris-HCl pH=8.5, 1mM EDTA and 500mM NaCl. Q-sepharose resin is used to separate proteins based on charge. The sepharose beads are decorated with the positively charged quaternary amine group. Molecules with an overall negative charge bind to the positively charged amine groups. The column is developed by a gradual increase in salt concentration, in which the negatively charged salt ions displace bound proteins.

The fractions that contained hydroxylamine reductase activity were pooled together and concentrated to 1mL. The concentrated protein was loaded onto a 475mL column packed with Sephacryl S-200 that was pre- equilibrated with 25mM Tris-HCl pH=8.5, 1mM EDTA, 100mM NaCl. S-200 is a size exclusion resin used to separate proteins by size. The porous beads make the path through the column longer for smaller molecules. The fractions that exhibited absorbance at 280nm and had hydroxylamine reductase activity were pooled. UV-vis absorbance to determine  $A_{410}/A_{280}$  were taken on a Cary 50 UV-vis in 25mM HEPES pH=7.0.

## 4.2 Results

### 4.2.1 Subcloning and expression

Plates that contained *E. coli* 5 $\alpha$  cells transformed with the pMMB503EH fragments re-ligated in the absence of the OTR gene fragment (the controls) had 3 colonies, while the plates that contained *E. coli* 5 $\alpha$  cells transformed with the pMMB503EH fragments re-ligated in the presence of the OTR gene had colonies that were too numerous to count (TNT). This suggested that the majority of ligation transformers contained the insert. Three colonies selected at random from the transformed set were subjected to colony PCR, and all confirmed the presence of the desired insert. The NS\_423a colony was selected for transconjugation.

The transconjugation plate contained numerous reddish colonies that were characteristic of *S. oneidensis*, and some smaller *E. coli* colonies that resulted from helper cells providing NS\_423a with kanamycin resistance as a result of fertility plasmid transfer. NS\_423a did not exhibit kanamycin resistance otherwise. Six of the reddish *S. oneidensis* colonies were picked for isolation and labeled as NS\_432 a-f. Of these, NS\_432f contained colonies that grew well and did not have any *E. coli* contamination. Therefore, the NS\_432f culture that carries the OTR gene on pMMB503EH (Figure 4.1) was used for all the subsequent studies.

### 4.2.2 Activity assays

Figure 4.5 shows the difference in nitrite, tetrathionate and hydroxylamine reductase activities between cultures induced with IPTG and those that were not induced. Interestingly, *no* differences in nitrite or tetrathionate reductase activities could be detected when comparing the induced and non-induced cells. On the other hand, hydroxylamine reductase activity was significantly higher in the induced cultures, with its expression reaching a maximum value 6 hours after induction (Fig. 4.5).

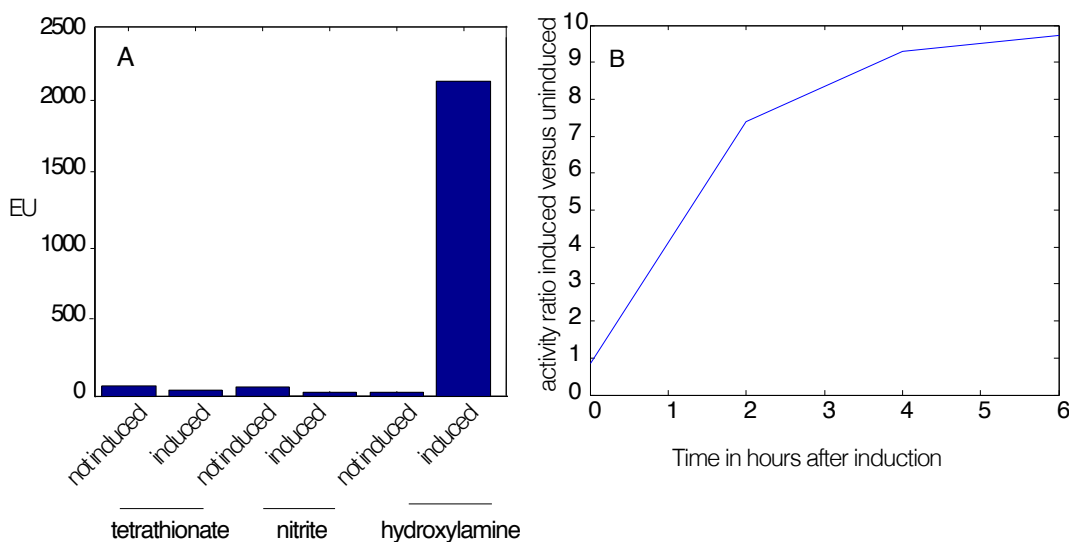


**Figure 4.5. (A) Units of enzymatic activity (EU) as described in text. The assays with the three different substrates were performed with subsamples that were collected four hours after induction with IPTG. (B) Ratios of hydroxylamine reductase activity of induced versus non-induced samples as a function of time after induction with IPTG.**

### 4.2.3 Analysis by octyl sepharose separation

The nitrite, tetrathionate and hydroxylamine reductase activities present in the soluble fractions obtained from NS\_432f were separated by chromatography on an octyl sepharose column (Figure 4.6). Notably, the activity peaks did not overlap as would be expected if they all corresponded to a single OTR enzyme as defined by Mowat and coworkers<sup>1,3</sup>. The nitrite reductase activity eluted first, followed by tetrathionate reductase activity. The hydroxylamine reductase activity eluted as two distinct peaks; the first of these overlapped the nitrite reductase activity, while the other eluted separately from the other two activities, at the very end of gradient. The hydroxylamine reductase activity that correlates with nitrite reductase activity can be attributed to the constitutively expressed Cytochrome-c Nitrite Reductase (CcNiR). Most of the hydroxylamine reductase activity eluted at the end of the gradient, and correlated with a c-heme protein that was shown to be the desired OTR species. Note though that the octaheme tetrathionate reductase activity eluting from the column did *not* correlate with this species; indeed, the fractions containing the tetrathionate reductase activity had very low heme content. Hence, it appears that the protein known as OTR is actually mislabeled as such, and that the true *S. oneidensis* octaheme tetrathionate reductase may not even be a c-heme protein. For convenience, in the remainder of the chapter we will continue to refer to the octaheme protein under study as OTR. However, henceforth the protein will be characterized by its hydroxylamine

reductase activity, which is clearly the most prominent activity identified thus far (Figure 4.6).

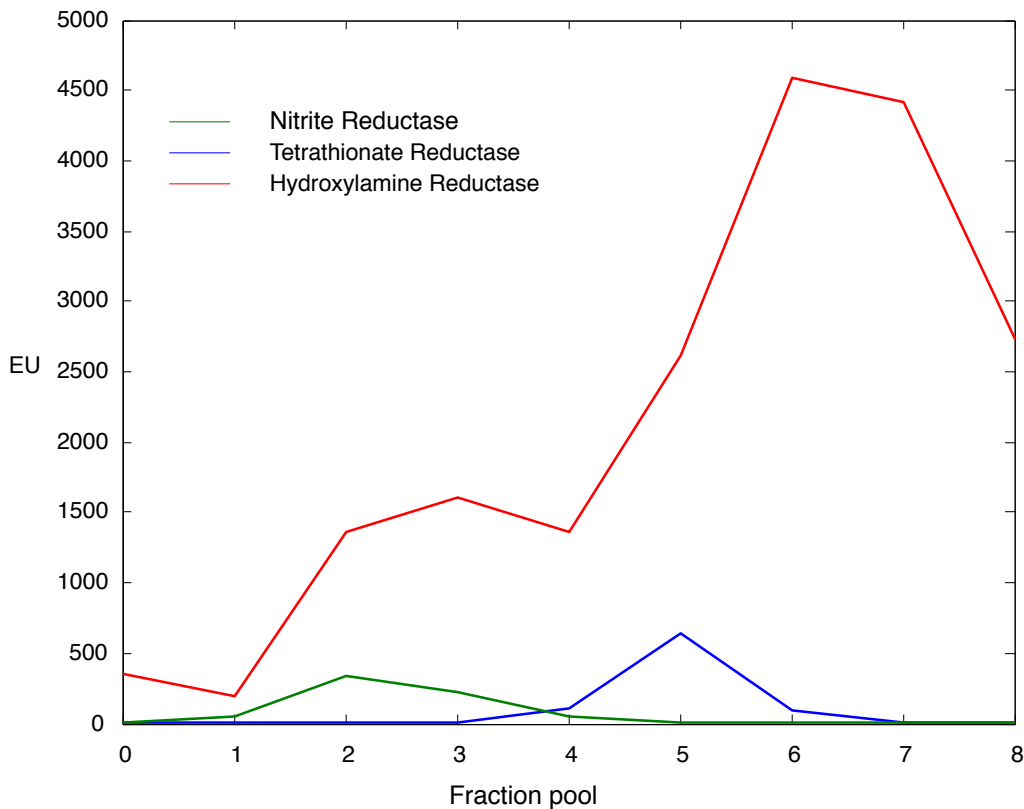


**Figure 4.6** Nitrite, hydroxylamine and tetrathionate reductase activities, as separated by octyl sepharose chromatography of lysate with 30% ammonium sulfate from NS\_432f. The protein was bound to the column at 30% ammonium sulfate in 50mM HEPES pH=7.0 and 1mM EDTA. 6mL fractions were collected during 600mL gradient from 30% to 0% ammonium sulfate.

#### 4.2.4 Streptomycin sulfate additions

Figure 4.7 shows the effect of adding streptomycin sulfate to the clarified NS\_432f cell lysate. Typically this salt is used to precipitate unwanted nucleic acid polymers from crude mixtures of protein and nucleic acid. However, as Figure 4.7 shows, addition of streptomycin sulfate leads to decreases in both absorbance at 410 nm (indicative of heme content in solution), and

hydroxylamine reductase activity. Thus, it appears that OTR is precipitated by streptomycin sulfate, along with nucleic acids.

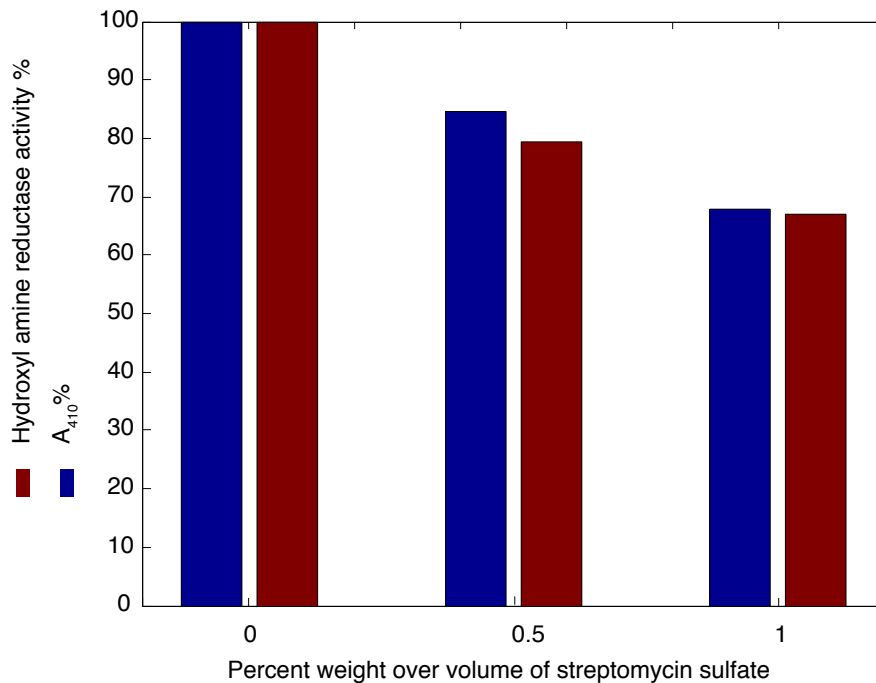


**Figure 4.7** Effect of adding progressively larger amounts of streptomycin sulfate to NS\_432f clarified cell lysate. Streptomycin sulfate was added to a slowly stirring solution as described in methods. The absorbance at 410 nm was measured and correlated to hydroxylamine reductase activity. For convenience in plotting the two disparate quantities on the same graph, absolute values were converted into percentages where the activity and A<sub>410</sub> without streptomycine are taken as 100%.

#### 4.2.5 Ammonium sulfate fractionation

Upon addition of ammonium sulfate a salting in effect was observed; at 20% ammonium sulfate saturation the hydroxylamine reductase activity was 112% of that in clarified lysate. This effect was observed consistently, at various pH values, in all attempts at OTR purification. Hydroxylamine reductase activity present in 50% ammonium-sulfate-saturated supernatant was only 10% of that in lysate. Hence, OTR can be precipitated in a 25-55% saturation pellet. Tris-HCl pH=8.5 buffer was used to re-suspend such a pellet, as OTR was significantly

more difficult to re-dissolve in lower pH buffers. However, even at pH 8.5 only about 70% of activity could be recovered from the pellet (Figure 4.8).

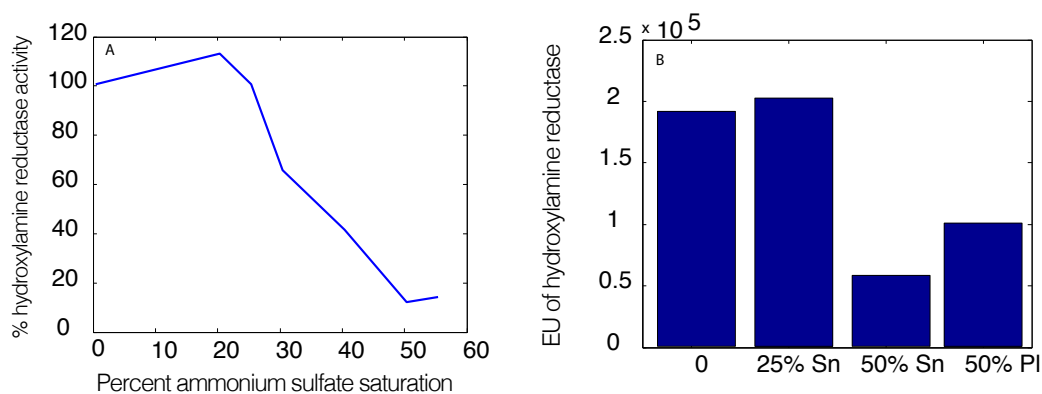


**Figure 4.8. (A) Ammonium sulfate saturation. The activity was measured as described in methods. 100% activity was taken as the activity of the clarified NS\_432f lysate. (B) Lysate in this purification trial contains 190,000 EU; 25% ammonium sulfate supernatant (Sn) 201,000 EU; 50% ammonium sulfate supernatant contains only 57,400 EU. Only 99,500 EU could be re-dissolved out of the pellet (PI). The re-dissolved suspension had to be centrifuged to remove some insoluble debris.**

#### 4.2.6 Serial column chromatography

OTR proved unusually sensitive to all the chromatographic techniques used in its attempted purification. This is seen in Figure 4.9 which plots the enzymatic activities and  $A_{410}/A_{280}$  ratios of the pooled samples obtained from each chromatographic step. The  $A_{410}/A_{280}$  ratio is a quick measure of heme protein purity and in previous publications was found to be  $\sim 4$  for pure OTR<sup>3</sup>. Interestingly, size exclusion chromatography produced the most damage (Figure 4.9); this is usually considered a gentle technique because direct interaction between the protein and gel surface is believed to be minimal. On the other hand size exclusion columns are the longest, so if unfavorable interactions are present they could be magnified.

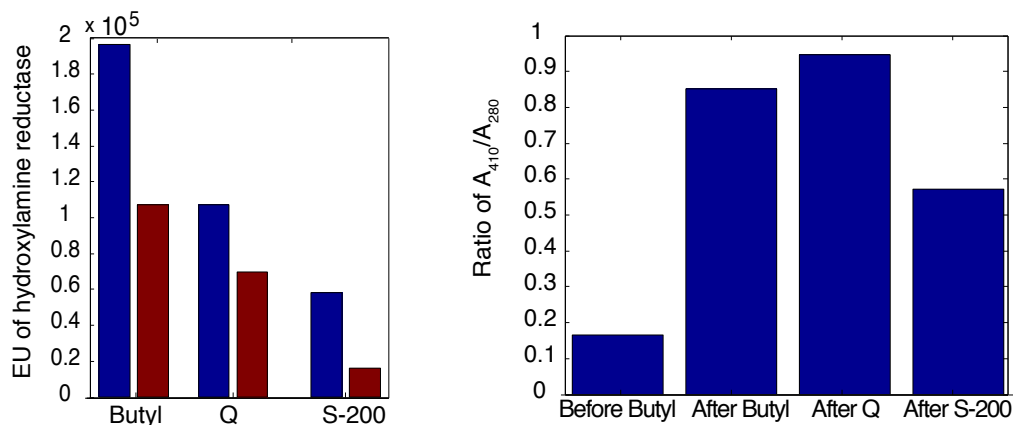


**Figure 4.9** The plots of enzymatic activities (left) and A<sub>410</sub>/A<sub>280</sub> ratios (right) of the pooled samples obtained from each chromatographic step. Left: The blue bars are activities immediately before the column, and the red bars after. The samples were kept in the refrigerator overnight before the next column. Right: A<sub>410</sub>/A<sub>280</sub> ratios as the measure of heme content per protein in the mixture.

### 4.3 Discussion

The pMMB503EH vector had been previously used for expression of OTR and other genes in *Shewanella frigidimarina*.<sup>3,6-8</sup> In this work the same expression vector was found to be suitable for inducible gene expression in *S. oneidensis*. Ten fold, and sometimes higher, over-expression of the enzyme OTR could be achieved in induced cultures. A surprising result of the present work was that the protein hitherto referred to as *S. oneidensis* OTR exhibited no tetrathionate or nitrite reductase activities. However, the putative OTR exhibited elevated hydroxylamine reductase activity.

Attempts to purify OTR led to significant decline in activity with every method used except for fractionation with 20% ammonium sulfate, which actually increased the activity of the soluble fraction. Such an activity increase is commonly known as a “salting in” effect; it is believed that the increase in ionic

strength can aid protein stability, promote proper folding, or enhance the formation of a correct oligomeric state. In the third case one could envision association of two or more OTR subunits, or an interaction of OTR with a physiological partner that produced a more soluble species.

Although OTR is reported to be a monomer based on its crystal structure<sup>1</sup>, electron transferring proteins and redox enzymes often form strong interactions with their electron donating or accepting partners. Addition of ammonium sulfate could promote these interactions if they are driven by hydrophobicity, and it is possible that an OTR-redox partner adduct would be more soluble than the isolated enzyme. Interestingly, OTR exhibits a solvent-accessible cysteine (Figure 4.10). CcNiR from *Desulfovibrio desulfuricans* exhibits a cysteine at its N-terminal, which is used to form a covalent bond with the glyceride-fatty acid lipid of the cytoplasmic membrane. This modification promotes the tight association with its redox partner<sup>9</sup>. Thus, an intriguing possibility is that OTR could also use its accessible cysteine to form a covalent bond with the membrane fatty-acid or even with its physiological partner, and that this bond formation might be promoted by salt elevation if these conditions increased hydrophobic interaction between the partners. The major problem with hypotheses that involve salting-in promoted by heteromeric interactions between OTR and a partner is that in our system OTR is overexpressed, and there is no reason to expect that a putative physiological partner's concentration would be comparable to the overexpressed OTR's. There is no similar objection to proposing that OTR is more stable as a

homo-multimer whose association is promoted by hydrophobic interactions, though as mentioned above the OTR structure doesn't immediately suggest a naturally oligomeric species.

The loss of activity observed with all attempts at chromatographic separation of OTR appears to result from the enzyme's tendency to irreversibly bind to the chromatographic resins' supports. In support of this reasoning, the biggest loss in activity was observed when using the typically non-interacting gel filtration chromatography, a method that often gives recoveries near 100%. OTR's hydroxylamine reductase activity is otherwise unchanged if kept overnight in 4°C, demonstrating that the enzyme is not inherently unstable.

To summarize, the results presented herein show that the enzyme previously identified as an *S. oneidensis*' octaheme tetrathionate reductase actually has no tetrathionate reductase activity, but does exhibit substantial hydroxylamine reductase activity. Though the enzyme can be overexpressed in good yield in *S. oneidensis* using a pMMB503EH expression vector, purification proved surprisingly difficult given that a crystal structure of the enzyme has been reported. It is perhaps telling that the purification protocol that led to the structure used a combination of 3 ion exchange columns and one size exclusion column<sup>7</sup>. This is an unusual strategy, and suggests that the earlier workers also encountered purification difficulties. In Atkinson's thesis she states that doing a repeat separation on a hydroxyapatite column led to an increased yield, from 0.28 to 0.34 mg of pure protein per liter of initial culture<sup>7</sup>.

To our knowledge no membrane fraction analysis of the cell lysate expressing OTR has yet been performed. Given the apparent hydrophobic characteristics of OTR, it is possible that the activity tracked so far is the sonication-emulsified fraction of the total, with the remainder in the insoluble cell debris. Future investigators could analyze a membrane fraction of the NS\_432f culture by solubilizing it in a buffer containing membrane solubilizing agents such as Triton-100.

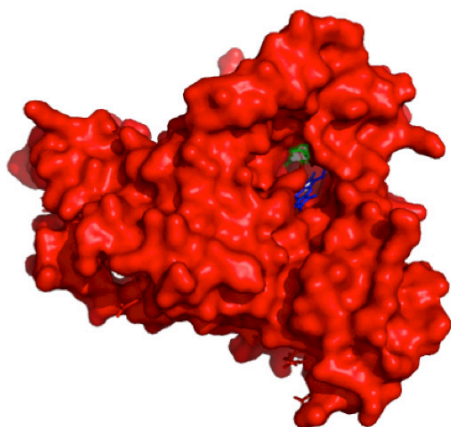


**Figure 4.10** Surface representation of OTR. The five-coordinate active site heme 2 is represented by blue sticks, while the solvent-accessible cysteine is rendered as green sticks.

## 4.4 References

- 1 Mowat, C. G. *et al.* Octaheme tetrathionate reductase is a respiratory enzyme with novel heme ligation. *Nat. Struct. Biol.* **11**, 1023-1024 (2004).
- 2 Mowat, C. G. & Chapman, S. J. Multi-heme cytochromes - new structures, new chemistry. *J. Chem. Soc. Dalton Trans.* **21**, 3381-3389 (2005).
- 3 Atkinson, S. J., Mowat, C. G., Reid, G. A. & Chapman, S. K. An octaheme c-type cytochrome from *Shewanella oneidensis* can reduce nitrite and hydroxylamine. *FEBS Lett.* **581**, 3805-3808 (2007).
- 4 Youngblut, M. *et al.* Laue crystal structure of *Shewanella oneidensis* cytochrome c nitrite reductase from a high-yield expression system. *J. Biol. Inorg. Chem.* **17**, 647-662 (2012).
- 5 Smith, M. C. M. & Sockett, R. E. *Genetic methods for diverse prokaryotes.* (Academic Press, 1999).
- 6 Gordon, E. H. J., Pealing, S. L., Chapman, S. K., Ward, F. B. & Reid, G. A. Physiological function and regulation of flavocytochrome c3, the soluble fumarate reductase from *Shewanella putrefaciens* NCIMB 400. *Microbiology* **144**, 937-945 (1998).
- 7 Atkinson, S. Studies of multiheme proteins from the dissimilatory metal reducing bacteria *Shewanella oneidensis* MR-1 and *Geobacter sulfurreducens* Ph.D. thesis, University of Edinburgh, (2009).
- 8 Wu, F. Novel octaheme cytochrome c tetrathionate reductase (OTR) from *Shewanella oneidensis* MR-1 Ph.D. thesis, University of Edinburgh, (2011).
- 9 Almeida, M. G. *et al.* The isolation and characterization of cytochrome c nitrite reductase subunits (NrfA and NrfH) from *Desulfovibrio desulfuricans* ATCC27774: Re-evaluation of the spectroscopic data and redox properties. *Eur. J. Biochem.* **270**, 3904-3915 (2003).

## 5 *Shewanella oneidensis* Lon Deletion

### 5.1 Background

*S. oneidensis* is a suitable host for overexpression of c-heme proteins<sup>1,2</sup>. The histidine tagged proteins were over-expressed successfully in *S. oneidensis*<sup>1</sup> in an inducible vector at 20°C. Overexpression of affinity tagged protein allows a rapid, one-step procedure for their purification. Tags can also be useful to study the mutants of homologously expressed proteins like CcNiR; histidine tag can separate mutant protein from indigenously expressed wild type. However, in the present expression system<sup>2</sup> at 30°C the polyhistidine tag was degraded. Once the temperature was lowered to 20°C expression itself was minimal. Degradation was reduced when CcNiR was expressed in pMMB503EH under control of tac promoter at 15°C, however, the degradation persisted and yield was not the same as that when expressed at 30°C. Thus improving *Shewanella* as the host seems to be important.

Lon protease is a serine protease responsible for the degradation of small regulatory and long abnormal peptides in the cytoplasm. In bacteria such as *E. coli* and *S. oneidensis* this gene is under heat shock promoter control<sup>3,4</sup>. *E. coli* *B* and its derivative strains, which are most widely used for heterologous expression of recombinant proteins, are deficient in Lon protease<sup>5</sup> because the operon is interrupted by a transposase (Figure 5.1). This is an important feature

for expression of proteins without undesired degradation by the Lon protease. This chapter describes an attempt to shut down Lon protease expression in *S. oneidensis*, to make these bacteria more suitable for biomolecular engineering.

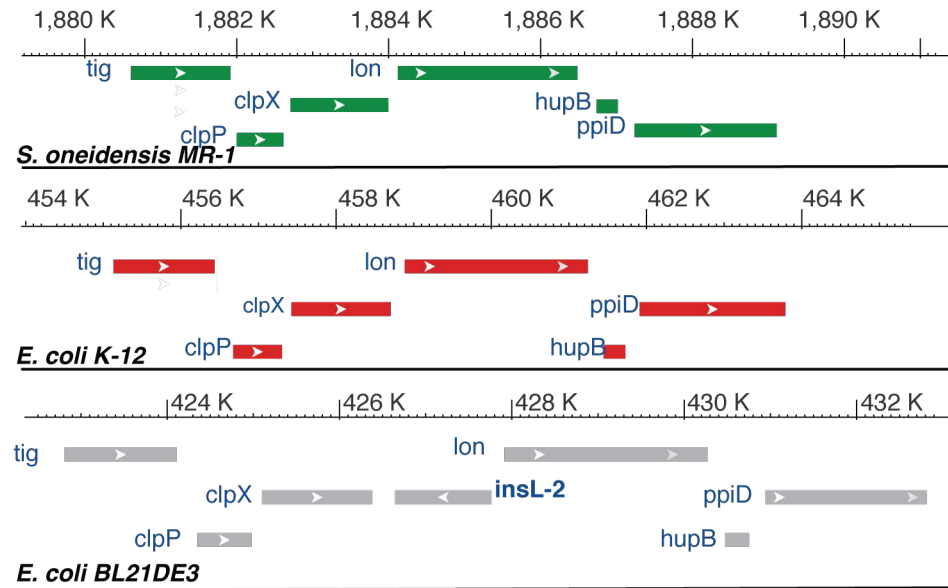


**Figure 5.1** Comparison of the three operons containing Lon protease as identified by the sequence homology. Their positions within their genomes are indicated by a graded line where K stands for thousand. *Shewanella oneidensis* (green) and *E. coli* K-12 (red) have the uninterrupted operons. *E. coli* (green) BL21DE3 has contains a transposase between *clpX* and *lon* sequences. The transposase is potentially responsible for observed Lon deficiency in the BL21DE3 strain.

In gram-negative bacteria *c*-hemes are transported co and post translationally using the SecA system. The emerging pre-protein is held in an unfolded state by the SecB chaperon, while two to three positively charged amino acids near the amino-terminal guide the peptide-chaperon complex to the negatively charged membrane<sup>6</sup>. The leader sequence of *c*-heme proteins contains binding sites for the SecA chaperon that will ultimately provide energy needed to push the peptide across the lipid bilayer. It is unclear exactly how and by what sequences the pre-protein interacts with SecB<sup>7</sup>, but it is plausible that

an artificial sequence at the c-terminus, such as a poly-his tag, would be exposed to proteolysis during the translocation. To guard against this possibility, the effort to eliminate Lon protease was undertaken.

Several strategies are available for engineering a gene deletion. In one relatively simple approach, a transposon that carries an antibiotic marker is inserted into the target gene so as to interrupt its synthesis. These constructs have the drawback of being able to revert to wild type by looping out the transposon. A second strategy is to supplement the organism with a plasmid that codes for anti-RNA for the sequence that needs to be silenced. Stability of the plasmid that carries such an anti-RNA sequence and the efficacy of the silencing, are both significant concerns in this strategy<sup>8</sup>.

Here a third strategy will be used, whereby an in-frame deletion removes the target gene; this is perhaps the most permanent solution for gene deletion<sup>9</sup>. This method takes advantage of prokaryotes' natural ability to acquire and expel DNA<sup>10-12</sup>. In-frame deletions within *S. oneidensis* are carried out routinely to study this organism<sup>13,14</sup>, so methods for achieving them are well established. The challenges associated with this approach are to make a stable deletion construct, and to prevent low homology or non-homologous recombinations<sup>12</sup>.

## 5.2 Methods

### 5.2.1 Suicide construct

The overall method for construction of the suicide construct that would integrate itself into genomic DNA of *S. oneidensis* is outlined in Figure 5.2. The strains and primers used for these experiments are given in Table 5.1. The plasmid pDS132 was kindly provided by Dr. Schneider from Université Joseph Fourier, France. Sequences flanking locus SO\_1796 that codes for the putative Lon protease based on the sequence homology were amplified from MR-1 genomic DNA using Phusion® High-Fidelity PCR Master Mix with HF Buffer, obtained either from New England Biolabs or from Thermo Fisher. Primers ns713a/ns723a were used to amplify the 1000bp fragment A that flanks the 5-prime region, and ns713b/ns723b were used to amplify the 800bp fragment that flanks the 3-prime region. Fragment A was digested with Sall(hf), fragment B with SphI(hf), and pDS132 was double digested with Sall(hf) and SphI(hf). The endonucleases were purchased from NEB. The digested inserts and pDS132 were purified using a PCR clean up kit (Qiagen) to remove small digested polynucleotide leftovers and digestion enzymes from the desired fragments. The clean DNA fragments A and B, and the pDS132, were combined in 5:5:1 ratio and ligated using 2XElectroligase master mix from NEB. Electroligase was then inactivated and removed using the PCR cleanup kit. The clean ligation mixture was separated on 0.7% agarose gel.

Amplify by PCR flanking regions of 600-1000bp with proper restriction sites.

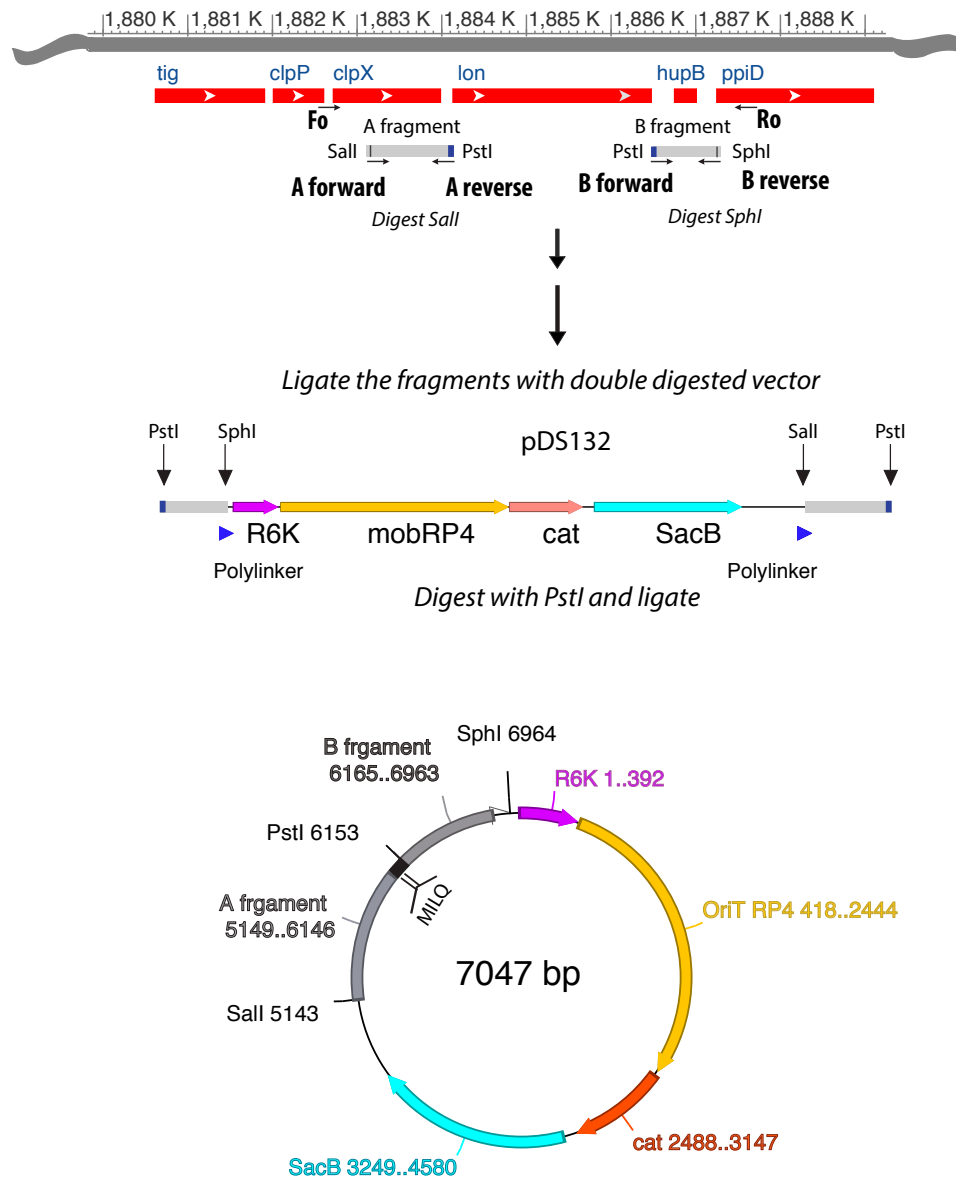


**Figure 5.2** A general scheme for the construction of Lon protease pDS132 vector that contains flanking regions of Lon protease from *S. oneidensis*. Fragment A was amplified with ns723a and ns713a primers, and fragment B with ns723b and 713b primers. For detailed description of the primers see Table 5.1. pDS132 was double digested with *Sall* and *SphI*, fragment A with *Sall*, and fragment B with *SphI*. The digested fragments and vector were ligated together. The linear ligation product was digested with *PstI* and circularized by ligation. A four amino acid sequence MILQ with two stop codons was placed in between the fragments.

**Table 5.1. Upper contains all the primers sequences used in this study and their descriptions in terms of priming regions on *S. oneidensis*' genome and orientations, and the relevant endonuclease sites that they contain. The assignments are given in reference to Figures 5.2 and 5.3. Lower are bacterial cultures that were used in this study.**

<b>Primer</b>	<b>Priming region</b>	
ns713a AAAAAA <u>CTGCAGGATCATAGTTCGATTCCGT</u> TTTAATAAAA	1884128-1884102 plus/minus	PstI site underlined A fragment reverse primer Sequence that codes for MILQ is italicized
ns713b ATATATAT <u>CTGCAGTAATAACGCAAGAAATTGC</u> GCTATCACG	1886479-1886504 plus/plus	PstI site underlined B fragment forward primer Sequence that codes for LQStopStop is italicized
ns723a TATATATAGTCGACGCCTTTTACCATGGCGGAT GCCACAACACTG	1883128-1883158 plus/plus	Sall site underlined A fragment forward primer
ns723b AAAAAAAAGCATGCAATCACGCCTTGCGAAC CATCGCGGATC	1887281-1887252 plus/minus	SphI site underlined B fragment reverse primer
ns810c CCCTTCTGGCCGAAACGCTTGCGCGC	1883091- 1883116 plus/plus	Fo primer
ns810d GGGACTTCGGAGGTTGAGCCTAAATAGCTACT CACGCC	1887362 - 1887325 plus/minus	Ro primer
<b>Organism/strain</b>	<b>Source</b>	<b>Genotype</b>
<i>S. oneidensis</i> MR-1 <i>fccA</i>	Dr. Saffarini	<i>fccA</i> deficient, kanamycin resistant Rifampin resistant
<i>S. oneidensis</i> TSP-C		
<i>E. coli</i> SM10 -pir	Dr. Schneider	Ferrieres, L. <i>et al.</i>
<i>E. coli</i> SM17.1 -pir	Dr. Saffarini	Ferrieres, L. <i>et al.</i>

The properly ligated fragments were cut out and cleaned using Qiagen Qiaxll gel extraction kit. The linear construct was then cut with PstI from NEB according to manufacturer's instructions. The digestion mixture was once again cleaned up with the PCR clean up kit, and then ligated using instant sticky end

ligase master mix from NEB. Chemically competent *E. coli*, either Sm10  $\lambda$  pir or S17.1  $\lambda$  pir cells, were prepared according to the method described in ref. <sup>15</sup>.

These cells were then transformed with 10% volume of ligation over volume of competent cells. The transformed Sm10  $\lambda$  pir were grown on LB agar plates supplemented with chloramphenicol/kanamycin, 50  $\mu$ g/mL (cam<sup>50</sup>/kan<sup>50</sup>), and chloramphenicol/streptomycin (cam<sup>50</sup>/strp<sup>50</sup>) for S17.1  $\lambda$  pir. All *E. coli* colonies were then screened for correct constructs by colony PCR, using ns723a/ns723b primers, or a mini prep followed by the restriction digest Sall/SphI.

### 5.2.2 Conjugation (mating)

Positive clones were mated with either *S. oneidensis* MR-1  $\Delta fccA$  that were provided by Dr. Saffarini (Biosci UWM) or TSP-C strain. Conjugation was performed as follows. The donor *E. coli* and acceptor *S. oneidensis*, cells were grown separately in 5 mL of LB broth each supplemented with appropriate antibiotics at 37°C and 30°C respectively until OD<sub>600</sub> reached ~0.5. The cells were collected by centrifugation and washed twice with SOC medium from Fisher. Finally the donor and acceptor cells were combined in 1:2 ratios, spotted on dry LB agar plates and incubated right side up at 30°C overnight. The following morning the spotted bacteria were collected and plated on LB plates supplemented with chloramphenicol/rifampicin 50 $\mu$ g/mL and 25 $\mu$ g/mL (cam<sup>50</sup>/rif<sup>25</sup>) for TSP-C cells, or cam<sup>50</sup>/kan<sup>25</sup> for MR-1  $\Delta fccA$ . *S. oneidensis* colonies were picked and screened for sucrose sensitivity. The colonies that

were unable to grow on LB cam<sup>50</sup> plates supplemented with 10% weight over volume sucrose were screened for the correct incorporation of suicide construct by a colony PCR using ns810c and ns810d primers (Table 5.1) as Fo and Ro primers, with extension time appropriate for wild type configuration as outlined in Figure 5.2. The correctly integrated colonies were expected to have no product because the distance between them would be too large to cover in the time used for wild type PCR. The colonies that underwent illegitimate integration were expected to have a wild type PCR product. The colonies that exhibited no PCR product in the initial PCR screening were then screened to determine the orientation of the insert, using combinations of Fo/B reverse and A forward/Ro primers.

### 5.3 Results and Conclusion

In *S. oneidensis* the Lon protease is coded by the locus SO\_1796. The goal of the procedure described in this chapter was to permanently delete this gene. First, the plasmid pDS132 construct that carries the flanking sequence of SO\_1796 was supposed to integrate itself, as graphically outlined in Figure 5.3, using the RecA homologous recombination mechanism.

This integration, although rare, is one of the few ways that a plasmid that has only an R6K origin of replication can reproduce in an organism that has no pi protein that is required for its replication. Gram negative bacteria does not possess this protein unless specifically engineered to carry a pir gene that codes for the pi protein like *E. coli* Sm10  $\lambda$  pir, S17.1  $\lambda$  pir or 5Halp  $\lambda$  pir strains <sup>16</sup>.

In this mechanism RecA binds the single stranded DNA that enters the cell via conjugation or other transformation methods. The complex is then aligned with the double stranded homologous region located on genomic DNA<sup>17</sup>. The single strand is then incorporated into genomic DNA. Other methods that are also called 'illegitimate' are possible when the integration occurs as a result of double stranded break and repair of genomic DNA<sup>18</sup>.

In theory, once the correct vector incorporation was confirmed, the colonies could undergo a resolution step (Figure 5.3B) This step is accomplished by growing the correct *S. oneidensis* colonies in LB without antibiotic or NaCl to  $OD_{600} = 0.5$ . Plate 100 $\mu$ L aliquots on LB agar plates that contain 10% sucrose and no antibiotic then incubate at 30°C overnight. The colonies that grow on sucrose are tested for inability to grow on chloramphenicol and then screened for the deletion product by colony PCR using the Fo and Ro primers (Figure 5.2). Fifty percent of the colonies are expected to revert to wild type and the other fifty should be the deletion.

Many problems were encountered with stability of the suicide vector construct. When *E. coli* were transformed with ligation, only *E. coli* S17.1  $\lambda$ -pir strain, but not SM10  $\lambda$ -pir strain, was found to maintain the deletion construct, although both strains could maintain pDS132. Upon screening of these clones, either an empty pDS132 or a mixture of differently altered inserts would appear

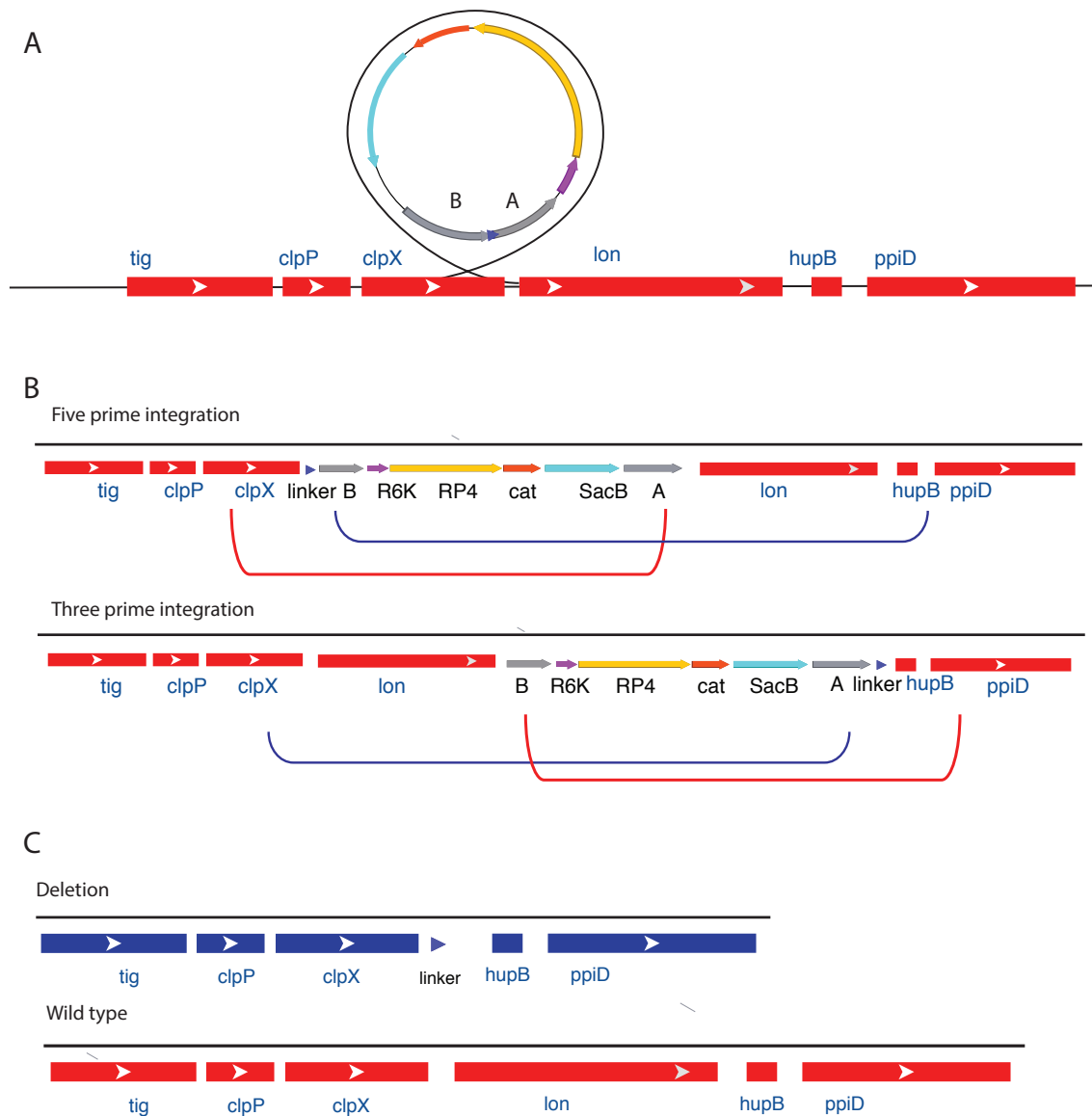


**Figure 5.3 Homology driven integration and resolution of a vector. (A) Homologous region of a plasmid is aligned with that of the *S. oneidensis* genomic DNA. Shown is the alignment of the A fragment that would lead to a five prime integration. Alignment of B fragments would lead to three-prime integration. (B) Example of the five-prime and the three prime integration of suicide construct and the possible resolution combinations. If resolution results from alignment of regions linked by the blue line, a deletion arrangement will result. If resolution results from alignment of regions linked by the red line, a wild type arrangement will be maintained. (C) Deletion and wild type arrangements in the Lon containing operon.**

It is unclear why the S17.1  $\lambda$ -pir strain was able to maintain the deletion construct, while SM10  $\lambda$ -pir could not. One possibility is that the insert is somehow toxic to the cells, and the *E. coli* S17.1  $\lambda$ -pir strain is better at altering the construct. Alternatively, since the deletion insert consists of large non-coding sequences that are rich in poly-A and poly-T stretches, it may not be replicated properly in these host cells. In other words, the latter possibility is that this insert is unstable.

Once the construct was trans-conjugated only plates with TSP-C cells had colonies. This difference in frequency of recombination can be attributed to small differences in strains' ability to incorporate foreign DNA.

The results from the screening of TSP-C recombinants also suggest that the construct is unstable. The initial screening by colony PCR of *S. oneidensis* colonies that were resistant to chloramphenicol and sucrose sensitive had many negatives. However, when these colonies would be screened for insert orientation they all appeared to either have reverted to the wild type or have an incorrect PCR size all together.

If this project is pursued further, cloning the insert into a conventional cloning vector and propagating it in an *E. coli* cloning strain should test its stability. After propagation several colonies can be tested by the colony PCR or a mini prep, followed by a restriction digest. If an insert is indeed unstable, different sized and combinations of fragments A and B can be tested until a stable combination is achieved. Alternatively an attempt can be made to interrupt

expression of Lon protease by transposon insertion. If the method proves more successful, initial tests to characterize an expression in a Lon deficient strain can follow.

A third option is to find a strain or *Shewanella* that is naturally Lon deficient.

## 5.4 References

- 1 Shi, L., Lin, J. T., Markillie, L. M., Squier, T. C. & Hooker, B. S. Overexpression of multi-heme C-type cytochromes. *BioTechniques* **38**, 297-299 (2005).
- 2 Youngblut, M. *et al.* Laue crystal structure of *Shewanella oneidensis* cytochrome c nitrite reductase from a high-yield expression system. *JBIC* **17**, 647-662, doi:10.1007/s00775-012-0885-0 (2012).
- 3 Lee, I. & Suzuki, C. K. Functional mechanics of the ATP-dependent Lon protease lessons from endogenous protein and synthetic peptide substrates. *Biochim Biophys Acta*. **1784**, 727-735 (2008).
- 4 Tsilibaris, V., Maenhaut-Michel, G. & Van Melderen, L. Biological roles of the Lon ATP-dependent protease. *Research in Microbiology* **157**, 701-713, doi:10.1016/j.resmic.2006.05.004 (2006).
- 5 Terpe, K. Overview of bacterial expression systems for heterologous protein production: from molecular and biochemical fundamentals to commercial systems. *Applied microbiology and biotechnology* **72**, 211-222, doi:10.1007/s00253-006-0465-8 (2006).
- 6 Driessen, A. J. M., Manting, E. H. & van der Does, C. The structural basis of protein targeting and translocation in bacteria. *Nature structural biology* **8**, 492-498, doi:10.1038/88549 (2001).
- 7 Hegde, R. S. & Bernstein, H. D. The surprising complexity of signal sequences. *TRENDS in Biochemical Sciences* **31**, 563-571, doi:10.1016/j.tibs.2006.08.004 (2006).
- 8 Dias, N. & Stein, C. A. Antisense oligonucleotides: basic concepts and mechanisms. *Molecular cancer therapeutics* **1**, 347-355 (2002).
- 9 Link, A. J., Phillips, D. & Church, G. M. Methods for generating precise deletions and insertions in the genome of wild-type *Escherichia coli*: application to open reading frame characterization. *Journal of bacteriology* **179**, 6228-6237 (1997).
- 10 Ochman, H., Lawrence, J. G. & Groisman, E. A. Lateral gene transfer and the nature of bacterial innovation. *Nature* **405**, 299-304, doi:10.1038/35012500 (2000).
- 11 Thomas, C. M. & Nielsen, K. M. Mechanisms of, and barriers to, horizontal gene transfer between bacteria. *NATURE REVIEWS MICROBIOLOGY* **3**, 711-721, doi:10.1038/nrmicro1234 (2005).
- 12 Lovett, S. T., Hurley, R. L., Sutura, J., Vincent A. , Aubuchon, R. H. & Lebedeva, M. A. Crossing Over Between Regions of Limited Homology in

- Escherichia coli*: RecA-Dependent and RecA-Independent Pathways. *Genetics* **160**, 851-859 (2002).
- 13 Gorby, Y. A. *et al.* Electrically conductive bacterial nanowires produced by *Shewanella oneidensis* strain MR-1 and other microorganisms. *Proceedings of the National Academy of Sciences of the United States of America* **103**, 11358-11363, doi:10.1073/pnas.0604517103 (2006).
  - 14 Burns, J. L. & DiChristina, T. J. Anaerobic respiration of elemental sulfur and thiosulfate by *Shewanella oneidensis* MR-1 requires psrA, a homolog of the phsA gene of *Salmonella enterica serovar typhimurium* LT2. *Applied and environmental microbiology* **75**, 5209-5217, doi:10.1128/AEM.00888-09 (2009).
  - 15 Glover, D. M. *DNA cloning : a practical approach*. 109-135 (IRL Press, 1985).
  - 16 Ferrieres, L. *et al.* Silent mischief: bacteriophage Mu insertions contaminate products of *Escherichia coli* random mutagenesis performed using suicidal transposon delivery plasmids mobilized by broad-host-range RP4 conjugative machinery. *Journal of bacteriology* **192**, 6418-6427, doi:10.1128/JB.00621-10 (2010).
  - 17 Sung, P. & Klein, H. Mechanism of homologous recombination: mediators and helicases take on regulatory functions. *Nature Reviews Molecular Cell Biology* **7**, 739-750, doi:10.1038/nrm2008 (2006).
  - 18 Heller, R. C. & Marians, K. J. Replisome assembly and the direct restart of stalled replication forks. *Nature Reviews Molecular Cell Biology* **7**, 932-943, doi:10.1038/nrm2058 (2006).

## 6 DsbA leader peptide mediated translocation of tagged CcNiR in *S. oneidensis*

### 6.1 Background

In gram negative bacteria *c*-heme pre-proteins are transferred to the periplasm via the SecA pathway <sup>1</sup>. This pathway transports the unfolded peptides co- and post-translationally. First, the peptides bind to SecB chaperons that keep them in an unfolded state. SecA then docks to the SecB/peptide complex and commences translocation via the SecYEG channel <sup>2</sup>. As discussed in Chapter 5, one possible reason for the degradation of carboxyl terminal His-tagged proteins in *S. oneidensis* TSP-C is that the tags are degraded by cytoplasmic proteases between the time that the pre-protein emerges from a ribosome and the time that it is transferred to the periplasm.

Another pathway that translocates the unfolded peptides to the periplasm does so only co-translationally <sup>2</sup>. This pathway utilizes signal recognition particles (SRPs) that bind the emerging leader peptides as soon as a leader peptide emerge from a ribosome, and halt the remaining translation until the complex docks to the SecYEG translocon. At that point SRPs dissociate, and the translation resumes while the peptide being translated <sup>3</sup>. This method ensures that the nascent peptide does not come into contact with the cytoplasm. One protein that is transported to the periplasm via this pathway is disulfide oxidoreductase (DsbA). The DsbA leader peptide (DsbAlp) was used

successfully for translocating pre-proteins in co-translational fashion in high yield in *E. coli*<sup>4</sup>.

This chapter describes the construction of a DsbAlpCcNiR hybrid gene, and its expression in *S. oneidensis* TSP-C and in *S. oneidensis*  $\Delta$ MtrA/ $\Delta$ DegP<sup>5</sup>. The latter strain was kindly provided by Dr. Johannes Gescher from the Institute of Applied Biosciences, Baden-Wuerttemberg, Germany. The amino acid sequences of the small tetraheme-c leader peptide (STC1p) that was used in the previous publications<sup>6,7,8</sup> and DsbAlp are compared in Figure 6.1. This study is complementary to that presented in Chapter 5. If *S. oneidensis* Lon protease were indeed the main contributor of His-tag degradation at the carboxyl terminal, then a switch to DsbAlp should result in significantly less degradation.

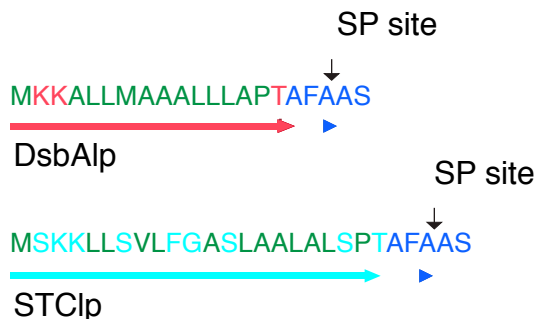


**Figure 6.1.** Comparison of leader peptides that were tested in this study. Underlined in red is the DsbA portion of the peptide from the *S. oneidensis* locus SO\_0333, and in cyan the leader peptide from *S. oneidensis*' small tetraheme-c locus SO\_2727. In blue are the signal peptidase recognition sites, with arrows indicating the exact cleavage site. In green are the hydrophobic residues. In the STC1p these residues are interspersed. DsbAlp contains a solid hydrophobic core; the property responsible for the recognition of this leader peptide by SRPs 3,4.

## 6.2 Materials and Methods

### 6.2.1 Leader sequence replacement

A maxi-prep of 6X-his-tagged optimized CcNiR in pHSG299 (NS\_583a) was used as a template for leader sequence replacement, using primers NS\_815a and NS\_815b (Table 6.1), and Taq-98 (HS) 2X PCR master mix from Lucigen. The replacement PCR was conducted according to the manufacturer's instructions. Additional details are summarized in Figure 6.2.

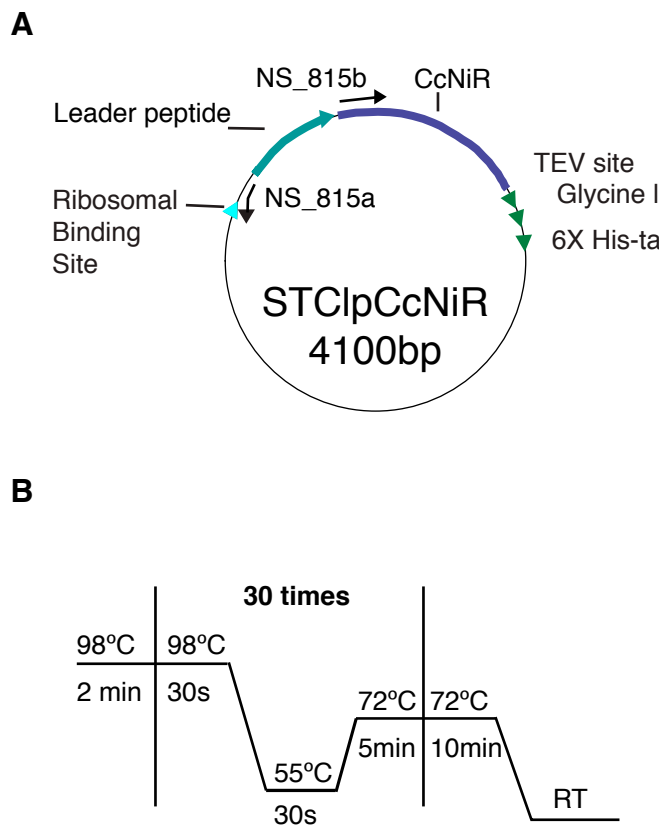


**Figure 6.2. (A) graphic depiction of primer annealing to the template. The primers NS\_815a and b (Table 6.1) bind outside of STClp, and carry the sequence that codes for the DsbAlp. (B) cycling parameters for the PCR. Each round will amplify the entire plasmid.**

The PCR product was treated with DpnI from NEB to remove methylated template DNA. Then the treated PCR fragments were ligated using NEB 2Xblunt ligation master mix. The *E. coli* NEB5alpha competent cells were transformed with the ligation mixture according to the manufacturer's instructions and plated on LB agar plates that contained kanamycin 50µg/mL (LB kan<sup>50</sup>), then incubated upside down, overnight, at 37°C. Several clones were selected for screening.

The mini-preps of the plasmids from the select clones were prepared using QuickLyse Miniprep Kit from Qiagen. The correct clone was confirmed first by the mini-prep digestion with AfeI from NEB. The site for this endonuclease is present in DsbAlp, but not in STC1p. The clones that were linearized with this endonuclease, as confirmed by an agarose gel electrophoresis, were then verified by sequencing performed by Cancer Research Center at University of Chicago. Upon the complete verification, the cultures of *E. coli* NEB5alpha with the correct construct, DsbAlpCcNiR, were stored as a permanent stock in a 10% glycerol inside an -80°C freezer. For the list of labels and descriptions of primers, constructs and cultures see table 5.1. A maxi-prep of the correct construct DsbAlpCcNiR was prepared, and stored in -20°C.

A plasmid mini-prep from *E. coli* NEB5alpha\_DsbAlpCcNiR, was electroporated into electrocompetent *S. oneidensis* TSP-C and *S. oneidensis* ΔMtrA/ΔDegP. The permanent stocks of *S. oneidensis* ΔMtrA/ΔDegP in 20% glycerol are stored in -80°C labeled NS\_680a.

The electrocompetent cells were prepared similarly to the method described in Myers et al<sup>9</sup>. Instead of sorbitol at pH=7.59, 10% glycerol in nano-pure water was used as an electroporation buffer. All electroporations were conducted in 2 cm electroporation cuvettes from Eppendorf with an Eppendorf Eporator. The voltage was set at 2.5kV.

The TSP-C transformants, TSP-C\_DsbAlpCcNiR, were plated on LB agar plates supplemented with 25µg/mL rifampin and 50µg/mL kanamycin (LB rif<sup>25</sup>/kan<sup>50</sup>) (both from Fisher). The *S. oneidensis* ΔMtrA/ΔDegP transformants, ΔMtrA/ΔDegP\_DsbAlpCcNiR, were plated on LB kan<sup>50</sup>. The plates were incubated upside down at 30°C overnight. The permanent stocks of these cultures in 10% glycerol are stored in -80°C freezer; for labels see the Table 6.1.

**Table 6.1. Primers, constructs and cultures used in this study**

<b>Primer name</b>	<b>Sequence</b>	<b>Description</b>
NS_815a	5' <u>GTAATGCTTTTTTCATAATTGTATCC</u> TCCGAATTCactggc3'	The underlined sequence codes for MKKAL(1/3L). The primer is phosphorylated at 5 prime end.
NS_815b	5' <u>TTATGGCGGCAGCGCTGTTATTGGC</u> <u>TCCTACCGCCTTTGCGTCGG3'</u>	The underline sequences for (2/3L)MAAALLLA. The primer is phosphorylated at 5 prime end.
<b>Construct label</b>	<b>Construct Description</b>	<b>Construct source</b>
NS_583a	An optimized CcNiR gene from <i>S. oneidensis</i> with leader peptide derived from small tetraheme c (STC) from <i>S. oneidensis</i> as shown in figure 5.1 in pHSG299. Tobacco Etch Virus (TEV) protease site followed by polyglycine flexible linker and 6XHis-tag at the Carboxyl terminal as shown in the figure 5.2. In text referred to as STClpCcNiR.	Pacheco lab
NS_827r	Same as NS_583a, but with DsbA leader peptide from <i>S. oneidensis</i> . In text referred to as DsbAlpCcNiR.	Pacheco lab
<b>Culture label</b>	<b>Culture description</b>	<b>Culture source</b>
<i>S. oneidensis</i> TSP-C	Rifampin resistant strain of <i>S. oneidensis</i> .	
NS_680a	<i>S. oneidensis</i> $\Delta$ MtrA/ $\Delta$ DegP	Dr. Johannes Gescher
NS_584b1	<i>S. oneidensis</i> TSP-C with the STClpCcNiR construct. In text referred to as TSP-C_ STClpCcNiR.	Pacheco lab
NS_824a1	<i>E. coli</i> NEB5alpha with DsbAlpCcNiR construct. In text referred to as NEB5alpha_ DsbAlpCcNiR	Pacheco lab
NS_827n	TSP-C with the DsbAlpCcNiR construct. In text referred to as TSP-C_ DsbAlpCcNiR	Pacheco lab
NS_830a	<i>S. oneidensis</i> $\Delta$ MtrA/ $\Delta$ DegP with the DsbAlpCcNiR construct. In text referred to as $\Delta$ MtrA/ $\Delta$ DegP DsbAlpCcNiR.	Pacheco lab

### 6.2.2 Expression and 6XHis-tag integrity assessment

To compare the expression levels in *S. oneidensis* TSP-C and the 6XHis-tag integrity as expressed by STClpCcNiR versus DsbAlpCcNiR, cell pellets were prepared as follows. Two 45mL conical falcon tubes with 10mL LB rif<sup>25</sup>/kan<sup>50</sup> were inoculated with a scrape from permanent stock cultures, one from TSP-CDsbAlpCcNiR and the other from TSP-C\_ STClpCcNiR. These tubes were incubated overnight in a shaking incubator at 30°C. The following morning each overnight culture was transferred into a 2L flask containing 1L LB rif<sup>25</sup>/kan<sup>50</sup>. The incubation continued for an additional 24 hours. The cells were harvested by centrifugation at 1,000 g for 30 min at 4°C. Each pellet was resuspended in approximately 40mL of 50mM HEPES pH=8.0, 500mM NaCl supplemented with 2mM pefabloc and 5µM leupeptin. The cells were disrupted by sonication on ice. The insoluble debris was removed by centrifugation at 60,000 g, 4°C for 30 minutes. The supernatants of both lysates were tested for the nitrite reductase activity as describe in Chapter 4. The histidine tag integrity was assessed by the ability of CcNiR from lysate DsbAlpCcNiR to bind to the 5mL Ni-NTA column. The activities of the collected flow-throughs were compared with that of the cleared cell lysate loaded on the column.

To check expression levels of DsbAlpCcNiR in *S. oneidensis*  $\Delta$ MtrA/ $\Delta$ DegP a scrape of each permanent stock,  $\Delta$ MtrA/ $\Delta$ DegP\_ DsbAlpCcNiR and *S. oneidensis*  $\Delta$ MtrA/ $\Delta$ DegP, were added to the 2ml of LB broth inside a 10ml round bottom culture tube and incubated for 24 hours at 30°C with agitation.

LB for  $\Delta$ MtrA/ $\Delta$ DegPDsbAlpCcNiR culture was supplemented with kan<sup>50</sup>, and 10% of v/v of DMSO was added to both cultures because of a previous observation that, at least in the TSP-C strain with a non-inducible expression system, the yield was lower if DMSO was not included. The cells were collected by centrifugation in a table top centrifuge at 10,000 g for 2 minutes. The pellets were resuspended in 1mL of 50mM HEPES pH=8.0, 500mM NaCl and 2mM pepabloc with 5 $\mu$ M leupeptin. The cells were disrupted by three freeze-thaw cycles. The insoluble debris was removed by centrifugation in a table-top centrifuge at 14,000g for five minutes. A smaller, 1 ml, Ni-NTA column was used to test the binding of CcNiR to nickel-resin. The nitrite reductase activity was measured as described in Chapter 4.

## 6.3 Results and Discussion

### 6.3.1 DsbA leader sequence insertion

The leader sequence was inserted successfully, as verified by both Afel digestion and sequencing. DpnI digestion was needed in this case; an attempt to bypass this step resulted in large number of colonies with template DNA.

### 6.3.2 Expression and Ni-NTA binding

The cleared lysate from the newly created TSP-C\_DsbAlpCcNiR, contained 114% more nitrite reductase activity than that from TSP-C\_STClpCcNiR culture. The nearly identical expression may be an indicator that a bottleneck for the periplasmic translocation is at the SecYEG translocon.

The cleared lysate from TSP-C\_DsbAlpCcNiR and the flow-through collected after loading it onto Ni-NTA, contained identical amounts of nitrite reductase activity. Thus, co-translational translocation did not rescue the tag at the carboxyl terminal.

Next, the expression levels and the histidine tag degradation in *S. oneidensis*  $\Delta$ MtrA/ $\Delta$ DegP were tested. In this case the comparison was made between the empty *S. oneidensis*  $\Delta$ MtrA/ $\Delta$ DegP and those that contained the  $\Delta$ MtrA/ $\Delta$ DegP\_DsbAlpCcNiR. The nitrite reductase activity in the cleared lysate from  $\Delta$ MtrA/ $\Delta$ DegP\_DsbAlpCcNiR was 52.5 times higher than that in the lysate *S. oneidensis*  $\Delta$ MtrA/ $\Delta$ DegP. Furthermore, in an SDS-PAGE gel of the lysates the 50kDa CcNiR band was easily observable for  $\Delta$ MtrA/ $\Delta$ DegP\_DsbAlpCcNiR, the first time for a cleared cell lysate (figure 6.3). However, almost all activity ended up in the flow through. The result indicates that DegP deletion alone does not rescue the tags at the carboxyl terminal.

DsbAlpCcNiR provides an effective means of transporting CcNiR pre protein peptide cotranslationally into the periplasm of *S. oneidensis*. The transport protects from cytoplasmic proteases and aggregations. The persistent degradation of the tag attached to the carboxyl terminal suggests the presence of at least one protease that degrades the tags in the periplasm. On the other hand, a highly active alkaline protease may exist in the cytoplasm that degrades the peptide efficiently at 4°C, and is not inhibited by the protease inhibitors in the

concentrations used in this study. In this case the degradation may happen after the cell lysis too.

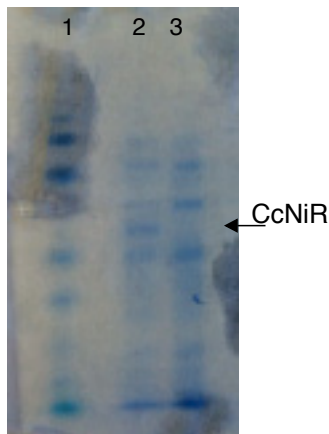


**Figure 6.3.** Lane 1: EZ-run pre-stained RecA ladder from Fisher Scientific. Lane 2: cleared lysate from  $\Delta MtrA/\Delta DegP\_DsbAlpCcNiR$ . Lane 3: cleared lysate from *S. oneidensis*  $\Delta MtrA/\Delta DegP$

In Chapter 5 the motivation behind the deletion of Lon protease stemmed from the observation that Lon is one protease that the more robust expression hosts that produce intact recombinant proteins are deficient in. These results indicate that there may be a periplasmic protease that is present in *S. oneidensis*, but not *E. coli*. Provided DsbAlpCcNiR construct is used in future studies, a rigorous bioinformatic comparison between the *E. coli* and *S. oneidensis* periplasmic proteases may shed a light on the conundrum of tag degradation.

An alternative strategy would be to test other *Shewanella* strains to see if they can express intact His-tagged protein.

## 6.4 References

- 1 Thony-Meyer, L. & Kunzler, P. Translocation to the periplasm and signal sequence cleavage of preapocytochrome c depend on sec and lep, but not on the ccm gene products. *European journal of biochemistry / FEBS* **246**, 794-799 (1997).
- 2 Mergulhao, F. J., Summers, D. K. & Monteiro, G. A. Recombinant protein secretion in *Escherichia coli*. *Biotechnol Adv* **23**, 177-202, doi:10.1016/j.biotechadv.2004.11.003 (2005).
- 3 Driessen, A. J. M., Manting, E. H. & van der Does, C. The structural basis of protein targeting and translocation in bacteria. *Nature structural biology* **8**, 492-498, doi:10.1038/88549 (2001).
- 4 Schierle, C. F. *et al.* The DsbA signal sequence directs efficient, cotranslational export of passenger proteins to the *Escherichia coli* periplasm via the signal recognition particle pathway. *Journal of bacteriology* **185**, 5706-5713 (2003).
- 5 Schicklberger, M., Bucking, C., Schuetz, B., Heide, H. & Gescher, J. Involvement of the *Shewanella oneidensis* Decaheme Cytochrome MtrA in the Periplasmic Stability of the  $\beta$ -Barrel Protein MtrB. *Applied and environmental microbiology* **77**, 1520-1523, doi:10.1128/aem.01201-10 (2010).
- 6 Judd, E. T., Youngblut, M., Pacheco, A. A. & Elliott, S. J. Direct Electrochemistry of *Shewanella oneidensis* Cytochrome c Nitrite Reductase: Evidence of Interactions across the Dimeric Interface. *Biochemistry* **51**, 10175-10185, doi:10.1021/bi3011708 (2012).
- 7 Youngblut, M. *et al.* Laue crystal structure of *Shewanella oneidensis* cytochrome c nitrite reductase from a high-yield expression system. *JBIC* **17**, 647-662, doi:10.1007/s00775-012-0885-0 (2012).
- 8 Youngblut, M. *et al.* *Shewanella oneidensis* CytochromecNitrite Reductase (ccNiR) Does Not Disproportionate Hydroxylamine to Ammonia and Nitrite, Despite a Strongly Favorable Driving Force. *Biochemistry* **53**, 2136-2144, doi:10.1021/bi401705d (2014).
- 9 Myers, C. R. & Myers, J. M. Isolation and characterization of a transposon mutant of *Shewanella putrefaciens* MR-1 deficient in fumarate reductase. *Letters in applied microbiology* **25**, 162-168 (1997).

## ACKNOWLEDGMENTS

Many people have helped me during my career as a PhD student.

My adviser, Dr. Andy Pacheco, provided me with the guidance how to conduct science and freedom to develop my own ideas. Dr. Brian Bennett's advice and collaboration were crucial for my research.

My coworkers, made this, often difficult, journey easier whether by landing a hand with an experiment or a cheer when things were not going well. Many undergraduates put a lot of work into my research and I am especially grateful to Dan Love and Tyler Blanke. I would also like to thank Evan Judd from Boston University who provided collaboration and ideas.

The research described in here would not be possible without the financial support from National Science Foundation.

But most of all I would like to thank my husband for cheering me on and being by my side no matter what. I couldn't have asked for a better partner in life.

# CURRICULUM VITAE

## Natalia Stein

### Education

#### Ph.D. in Biochemistry

May 2015

University of Wisconsin Milwaukee

Spectroscopic and electrochemical studies of *Shewanella oneidensis* cytochrome c nitrite reductase, and improving c-heme expression systems

#### B.S. in Biochemistry

2002-2007

University of Wisconsin-Milwaukee

Minor: Biology

Certificate: Biotechnology

### Teaching Experience

Trainer and Supervisor of Undergraduate and Graduate students 2010-present

- Trained graduate and undergraduate students to conduct laboratory experiments using industry standard laboratory equipment.
- Trained students in computational software such as Origin, KaleidaGraph, MathCad, and MatLab.

Graduate/Undergraduate Teaching Assistant

2006-2010

- Conducted discussions.
- Supervised laboratories.
- Graded quizzes and lab reports.

- Assisted in exam proctoring and grading.

Tutor at UWM Supplemental Instruction Center

2005-2006

- Provided tutoring for 100 and 200 level chemistry courses.

-

## Research Experience

Graduate Researcher

Advisor: Andy Pacheco

Fall 2009-Present

Spectropotentiometric analysis of Cytochrome c Nitrite Reductase.

- Developed conditions for potentiometric titrations of CcNiR.
- Performed potentiometric titrations using an Optically Transparent Thin-layer Electrochemical (OTTLE) UV-vis cell and bulk electrolysis cell for analysis by Electron Paramagnetic Resonance (EPR).
- Analyzed and simulated data using Singular Value Decomposition (SVD), global fitting, and least square non linear fitting. Used various computational softwares subroutines for these analyses:

ORIGINE 6.0, KaleidaGraph, MathCad, MatLab

Tag degradation analysis by *Shewanella oneidensis*.

- Used Polymerase Chain Reactions (PCR) to attach tags to Octaheme Tetrathionate Reductase (OTR) and Cytochrome c Nitrite Reductase (CcNiR).
- Tested the ability of these proteins to bind to nickel or StrepII columns after expression at various conditions.

Expression of Octaheme Tetrathionate Reductase (OTR).

- Cloned OTR in to pMMB503EH vector. Transferred the construct into *Shewanella oneidensis* by transconjugation.

- Used *Shewanella oneidensis* as expression host and optimized conditions for expression.
- Determined proper substrate and conditions for assay to track OTR activity in cleared lysate.
- Used glove box to perform enzymatic assays in anaerobic environment.
- Developed bulk electrolysis protocols.

### Undergraduate/Graduate Researcher

Advisor: Graham Moran

Summer 2006-summer 2009

Maleic acid cis trans isomerase sub cloning.

- Subcloned Maleic acid cis trans isomerase into pET17b.
- Developed activity assay.

Hydroxyphenylpyruvate dioxygenase (HPPD) mutagenesis.

- Designed primers for mutagenesis of c-terminus of HPPD. Performed mutagenesis polymerase chain reaction and prepared cell cultures for testing.
- Assisted in purification of HPPD, performed activity assays using UV-vis and oxygen probe.

### Presentations and Posters

Natalia Stein & Andy Pacheco. (2014). Ligand binding and reduction potentials of Cytochrome c Nitrite Reductase (CcNiR). Oral presentation for Biophysics seminar, 03/14/2014, University of Wisconsin-Milwaukee Physics Department.

Natalia Stein, Dan Love, Brian Bennett, & Andy Pacheco. (2014). Electron distribution within the Cytochrome c Nitrite Reductase (CcNiR) hemes as a function of applied potential: a spectro-potentiometric analysis. Poster for Gordon

Research Conference Metals in Biology, 01/26-31/2014, Ventura, CA.

Natalia Stein, Dan Love, Brian Bennett, & Andy Pacheco. (2013). Electron distribution within the Cytochrome c Nitrite Reductase hemes as a function of applied potential. Oral Presentation for American Chemical Society Regional Meeting, 06/6-8/2013, LaCrosse, WI.

Natalia Stein, Dan Love, Brian Bennett, & Andy Pacheco. (2013). Electron distribution within the Cytochrome c Nitrite Reductase hemes as a function of applied potential. Poster for American Society of Biochemistry and Molecular Biology Annual Conference, 04/20-25/2013, Boston, MA.

Natalia Stein, & Andy Pacheco. (2013). Spectro-electrochemistry: Combining methods for analysis of redox centers. Oral presentation for Recruitment Weekend, 04/19/2013, University of Wisconsin-Milwaukee.

Natalia Stein, Brian Bennett, & Andy Pacheco. (2012). Effects of active site ligation on heme potentials in CcNiR. Poster for Midwest Enzyme Chemistry Conference, 10/13/2012, Chicago, IL.

## **Publications**

Matthew Youngblut, Daniel J. Pauly, Natalia Stein, Daniel Walters, John A. Conrad, Graham R. Moran, Brian Bennett, & A. Andrew Pacheco. (2014). *Shewanella oneidensis* Cytochrome c Nitrite Reductase (ccNiR) does not disproportionate hydroxylamine to ammonia and nitrite, despite a strongly favorable driving force. *Biochemistry*, 53(13), 2136-2144. doi: 10.1021/bi401705d

## Manuscripts

Natalia Stein, Daniel Love, Evan Judd, Sean J. Elliott, Brian Bennett, & A. Andrew Pacheco. (2014). Correlations between the electronic properties of *Shewanella oneidensis* cytochrome c nitrite reductase (ccNiR) and its structure: effects of heme oxidation state and active site ligation.

Evan Judd, Natalia Stein, A Pacheco, & Sean Elliott. (2014). Hydrogen-bonding networks tune proton-coupled redox steps during the enzymatic six-electron conversion of nitrite to ammonia.